

Studies of the emittance growth due to noise in the Crab Cavity RF systems



Thesis submitted in accordance with the requirements of the
University of Liverpool for the degree of Doctor in Philosophy

by

Natalia Triantafyllou

Day Month Year

Abstract

Acknowledgments

Contents

Abstract	iii
Acknowledgments	v
List of figures	xviii
List of tables	xviii
List of symbols	xx
List of symbols v2	1
1 Introduction	1
1.1 The CERN accelerator complex	1
1.1.1 The CERN Super Proton Synchrotron	3
1.2 High-Luminosity LHC project and Crab Cavities	4
1.2.1 Crab cavities	5
1.3 Motivation, objectives and thesis outline	8
2 Basics of accelerator beam dynamics	11
2.1 Motion of charged particles in electromagnetic fields	12
2.2 Single-particle beam dynamics	15
2.2.1 Transverse motion	16
2.2.1.1 Linear dynamics	16
2.2.1.2 Non-linear dynamics	29
2.2.2 Longitudinal motion	30
2.3 Collective effects	33
2.3.1 Wakefields and impedance	34

2.4	Optics models for accelerators	39
2.5	Tracking simulation codes	40
2.5.1	PyHEADTAIL	40
2.5.2	Sixtracklib	43
3	Theory of Crab Cavity RF noise-induced emittance growth	45
3.1	Noise	45
3.2	Crab Cavity noise and emittance growth	46
3.2.1	Crab Cavity amplitude and phase noise	47
3.2.2	Emittance growth formulas	49
3.3	Studies in KEKB	52
4	Calibration of the Crab Cavities for the SPS tests in 2018	54
4.1	Crab Cavities' installation in the SPS	54
4.2	Operational considerations	55
4.3	SPS Head-Tail monitor as the main diagnostic	56
4.3.1	General information	57
4.3.2	Post processing in the presence of Crab Cavities	59
4.3.3	Crab Cavity voltage reconstruction	61
4.3.4	Demonstration of crabbing with proton beams	62
4.4	Characterisation of measured Crab Cavity voltage	63
4.4.1	Definitions of the amplitude and the uncertainty of the measurement	63
4.4.2	Dependence of the crab cavity voltage and offset on the phase .	66
5	Experimental studies 2018: emittance growth from Crab Cavity noise	68
5.1	Experimental configuration and procedure	68
5.1.1	Preparatory experimental studies	69
5.1.2	Machine and beam configuration	69
5.1.3	Experimental procedure	71
5.2	Injected RF noise	71
5.3	Emittance growth measurements	73
5.3.1	SPS Wire Scanners	74
5.3.2	Experimental results	77

0. Contents

5.4	Bunch length and intensity measurements	80
5.4.1	ABWLM and Wall Current Monitor	81
5.4.2	Bunch length measurements	81
5.4.3	Longitunal profile measurements	83
5.4.4	Intensity measurements	84
5.5	Comparison of measured transverse emittance growth with the theoretical predictions	84
5.6	Conclusions and outlook	88
6	Investigation of the discrepancy	89
6.1	Benchmarking with different simulation software	89
6.1.1	PyHEADTAIL	89
6.1.2	Sixtracklib	89
6.2	Sensitivity to the non-linearities of the main SPS dipoles	90
6.3	Simulations using the measured noise spectrum	90
6.4	Sensitvity studies	90
6.5	b3b5b7 multiple errors	90
7	Simulation studies: Suppression mechanism from the beam transverse impedance	91
7.1	SPS transverse impedance model	91
7.1.1	Testing the implementation in PyHEADTAIL	93
7.2	Emittance growth simulations setup	98
7.3	First observations of emittance growth suppression by the impedance	100
7.4	Characterisation of the emittance growth suppression by the impedance	103
7.4.1	Amplitude noise	103
7.4.2	CC RF noise at 200 MHz	104
7.4.3	Pure dipolar noise	106
7.4.4	Sensitivity to linear chromaticity	106
7.4.5	Disentangle quadrupolar and dipolar contribution	106
7.5	Supresion mechanism	106
7.5.1	Past studies with beam-beam interactions	106
7.5.2	Intensity scans	106

7.5.3	Schottky noise spectra	106
7.6	Towards HL-LHC case	106
7.6.1	Damper	106
7.7	Conclusions	107
8	Experimental studies 2022	108
9	Simple model of describing the decoherence suppression from impedance	109
10	Conclusion	110
A	Definitions and methods of statistical analysis	111
A.1	Basic terminology	111
A.1.1	Averages	111
A.1.2	Measuring the spread	112
A.1.3	Data sets with more than one variables - Covariance	113
A.2	Least squares fitting	113
A.3	Propagation of uncertainty	115
B	Fundamentals of signal analysis and measurement	116
B.1	Continuous-time analysis	116
B.2	Discrete-time analysis	118
B.3	Measuring amplitude and phase noise	124
B.4	Applying a measured noise spectrum in numerical simulations	126
B.4.1	Crab cavity noise in numerical simulations	126
B.4.2	Measured noise spectrum	126
B.4.3	Generating time series	127
B.4.4	Validation of the time series reconstruction	128
C	Appendix C	132
C.1	Solutions of betatron equations	132
C.2	Detuning with amplitude	133
C.3	SPS non-linear model	136
D	Glossary and defintions	137

0. Contents

Bibliography	150
---------------------	------------

List of Figures

1.1	Schematic view of the CERN accelerator complex. The different colors correspond to the different machines. The year of commissioning and the type of particles used in each one of them are also indicated along with the circumference for the circular machines. The image is courtesy of CERN.	2
1.2	Visualisation of the CC kick (green line) on the bunch particles (blue dots). The bunch here appears much smaller than the CC wavelength which means that only the linear part of the kick affects the bunch. This will be the case for the HL-LHC scenario.	5
1.3	Layout of the LHC and the SPS. The CC location for the HL-LHC configuration is marked. Two CCs (one per ring) will be installed on each side of ATLAS (red) and CMS (orange). Two prototype CCs were also installed in the SPS (magenta) in 2018, to be tested before their installation in LHC. The layout can be found in Ref. [9] and was modified inspired by Ref. [10].	6
1.4	Collision with and without the use of CCs [11]. CCs restore the overlap between the bunches recovering the luminosity reduction caused by the crossing angle, θ_c . The blue and red colors indicate two bunches in the different rings.	6
2.1	Co-ordinate system used to describe particles motion in a synchrotron. This is a local co-ordinate system, with the origin following the reference trajectory around the accelerator. The unit vector \mathbf{e}_z is tangential to the reference trajectory at each point, \mathbf{e}_y is vertical, and \mathbf{e}_x is horizontal, and perpendicular to \mathbf{e}_z and \mathbf{e}_y	14

0. List of Figures

2.2 Phase space co-ordinates (u, u') turn by turn, for a particle moving along the ring but at a particular position s which is characterised by the following twiss parameters $[\alpha_u(s), \beta_u(s), \gamma_u(s)]$. In the labels shown on the diagram, the dependence on the s parameter has been omitted.	22
2.3 Normalised phase space: the trajectory shown represents the particle motion as the particle moves around the synchrotron. This is not the case in the regular (not normalised) phase space, since the shape of the phase space ellipse will change with position around the ring. The particle moves turn by turn in a circle of radius $\sqrt{2J_u}$	23
2.4 Transverse phase space of a Gaussian bunch. The figure is a courtesy of Tirsi Preibibaj [30].	25
2.5 The closed orbit and the betatron oscillations around it in the presence of dispersion [32]	27
2.6 Phase stability for particles in a circular accelerator which operates above transition.	33
2.7 Wakefield interaction, where the source particle (blue) affects the witness particle (yellow) travelling at a distance z behind it [42]. $(\Delta x_1, \Delta y_1)$ and $(\Delta x_2, \Delta y_2)$ are the transverse offsets of the source and witness particles respectively.	35
2.8 Longitudinal bunch slicing for the implementation of wakefield kicks in PyHEADTAIL. Without the slicing technique (left) the wake kicks on the red macroparticle are generated from all the green macroparticles resulting in computationally expensive simulations. Instead, when the bunch is sliced longitudinally (right) the wake kicks on the macroparticles in the red slice i are generated by the macroparticles in the green slices j , decreasing significantly the computation time. The figures are courtesy of M. Schenk [55]	42

2.9 Graphical representation of the accelerator model and tracking procedure in PyHEADTAIL (inspired by the graphs in Refs. [55, 57]). In this example the ring is split in four segments separated by the interaction points (IPs). Wakefield and multipole kicks are applied to the macroparticles in IP2 and IP4. The macroparticles are transported between the IPs by a linear transfer map (which can include detuning effects) in the transverse plane. The longitudinal coordinates are updated once per turn.	43
3.1 Modulation in amplitude or amplitude noise (left) and its impact on the particles within the bunch (right). The blue dots represent the individual particles while the red arrows indicate the direction of the noise kicks which act on them.	48
3.2 Modulation in phase or phase noise (left) and its impact on the particles within the bunch (right). The blue dots represent the individual particles while the red arrows indicate the direction of the noise kicks which act on them.	49
3.3 Correction term for amplitude (left) and phase (right) noise over a range of bunch length values.	51
4.1 Cross section view of the CC cryomodule [22]. It has a total length of 3 m [66] and at its core there are the two DQW cavities, which are illustrated with light green color.	55
4.2 Diagram of the SPS HT monitor [70]. The beam is passing through a straight stripline coupler which is followed by a 180°hybrid. This configuration provides the sum (Σ) and the difference (Δ) signal of the two electrodes.	58
4.3 Example difference and sum signals (top and bottom plots, respectively) from the HT monitor, in time scale, with respect to the longitudinal position within the bunch over several SPS revolutions, after the basic post processing [70] but before the baseline correction. The different colors indicate the signals from different turns (every 100 turns).	58

0. List of Figures

4.4 2D representation of example difference and sum signals with respect to the longitudinal position within the bunch obtained from the HT monitor over several SPS revolutions.	59
4.5 HT monitor baseline correction for the SPS CC tests. The baseline signal (blue dashed line) refers to the mean of the difference signals acquired before the CC - main RF synchronisation. The measured signal (blue solid line) corresponds to the mean of the difference signal acquired after the synchronisation. Last, the corrected signal (orange solid line) is obtained after subtracting the baseline from the measured signal.	60
4.6 HT acquisitions before and after the synchronisation of the SPS main RF with the CC.	60
4.7 Intra-bunch offset from the CC kick expressed in millimeters after the removal of the baseline.	61
4.8 CC voltage reconstruction from the HT monitor.	62
4.9 Demonstration of the crabbing from the HT monitor signal. CC voltage and sum signal (longitudinal line density) measured from the HT monitor (top) together with the density plot (bottom) which visualises the effect of the CC kick on the beam.	64
4.10 Demonstration of the sinusoidal fit on the HT monitor reading in order to obtain the CC parameters. A four-parameter sinusoidal fit is performed using Eq. (4.2) in order to obtain the amplitude, V_{CC} , the frequency, f_{CC} , the phase, ϕ_{CC} , and the voltage offset, k . The fit results are given in the yellow box.	65
4.11 Phase scan with CC1 at 26 GeV. The sensitivity of the measured CC voltage (left) and its uncertainty (right) on the phase is studied. The error bars of the voltage, V_{CC} , indicate the uncertainty, ΔV_{CC} . The error bars of the uncertainty, ΔV_{CC} , and the phase, ϕ_{CC} , correspond to the error of the respective fit result (see Appendix A.2) The error bars are not visible here as they are smaller than the markers.	66

5.1 Demonstration of the sinusoidal fit on the HT monitor reading in order to obtain the CC parameters as described in Section 4.4. The fit results, are given in the yellow box. The measured voltage amplitude, V_{CC} , was found to be 0.99 MV while its uncertainty, ΔV_{CC} , was measured at 0.04 MV. The measured voltage value agrees well with the requested value of 1 MV.	70
5.2 Example amplitude (left) and phase (right) noise spectra measured with a spectrum analyzer E5052B [81] during the emittance growth studies with CCs in SPS. The noise extends up to 10 kHz (grey dashed line) overlapping the first betatron sideband at ~8 kHz (green dashed line). The spikes at high frequencies correspond to the harmonics of the revolution frequency and are a result of the bunch crossing.	72
5.3 Sketch of the SPS rotational wire scanners [83]. The wire moves across the proton beam generating secondary particles which are then detecting by a scintillator and a photomultiplier. From the measured photomultiplier current the beam profile is reconstructed.	75
5.4 Vertical beam profile obtained from the BWS.41677.V instrument. The measured data points (light blue) are fitted with a four parameter gaussian (orange) to obtain the beam size. The calculated emittance and its uncertainty are also shown.	75
5.5 Bunch by bunch horizontal (top) and vertical (bottom) emittance evolution during the experiment on September, 15, 2018. The four different colors indicate the different bunches. The different applied noise levels are also shown while the moments when the noise level changed are indicated with the grey vertical dashed lines. The emittance growth rates along with their uncertainties for the seven different noise settings are displayed at the legend at the bottom of the plots.	79
5.6 Summary plot of the emittance growth study with CC noise in 2018. The transverse emittance growth rate, for the four bunches, is shown as a function of the different levels of applied noise.	80

0. List of Figures

5.7 Evolution of the beam in transverse and longitudinal planes during the CC noise induced emittance growth experiment. Top: Horizontal emittance growth measured with the SPS WS. Middle: Vertical emittance growth measured with the SPS WS. Bottom: Bunch length evolution measured with the ABWLM (small markers) and the Wall Current Monitor (bigger markers).	82
5.8 Longitudinal profiles (top) and relative bunch position with respect to the center of the RF bucket (bottom) acquired with the Wall Current Monitor. The acquisitions correspond to the times when the sudden jumps in the bunch length evolution are observed (see Fig. 5.7).	83
5.9 Intensity evolution as measured with ABLWM (smaller markers) and with the Wall Current Monitor (bigger markers) during the experiment with CC noise in 2018.	85
5.10 Summary plot of the emittance growth study with CC noise in 2018 focused on bunch 1 only. The measured emittance growth rate (blue) and the expected growths from the theoretical model (black) are shown as a function of the different levels of applied noise.	87
7.1 Horizontal (left) and vertical (right) impedance model of the SPS. The model is available in the public gitlab repository of Ref. [91].	92
7.2 Horizontal (left) and vertical (right) wakefunctions of the SPS. The wake functions are available in the public gitlab repository of Ref. [91]. For comparison the bunch length in the SPS CC experiments is ~ 1.85 ns ($4\sigma_t$).	93
7.3 Horizontal (left) and vertical (right) coherent tunes as a function of intensity in the presence of the beam coupling SPS impedance obtained using analytical formula (blue dashed line) and PyHEADTAIL tracking simulations (orange line). The impedance model and the wake functions used are available in the public gitlab repository of Ref. [91].	96

7.4	Horizontal (left) and vertical (right) coherent tunes as a function of intensity in the presence of the beam coupling SPS impedance obtained using analytical formula (blue dashed line) and PyHEADTAIL tracking simulations (orange line). The impedance model and the wake functions ("updated wakefields" model) used are available in the public repositories of Ref. [91] and Ref. [103] respectively.	97
7.5	Transverse emittance growth driven by CC RF phase noise without (blue) and with (orange) the impedance effects.	102
7.6	Transverse emittance growth driven by CC RF amplitude noise without (blue) and with (orange) the impedance effects.	104
7.7	Transverse emittance growth driven by CC RF noise at $f_{CC} = 200$ MHz without (blue) and with (orange) the impedance effects.	105
B.1	Sampling of the continuous signal $y(t)$ at a finite number of points N . The sampled signal is the discrete-time signal $y(n\Delta t)$ with Δt the sampling interval and n an integer such that $n \in [0, N - 1]$	118
B.2	Example of a signal sampled at discrete time intervals, and the corresponding discrete Fourier transform.	119
B.3	Power spectrum of $y = \sin(2\pi f t)$, $f = 50$ Hz.	121
B.4	Single-sided power spectrum of the signal shown in Fig. B.2(a).	122
B.5	Instantaneous voltage of an oscillator in the presence of (a) amplitude noise, (b) phase noise, and (c) both amplitude and phase noise.	125
B.6	Steps required to generate the sequence of noise kicks to be applied in the simulations from the measured noise spectrum.	129
B.7	Power spectral density computed from the time series ϕ_n produced from a measured power spectrum (black), compared with the original measured power spectrum (green).	130
B.8	Comparison between emittance growth found from simulations in PyHEADTAIL and emittance growth expected from an analytical model [63]. The emittance growth is driven by amplitude and phase noise, with kicks in the simulations generated from a measured power spectrum.	131

List of Tables

4.1	Crab Cavities design parameters for the SPS tests in 2018.	56
4.2	Parameters for computing the CC voltage from the example HT monitor measurements discussed in this chapter.	63
5.1	Main machine and beam parameters for the emittance growth studies with CCs in SPS in 2018.	71
5.2	Phase and amplitude noise levels injected in the CC RF system for the emittance growth studies of 2018. The listed values correspond to the average PSD values over a frequency range of ± 500 Hz around the first betatron sideband, f_b . The calculated effective phase noise for the parameters of the first bunch are also listed.	74
5.3	Comparison between the measured and the calculated transverse emittance growth rates for bunch 1 for the different noise levels, and average bunch length for each case.	87
7.1	PyHEADTAIL simulation parameters used to study impedance induced effects for the SPS.	94
7.2	PyHEADTAIL simulation parameters used for the implementation of the CC RF noise kicks for the emittance growth studies. This table is complementary of Table 7.2.	99
C.1	Multipole errors from SPS non-linear model, at 270 GeV.	136

List of Symbols

E_b	Energy
J_x	Horizontal particle action
J_y	Vertical particle action
V_{RF}	Main RF voltage
f_{RF}	Main RF frequency
CC	Crab Cavity
V_{CC}	CC voltage
f_{CC}	CC frequency
ϕ_{CC}	CC phase
Q_s	Synchrotron tune
D_x	Horizontal dispersion function
D_y	Vertical dispersion function
β_0	Relativistic beta
γ_0	Relativistic gamma (Lorenz factor)
N_b	Bunch intensity i.e. number of particles (here protons)
Q'_x	Horizontal first order chromaticity
Q'_y	Vertical first order chromaticity
σ_t	Rms bunch length
ϵ_x^n	Horizontal normalised emittance of the beam
ϵ_y^n	Vertical normalised emittance of the beam
ϵ_x^{geom}	Horizontal geometric emittance of the beam
ϵ_y^{geom}	Vertical geometric emittance of the beam
ΔQ_x^{rms}	Betatron horizontal rms tune spread
ΔQ_y^{rms}	Betatron vertical rms tune spread
α_{xx}	Horizontal detuning coefficient
α_{yy}	Vertical detuning coefficient
$\alpha_{xy} = \alpha_{yx}$	Cross-detuning coefficients
k_{LOF}	LHC Software Architecture (LSA) trim editor knobs for SPS Landau octupoles, LOF family

0. List of Tables

k_{LOD} LHC Software Architecture (LSA) trim editor knobs for SPS Landau
octupoles, LOD family

1 | Introduction

Particle accelerators were first developed in the early 20th century as a tool for high-energy physics research. By increasing particles' energy they allow us to investigate the subatomic structure of the world and to study the properties of the elementary particles and the fundamental forces. On a basic level, accelerators increase the energy of charged particles using electric fields. Through the years significant technological progress has been achieved resulting in higher energies and greatly enhanced performance of the machines. Additionally, various types of accelerators have been developed (cyclotrons, linacs, synchrotrons etc) using different types of particles (hadrons or leptons) and their use was also expanded in other fields such as medicine and industrial research.

1.1 The CERN accelerator complex

CERN (European Organisation of Nuclear Research), located on the Franco-Swiss border near Geneva, is at the forefront of the accelerator physics research as it operates an extensive network of accelerators, illustrated in Fig. 1.1, including the well-known Large Hadron Collider (LHC) [1].

LHC is a circular machine, 27 km long, built about 100 m underground and is currently the largest and most powerful accelerator. It accelerates and collides two counter-rotating beams of protons or ions (circulating in two different rings) at the four main experiments which are located around the LHC ring, namely ATLAS, CMS, ALICE and LHCb. The highlight of CERN and of the LHC operation up to now was the discovery of the Higgs boson in 2012 from ATLAS [2] and CMS [3], from proton collisions at 3.5 TeV (center-of-mass energy of 7 TeV), which was a milestone for the standard model.

1. Introduction

The beams used by the LHC are produced and gradually accelerated by the injector chain which is a sequence of smaller machines boosting the energy of the beam. In particular, Linac4 (which replaced Linac2 in 2020) accelerates the protons up to 160 MeV, the Proton Synchrotron Booster (PSB) up to 2 GeV, the Proton Synchrotron (PS) up to 26 GeV and the Super Proton Synchrotron (SPS) up to 450 GeV. Finally, the protons are injected in the LHC where they are accelerated up to the collision energy of 6.5 TeV (center-of-mass energy of 13 TeV). It should be noted, that LHC delivered collisions with center-of-mass energy of 7 TeV during Run 1 (2010-2013) which was increased to 13 TeV for the Run 2 (2015-2018) and for Run 3 (2020-present).

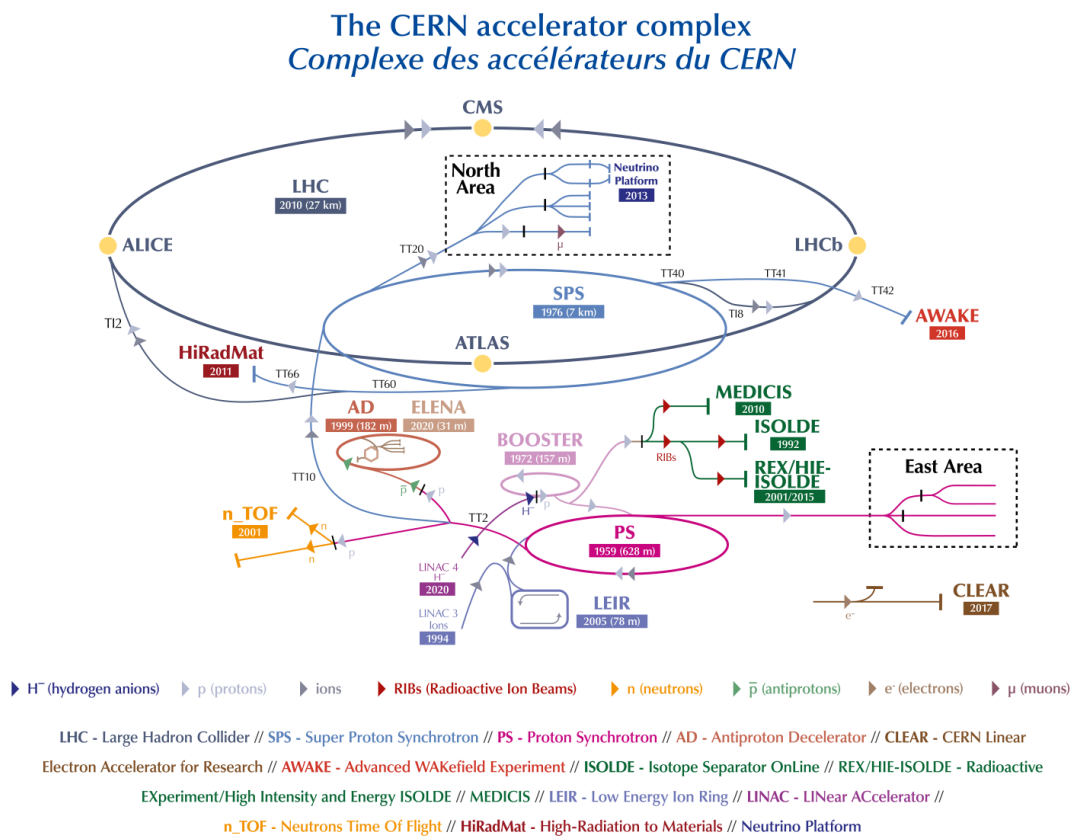


Figure 1.1: Schematic view of the CERN accelerator complex. The different colors correspond to the different machines. The year of commissioning and the type of particles used in each one of them are also indicated along with the circumference for the circular machines. The image is courtesy of CERN.

It is worth mentioning that not only protons but also lead ions are accelerated in the LHC, starting their journey from Linac3 and LEIR and then following the same route as proton beams.

Finally, the accelerators in the injector chain not only prepare the beam for the LHC but also provide beams to various other facilities and experiments at lower energies. Examples are the Anti-proton Decelerator (AD) which studies antimatter, the Online Isotope Mass Separator (ISOLDE) which studies the properties of the atomic nuclei using radioactive beams, and the Advanced Proton Driven Plasma Wakefield Acceleration Experiment (AWAKE) which investigates particle acceleration by proton-driven plasma wakefields.

1.1.1 The CERN Super Proton Synchrotron

The majority of the research described in this thesis was conducted for the Super Proton Synchrotron (SPS). Thus, some additional information about this machine is provided here. The SPS (shown with light blue color in Fig. 1.1) was first commissioned in 1967 and has a circumference of 6.9 km. It used to operate as a proton-antiproton collider ($Spp\bar{S}$) and later on as an injector for the Large Electron Positron collider (LEP) while it also provided beams for fixed-target experiments (e.g. in the North Area). Even though the SPS can accelerate various particle types (protons, antiprotons, electrons, and heavy ions) the following information will concern its operation with proton beams which is the topic of the research presented in this thesis.

Currently, the SPS is the second biggest accelerator at CERN and it can accelerate protons from 26 GeV up to 450 GeV. Due to its past use as a collider, it can also operate as a storage ring. This operational mode is called "coast" and was used for the majority of the experimental studies presented in this thesis. During coast, the bunches circulate in the machine for long periods at constant energy. The highest energy at which SPS can operate in coast is 270 GeV due to limited cooling of the magnets to transfer away the heating when operating at high energy and consequently at large currents for long periods.

1.2 High-Luminosity LHC project and Crab Cavities

High-Luminosity LHC (HL-LHC) [4, 5] is the upgrade of the LHC machine which will extend its potential for discoveries. In particular, it aims to increase the instantaneous luminosity by a factor of 5 beyond the current operational values and the integrated luminosity by a factor of 10.

The luminosity, along with the energy, is a key parameter defining the performance of a collider as is a measure of the collision rate. The instantaneous luminosity is expressed as [6]:

$$\mathcal{L} = \frac{n_b f_{\text{rev}} N_1 N_2}{4\pi \sigma_x \sigma_y} \frac{1}{\sqrt{1 + (\frac{\sigma_z}{\sigma_{\text{xing}}} \frac{\theta_c}{2})^2}}, \quad (1.1)$$

where f_{rev} is the revolution frequency of the machine (the number of times per second a particle performs a turn in the accelerator, definition; in Chapter 2), n_b is the number of colliding bunch pairs, $N_{1,2}$ is the number of particles per bunch, $\sigma_{x,y}$ is the transverse beam size at the interaction point, σ_z the rms bunch length, σ_{xing} the transverse beam size in the crossing plane and θ_c is the full crossing angle between the colliding beams. The crossing angle, is often introduced between the bunches in a collider to reduce parasitic collisions and get rid of the remnants after the collision. For reference, in the LHC, the crossing angle has order of magnitude 10^{-4} radians.

The integrated luminosity is the one that ultimately defines the performance of the machine as it provides the total number of recorded events. It depends both on the instantaneous luminosity and on the machine availability. The integrated luminosity, is expressed as [4]:

$$\mathcal{L}_I \equiv \int_{\Delta t} \mathcal{L} dt, \quad (1.2)$$

where \mathcal{L} is the instantaneous luminosity as defined in Eq. (1.1).

HL-LHC aims to achieve instantaneous luminosity of $\mathcal{L} \sim 5 \cdot 10^{34} \text{ cm}^{-2}\text{s}^{-1}$ and an increase on the integrated luminosity from 300 fb^{-1} to 3000 fb^{-1} over its lifetime of 10-12 years and considering 160 days of operation per year [7].

1.2.1 Crab cavities

To achieve its luminosity goals, HL-LHC will employ numerous innovative technologies. Crab cavity technology (will be denoted as CC in this thesis) [8] is one of the key components of the project as it will be employed to restore the luminosity reduction caused by the crossing angle, θ_c (see Eq. (1.1)).

A crab cavity is an RF cavity which provides a transverse, sinusoidal like, kick to the particles depending on their longitudinal position within the bunch. A graphical visualisation of the kick is shown in Fig. 1.2. It can be seen that the head (leading part) and the tail (trailing part) of the bunch receive opposite deflection while the particles at the center remain unaffected.

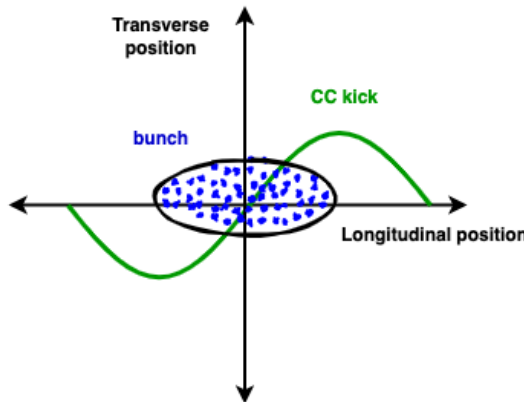


Figure 1.2: Visualisation of the CC kick (green line) on the bunch particles (blue dots). The bunch here appears much smaller than the CC wavelength which means that only the linear part of the kick affects the bunch. This will be the case for the HL-LHC scenario.

The CCs will be installed in the two main interaction points of LHC, ATLAS and CMS. According to the plan, two CCs will be installed on each ring and on each side of the interaction points (eight in total). This is displayed in Fig. 1.3 with the red (ATLAS) and orange (CMS) markers. The reason why two CCs are needed in each ring on each side of the IP is discussed in the following paragraphs (local vs global scheme).

1. Introduction

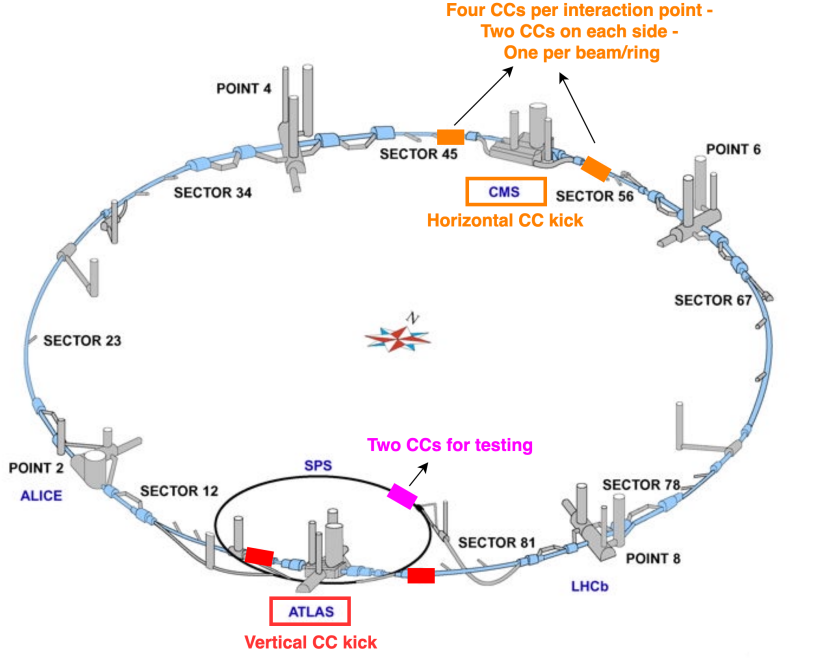


Figure 1.3: Layout of the LHC and the SPS. The CC location for the HL-LHC configuration is marked. Two CCs (one per ring) will be installed on each side of ATLAS (red) and CMS (orange). Two prototype CCs were also installed in the SPS (magenta) in 2018, to be tested before their installation in LHC. The layout can be found in Ref. [9] and was modified inspired by Ref. [10].

In this configuration, the bunches receive the transverse deflection from the first pair of CCs just before reaching the interaction point. This results in a rotation of the bunch, which mitigates the crossing angle and restores the head-on collisions. The deflection is cancelled once the bunches reach the second pair of CCs which are symmetrically placed at the opposite side of the interaction point. The collision of the bunches in the presence of the CCs is illustrated in Fig. 1.4 [11].

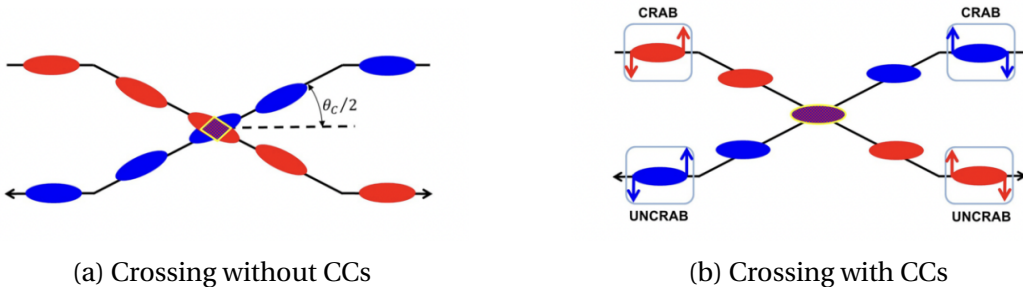


Figure 1.4: Collision with and without the use of CCs [11]. CCs restore the overlap between the bunches recovering the luminosity reduction caused by the crossing angle, θ_c . The blue and red colors indicate two bunches in the different rings.

The above scheme, with CCs before and after the interaction point, is called the local crabbing scheme. An alternative scheme, named the global crabbing scheme, was also under discussion in the first stages of the project. In such a scheme, the closed orbit distortion that is caused by the fact that the head and the tail of the bunch are kicked in opposite directions propagates in the ring, resulting in transverse bunch oscillations [5]. This scheme is cost-efficient compared to the local scheme as it only requires two CCs. However, it introduces significant constraints on the betatron phase advance between the interaction points and the CCs. The constraints are enhanced by the fact that the bunch crossing in ATLAS takes place in the vertical plane while in CMS in the horizontal. To this end, the local CC scheme was chosen for the HL-LHC configuration.

In order to accommodate the crossing in both transverse planes two CC designs have been developed: the Double-Quarter Wave (DQW) and the RF dipole (RFD), which provide vertical and horizontal deflection respectively. Information on their design can be found in Refs. [12, 13, 14, 15]

The CCs have already been successfully used in the KEKB collider [16] in Japan, during 2007-2010, with lepton beams ($e^+ - e^-$) [17, 18, 19]. However, there are significant differences in the beam dynamics in the presence of CCs in leptons and hadrons (HL-LHC case). One of the most crucial points is the impact of errors (e.g. RF noise) which leads to beam degradation [20, 21]. This is not an issue of concern for lepton beams as they nevertheless experience emittance damping due to synchrotron radiation. For proton beams, the synchrotron radiation damping is much weaker meaning that the beam degradation can lead to emittance growth which eventually can result in loss of luminosity.

As the CCs have never been used with protons before, two prototype superconducting CCs were installed in the SPS (Fig. 1.3, magenta markers) to test the technical systems, to validate their operation with proton beams and to identify and address potential issues before their installation in LHC. The SPS provides an ideal test bed for these studies as it allows testing under conditions that are closer to those in HL-LHC than any other machine. In particular, the SPS operates with proton beams, can run in storage-ring mode, and in terms of the

1. Introduction

energy reach is second only to LHC. The two CCs that were installed in SPS [22] were identical, fabricated at CERN and of the DQW type (like the ones that will be used in ATLAS interaction point in HL-LHC).

1.3 Motivation, objectives and thesis outline

As mentioned above, one of the main concerns regarding the CC operation with protons is the emittance growth due to noise in their RF system as it leads to luminosity loss. For the HL-LHC, the target values regarding the luminosity loss and emittance growth are very tight. In particular the maximum allowed luminosity loss due to CC RF noise induced emittance growth is targeted at just 1%, during a physics fill, which corresponds to an CC RF noise induced emittance growth of 2 %/h [23, 24, 25]. To this end, a good understanding and characterization of the emittance growth mechanism is crucial for the HL-LHC project.

It should be added here that a physics fill is the time period during which the beams are successfully injected in the LHC at the desired conditions, they are accelerated at the desired energy and they are kept in the machine for consecutive collisions. After some hours, due to beam degradation the beams are dumped and a new fill is prepared. A fill in the HL-LHC will last a couple of hours.

This thesis focuses on understanding, characterising and evaluating the mechanism of CC RF noise-induced emittance growth including numerical and experimental studies. The studies presented in this thesis were conducted for the SPS machine since it has proton crabbing operational experience and allows direct comparison of predictions from models and experimental data. It should be emphasised that the CC tests in SPS constitute the first experimental beam dynamics studies with CCs and proton beams. The results and the understanding obtained from this research are essential for the HL-LHC, in order to predict the long-term emittance and to define limits on the acceptable noise levels for the CCs.

This thesis reports research that was carried out between 2018 and 2022, based at CERN and it structured as follows:

Chapter 2 presents the basics of accelerator beam dynamics focusing on the concepts that are relevant for understanding the studies presented in this thesis.

This paragraph needs to be re-written after you finish chapter 2. In particular, definitions are given for linear optics, non-linear optics, of emittance, transfer maps, wakefields, detuning with amplitude. Finally, the two simulation codes used in this thesis for macroparticle tracking, PYHEADTAIL and Sixtracklib, are described.

The mechanism of noise induced emittance growth and in particular of the CC RF noise induced emittance growth is explained in Chapter 3. The modelling of the noise effects in the simulations is also discussed. Finalise after writing chapter 3.

Chapter 4 is devoted to the methodology used for the calibration of the CCs. The first sections provide some general details on the CC installation and operation in the SPS. The instrument that is used as the main diagnostic is described. Finally, the post-processing of the measurements to characterise the CC voltage and phase is explained.

The results from the first experimental studies of the emittance growth from CC RF noise in the SPS are presented in Chapter 5. First, the experimental configuration and procedure is reported. Second the artificial noise injected in the CC RF system for the measurements is discussed in detail. Subsequently, the emittance growth measurements are presented along with the measured bunch length and intensity evolution for completeness. Last the measured emittance growth rates are compared with the predictions from the theoretical model (described in Chapter 3). It was found the the measured growth rates were systematically a factor of 4 on average lower than the predictions.

Various possible factors were investigated as a possible explanation for this discrepancy. These extensive studies, which took place over two years are described in Chapter 6. Initially, the theory was benchmarked with different simulation software: PyHEADTAIL and Sixtracklib. The sensitivity of the emittance evolution on the non-linearities of the SPS machine (which was not included in the theory of Chapter 3) was also tested. Last, thorough studies were performed to

1. Introduction

exclude the possibility that the discrepancy is not a result of possible errors in the analysis of the experimental data or the actual noise levels applied on the CCs. However, none of these factors could explain the discrepancy.

Finally, simulations including the SPS transverse impedance model (not included in the theory (of Chapter 3) showed a significant impact on the emittance growth. Chapter 7 discusses the investigation and characterisation the phenomenon of the emittance growth suppression from the beam coupling impedance as observed in simulations with PyHEADTAIL. It was shown that the suppression is related to the dipole motion which is excited by the CC RF phase noise.

Chapter 8, presents the results from the second round of emittance growth measurements with CCs in SPS that took place in 2022. The objective of these experimental studies was to validate the mechanism of the suppression of the CC RF noise-induced emittance growth from the beam coupling impedance as observed in simulations (described in Chapter 7). This would also confirm that this impedance-induced effect is the reason for the discrepancy observed in the 2018 experiment between the measurements and the theoretical predictions. The experiments of 2022 successfully confirmed the suppression mechanism, despite the very challenging conditions of the studies.

In Chapter 9, further experimental results with the use of the SPS transverse damper as a source of noise are shown. The measurements took place in 2022, after the CC experiment for the same machine and beam conditions. The objective was to obtain further measurements which would validate the mechanism of the suppression of the noise-induced emittance growth by the impedance. The use of the damper is an appropriate configuration as it provides dipolar noise kicks in the beam and as shown in Chapter 7 the suppression mechanism is related to the dipole motion. The experimental results from use of the damper are also compared with the predictions from a recently developed theoretical model from X. Buffat which describes the emittance growth suppression from a collective force.

Last, Chapter 10 summarizes the conclusions of the thesis. The project is viewed from a broad perspective highlighting its importance. Potential follow up studies are proposed. [Comment on Appendix?](#)

2 | Basics of accelerator beam dynamics

In this chapter, the basic concepts of accelerator beam physics that are essential for understanding the studies presented here are introduced. A more complete description can be found in the books of the following references: [26, 27, 28]. The focus is put on the concepts for synchrotrons with proton beams. Additionally, in the last section, the tracking simulation codes used in this work are described.

Synchrotrons are circular accelerators where the particles follow a fixed closed-loop path. In a synchrotron, electric fields accelerate the particles while magnetic fields steer and focus them. The magnetic fields are not constant but they vary according to the particles' energy, allowing acceleration and operation at very high (relativistic) energies. The LHC and SPS machines at CERN are synchrotrons like many of the machines used for High Energy Physics experiments. Usually, in synchrotrons, the beams consist of multiple bunches, longitudinally spaced around the machine. Although the bunches interact with each other, these interactions are not relevant to the studies presented later in this thesis, and will not be considered further

Finally, at this point, it is appropriate to introduce the terms incoherent and coherent effects. Incoherent effects (microscopic approach) affect the individual particles affect individual particles. Any theory or model of incoherent effects has to treat the beam as a collection of a large number of individual particles, each with its own behaviour. In contrast, coherent effects can be understood in terms of their impact on the beam as a whole, and can be modelled by representing each bunch, for example, as a single 'macroparticle', with mass and charge corresponding to the total number of particles it contains.

2.1 Motion of charged particles in electromagnetic fields

The motion of a particle with charge q and velocity $\mathbf{v} = (v_x, v_y, v_z)$ moving in an electric field \mathbf{E} and a magnetic field \mathbf{B} is defined by the influence of the Lorentz force:

$$\mathbf{F}_L = q(\mathbf{E} + \mathbf{v} \times \mathbf{B}). \quad (2.1)$$

At this point, it is appropriate to mention that in this thesis the vectors are denoted in bold font (e.g. \mathbf{E}).

In synchrotrons, the electric fields, which are generated by radiofrequency (RF) cavities, are used for accelerating the beams. The magnetic fields, are used to steer (dipoles) and focus (quadrupoles) and apply corrections (sextupoles, octupoles and higher order multipoles) to the motion of the beam. The sequence of the various electromagnetic elements around the accelerator ring is called the machine lattice.

Reference trajectory and reference momentum

Here the concepts of reference momentum and reference trajectory are introduced. They both can be chosen arbitrary and are used as a reference for describing the particles motion in the magnetic fields of an accelerator. It might be the case that no particle follows the reference trajectory and has the reference momentum.

The reference trajectory is a chosen curved path in space which acts as a reference for the alignment of the accelerator components. It is defined by the dipoles and is typically chosen such as it passes from the center of all the magnets. The total length of the reference trajectory in a circular accelerator is called the circumference, C_0 .

The particle that follows this trajectory is called the reference particle and has a momentum p_0 , an energy E_0 , and a velocity v_0 . This particle is often called the synchronous particle as it crosses an RF cavity always at the same phase (assuming constant speed and no losses). For a proton, the reference momentum is given by:

$p_0 = \gamma_0 m_p v_0$, where m_p is the proton rest mass, and $\gamma_0 = \frac{1}{\sqrt{1-\beta_0^2}}$ is the relativistic gamma or Lorentz factor, where $\beta_0 = v_0/c$ is the relativistic β with c being the speed of light.

Mangetic rigidity

At this point, it is appropriate to introduce the concept of magnetic rigidity, $B_0\rho$, which is often used in accelerators as a normalisation factor and is a measure of how the charged particles resist bending by a dipolar magnetic field. Assuming that a proton moves only under the influence of a uniform vertical dipole field $\mathbf{B}_0 = (0, B_0, 0)$, it would follow a circular path of radius ρ (it will be often referred to as bending radius) which is defined by the Lorentz force (Eq. (2.1)) being equal to the centripetal force, as follows:

$$ev_0 B_0 = \frac{\gamma_0 m_p v_0^2}{\rho} \Rightarrow B_0 \rho = \frac{\gamma_0 m_p v_0}{e} \Rightarrow B_0 \rho = \frac{p_0}{e}, \quad (2.2)$$

where e and m_p are the charge and rest mass of a proton respectively, p_0 is the reference momentum, and γ_0, β_0 the relativistic gamma and beta. In the ultra-relativistic regime which is the case in the studies presented in this thesis, the approximation $\beta_0 = 1$ is often used. From Eq. (2.2) it becomes clear that the magnetic rigidity is another way of stating the reference momentum, p_0 .

If the particle momentum is given in GeV/c (which are the usual units in high energy accelerators) then the unit of magnetic rigidity is T · m.

Co-ordinate system

However, the individual particles do not follow the reference trajectory due to small deviations in their initial conditions: an example trajectory is shown in Fig. 2.1 with the blue line. The co-ordinate system used to describe the individual trajectories of the beam particles around the accelerator is illustrated in Fig. 2.1 and it is known as Frenet-Serret system. It consists of the orthogonal co-ordinate system $\Sigma(s) = (\mathbf{e}_x, \mathbf{e}_y, \mathbf{e}_z)$ whose origin moves along the reference trajectory (red line) together with the beam.

The variable s denotes the distance along the reference trajectory. In accelerator physics, s is usually chosen as the independent variable instead of time, t .

2. Basics of accelerator beam dynamics

Therefore, at any given location s around the ring, the coordinates $(x(s), y(s), z(s))$ give the horizontal, vertical, and longitudinal position of the particle with respect to the origin of the orthogonal moving system Σ . In the following paragraphs, the dependence of the co-ordinates on the position s along the ring is omitted when possible to facilitate the notation (e.g. $x(s)$ will be denoted as x).

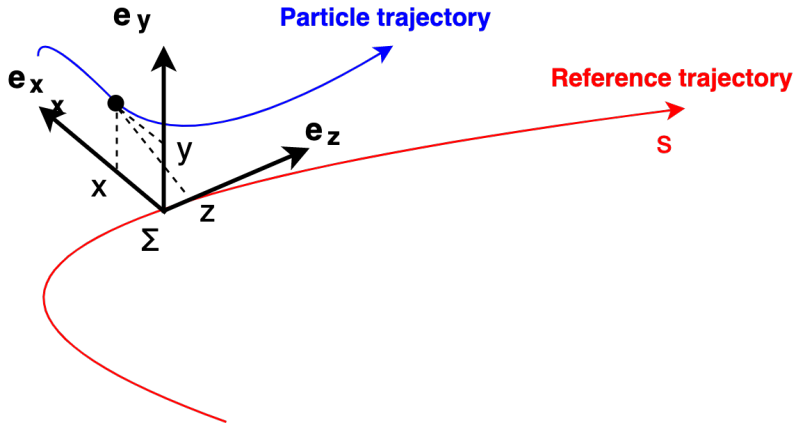


Figure 2.1: Co-ordinate system used to describe particles motion in a synchrotron. This is a local co-ordinate system, with the origin following the reference trajectory around the accelerator. The unit vector \mathbf{e}_z is tangential to the reference trajectory at each point, \mathbf{e}_y is vertical, and \mathbf{e}_x is horizontal, and perpendicular to \mathbf{e}_z and \mathbf{e}_y .

At any point s along the reference trajectory each particle is represented by the six-dimensional "phase space" vector $(x, x', y, y', z, \delta)$ where:

$$x' = \frac{dx}{ds} = \frac{dx}{dt} \frac{dt}{ds} = \frac{v_x}{v_z} = \frac{p_x}{p_z} \approx \frac{p_x}{p_0}, \quad (2.3a)$$

$$y' = \frac{dy}{ds} = \frac{dy}{dt} \frac{dt}{ds} = \frac{v_y}{v_z} = \frac{p_y}{p_z} \approx \frac{p_y}{p_0}, \quad (2.3b)$$

$$\delta = \frac{\Delta p}{p_0} = \frac{p - p_0}{p_0}, \quad (2.3c)$$

$$z = \beta_0 c(t_0 - t), \quad (2.3d)$$

where p_0 and β_0 are the momentum and relativistic (scaled) velocity, respectively, of the reference particle, t_0 is the time which the reference particle arrives at the location s and t is the time at which the individual particle arrives at the same location. It can be seen that δ is the relative momentum offset from the reference particle. In order to avoid a possible misconception it seems appropriate to clarify here, that the longitudinal parameter z indicates the longitudinal offset from the

reference particle at the center of the bunch. If $z > 0$ ($z < 0$) the corresponding particle arrives earlier (later) than the center of the bunch at an arbitrary reference point. Last, in the ultra-relativistic regime the momentum of the particles in the \mathbf{e}_z direction is much larger than the transverse ones and almost equals the reference momentum: $p_x, p_y \ll p_z \approx p_0$. This is why the values of x' and y' are close to p_x/p_0 and p_y/p_0 , respectively.

To summarize, the motion of the particles is treated separately in the transverse and longitudinal planes where it is described with the (x, x', y, y') and (z, δ) co-ordinates respectively. As an example the co-ordinates of the reference particle are $(x = 0, x' = 0, y = 0, y' = 0, z = 0, \delta = 0 (p_z = p_0))$.

Last, (x, y, z) are expressed in meters, (x', y') in radians while δ is dimensionless.

2.2 Single-particle beam dynamics

In this section, the interactions between the particles within a bunch are neglected, hence the term single-particle beam dynamics.

Two-dimensional complex fields

As already discussed, the motion of the charged particles inside a circular accelerator is controlled by magnetic fields. In this thesis, the magnets are considered purely transverse elements. Their effect is therefore described with two-dimensional multipole fields, acting in the horizontal and vertical planes¹.

The description of two-dimensional magnetic fields in accelerator physics is discussed using the concept of multipole expansion and is expressed as a complex quantity. The complex quantity allows to describe a two-dimensional field in (x, y) space (to be compatible with the co-ordinates used for describing the particle's trajectory as discussed in the previous section). Therefore, the magnetic field

¹Examples of three-dimensional treatment can be found in [26, 29]. However, the two-dimensional treatment is most often used in accelerator physics as it provides a good description for the majority of the magnetic elements.

2. Basics of accelerator beam dynamics

around the beam is expressed as follows [26]:

$$B_y(x, y) + iB_x(x, y) = \sum_{n=1}^{\infty} C_n (x + iy)^{n-1}, \quad (2.4)$$

where n indicates the order of the field component: $n=1$ for a dipole (steering), $n=2$ for quadrupole (focusing), $n=3$ for sextupoles (chromaticity correction), $n=4$ for octupole (error or field correction) etc. $C_n = (b_n + ia_n)$ is a complex constant which denotes the strength and orientation of the multipole field. The coefficients $b_n = \frac{1}{(n-1)!} \frac{\partial^{n-1} B_y}{\partial x^{n-1}}$ and $a_n = \frac{1}{(n-1)!} \frac{\partial^{n-1} B_x}{\partial x^{n-1}}$ denote the strength of a normal and skew (normal multipole rotated by $\pi/2(n)$) multipole respectively in units of T/m^{n-1} .

Usually, in accelerator physics the values of the multipole strengths are quoted normalised to the magnetic rigidity as defined in Eq. (2.2) and are denoted by:

$$k_n = \frac{b_n}{B_0 \rho}, \quad (2.5)$$

where k_n is expressed in units of m^{-n} . This is the convention that will be used in this thesis.

It should be clarified here, that the notations of B_0 and b_1 are equivalent. However, in accelerator physics the magnetic rigidity is denoted as $B_0 \rho$ as a convention due to its derivation at the early stages of the analysis (see Eq.(2.2)). This notation will be used throughout this thesis.

2.2.1 Transverse motion

In the transverse plane the motion is orthogonal to the reference trajectory (see Fig. 2.1) and its co-ordinates are (x, x', y, y') . For the discussion on the transverse beam dynamics, the (x, x') and (y, y') co-ordinates will be both described by (u, u') when possible to facilitate the notation.

2.2.1.1 Linear dynamics

Here the transverse motion of a particle moving through the two-dimensional fields described in Eq. (2.4) is discussed. For now, the discussion is limited only to

dipolar and quadrupolar components ($n = 1$ and $n = 2$) which are considered the basic magnetic elements, as in the absence of magnetic errors or momentum deviations between the particles they are sufficient to create a synchrotron.

As mentioned above, the particles transversely oscillate around the reference trajectory (except for a nominal reference particle which follows it). This motion, through an arbitrary periodic sequence of dipoles and quadrupoles, is called betatron motion and can be described by the following equations of motion [28]:

$$x'' - \frac{\rho + x}{\rho^2} = -\frac{B_y}{B_0\rho} \frac{p_0}{p} \left(1 + \frac{x}{\rho}\right)^2, \quad (2.6)$$

$$y'' = \frac{B_x}{B_0\rho} \frac{p_0}{p} \left(1 + \frac{x}{\rho}\right)^2, \quad (2.7)$$

where $B_0\rho$ and ρ the magnetic rigidity and radius as defined in Eq. (2.2), B_y, B_x the transverse magnetic fields of Eq. (2.4), and p_0 the reference momentum.

In the case of dipole and quadrupole fields, linear approximations to the equations of motion (equations describing the particle motion through the fields) provide good representations of the dynamics, at least in the case of the transverse motion. Hence the name linear dynamics. For the linear approximation the following assumptions are made: the transverse offset and angle of motion of the rest of the particles (x, x', y, y') are very small and close to the reference trajectory and only the linear terms in x and y of the magnetic field (described in Eq. (2.4)) are taken into account, such as [28]:

$$B_y = B_0 + \frac{\partial B_y}{\partial x} x = B_0 + b_2 x, \quad B_x = \frac{\partial B_x}{\partial x} y = b_2 y. \quad (2.8)$$

Note that the term B_0 doesn't appear in the horizontal magnetic field due to the fact that, as mentioned earlier, only vertical dipole fields are considered.

Exapnding Eqs. (2.6) and (2.7) to the first order of x and y respectively, setting $\delta = (p - p_0)/p_0$, and $k_2 = b_2/(B_0\rho)$ the linear equations of motion are

2. Basics of accelerator beam dynamics

obtained [28]:

$$x'' + \left(\frac{1-\delta}{\rho^2(1+\delta)} + \frac{k_2(s)}{1+\delta} \right) x = \frac{\delta}{\rho(1+\delta)}, \quad (2.9)$$

$$y'' - \left(\frac{k_2(s)}{1+\delta} \right) y = 0, \quad (2.10)$$

where the sign-convention is $k_2 > 0$ ($k_2 < 0$) for focusing in the horizontal (vertical) plane. It is worth commenting that $1/\rho = B_0/(B_0\rho) = b_1/(B_0\rho) = k_1$ the normalised dipole strength.

For on-momentum particles (with $\delta = 0$) ² the linear equations of motion are simplified even more to the equation for a harmonic oscillator (but with an s dependent strength $K_u(s)$), named Hill's equation [28]:

$$u''(s) + K_u(s) u(s) = 0, \quad (2.11)$$

where $u = (x, y)$ and:

$$K_u(s) = \begin{cases} \frac{1}{\rho^2(s)} + k_2(s), & u = x \\ -k_2(s), & u = y \end{cases} \quad (2.12)$$

with $k_2(s)$ being the normalised quadrupole strength. It should be noted that for Eq. (2.11) it is assumed the motion in the horizontal plane is independent of the motion in the vertical plane, and vice-versa, i.e. the motion is uncoupled.

As already mentioned, Eq. (2.11) resembles the equation of motion for a harmonic oscillator, but with an oscillation frequency that varies with position along the beamline (i.e. varies with s). For a circular accelerator K_u is periodic: $K_u(s + C_0) = K_u(s)$, where C_0 is the periodicity of the accelerator and real-valued. The general solution of Hill's equations in this case is (using the Floquet transformation) [28]:

$$u(s) = Aw(s) \cos(\psi_u(s) + \psi_{u,0}), \quad (2.13)$$

where A and $\psi_{u,0}$ the integration constants and $w(s)$ and $\psi_u(s)$ are the amplitude and betatron phase functions, which are periodic functions with the same periodicity as K_u .

²The solution of the equation of motion for off-momentum particles is discussed in the paragraph "Off-momentum effects: dispersion" later in this section.

After substituting for $u(s)$ from Eq. (2.13) in Eq. (2.11), we find after some calculation (see Appendix C.1) that the amplitude and phase functions fulfill the following equations:

$$w_u'' + K_u(s) w_u(s) - \frac{1}{w_u(s)^3} = 0, \quad (2.14)$$

where:

$$\psi'_u(s) = \frac{1}{w_u(s)^2} \Rightarrow \psi_u(s) = \int_{s_0}^s \frac{ds}{w_u(s)^2} \quad (2.15)$$

The above equations are called the betatron envelope and phase equations.

Courant-Snyder parameters

At this point it is appropriate to introduce the betatron or Twiss or Courant-Snyder:

$$\beta_u(s) = w_u(s)^2, \quad (2.16a)$$

$$\alpha_u(s) = -\frac{1}{2} \beta'_u(s), \quad (2.16b)$$

$$\gamma_u(s) = \frac{1 + \alpha_u(s)^2}{\beta_u(s)}, \quad (2.16c)$$

with $\beta'_u(s) = d\beta_u(s)/ds$.

The betatron phase advance from Eq. (2.15) can be re-written using the beta twiss function as:

$$\psi_u(s) = \int_{s_0}^s \frac{ds}{\beta_u(s)}. \quad (2.17)$$

The advantage of the Twiss parameters over using $w_u(s)$ and $\psi_u(s)$ is that they can be also used to describe the properties of a bunch of particles while the latter describe the motion of each particle individually. This is discussed in further details in the following paragraph "Transverse emittance".

Betatron tune

Another important quantity in accelerator physics is the betatron tune of the machine, Q_u , which is the phase advance for one complete revolution around the machine divided by 2π :

$$Q_u = \frac{\psi_u(s+C) - \psi_u(s)}{2\pi} = \frac{1}{2\pi} \oint_C \frac{ds}{\beta_u(s)}, \quad (2.18)$$

2. Basics of accelerator beam dynamics

where C is the circumference of the machine. As it can be seen, the tune also represents the number of betatron oscillations that a particle undergoes during one full revolution around the machine.

The tune of the individual particles may vary due to effects such as the chromaticity, the detuning with their transverse amplitude, and collective forces (e.g. impedance) that will be discussed in the following paragraphs. The horizontal and vertical tune of the reference particle will be referred to as the bare tunes and define what is called the working point of the machine, (Q_{x0}, Q_{y0}) .

Matrix formalism

Knowing the lattice (element per element structure of the accelerator) the solutions $w_u(s)$ and $\psi_u(s)$ of the Hill's equation can also be described using a matrix formalism as follows:

$$\begin{pmatrix} u \\ u' \end{pmatrix}_{s_1} = M_u(s_1|s_0) \begin{pmatrix} u \\ u' \end{pmatrix}_{s_0}, \quad (2.19)$$

where $u = (x, y)$. The transfer matrix from the position s_0 to the s_1 , $M_u(s_1|s_0)$, can be expressed in terms of the Courant-Snyder parameters as [28]:

$$M_u(s_1|s_0) = \begin{pmatrix} \sqrt{\frac{\beta_u(s_1)}{\beta_u(s_0)}}(\cos \Delta\psi_u + \alpha_u(s_0) \sin \Delta\psi_u) & \sqrt{\beta_u(s_0)\beta_u(s_1)} \sin \Delta\psi_u \\ -\frac{1+\alpha_u(s_0)\alpha_u(s_1)}{\sqrt{\beta_u(s_0)\beta_u(s_1)}} \sin \Delta\psi_u + \frac{\alpha_u(s_0)-\alpha_u(s_1)}{\sqrt{\beta_u(s_0)\beta_u(s_1)}} \cos \Delta\psi_u & \sqrt{\frac{\beta_u(s_0)}{\beta_u(s_1)}}(\cos \Delta\psi_u + \alpha_u(s_1) \sin \Delta\psi_u) \end{pmatrix} \\ = \begin{pmatrix} \sqrt{\beta_u(s_1)} & 0 \\ -\frac{\alpha_u(s_1)}{\sqrt{\beta_u(s_1)}} & \frac{1}{\beta_u(s_1)} \end{pmatrix} \begin{pmatrix} \cos \Delta\psi_u & \sin \Delta\psi_u \\ -\sin \Delta\psi_u & \cos \Delta\psi_u \end{pmatrix} \begin{pmatrix} \frac{1}{\sqrt{\beta_u(s_0)}} & 0 \\ \frac{\alpha_u(s_0)}{\sqrt{\beta_u(s_0)}} & \sqrt{\beta_u(s_0)} \end{pmatrix}, \quad (2.20)$$

where $\Delta\psi_u = \psi_u(s_1) - \psi_u(s_0)$ is the betatron phase advance between the two locations while $\alpha_u(s_i)$ and $\beta_u(s_i)$ are the Courant-Snyder parameters at the location s_i , where $i = (0, 1)$. Transfer matrices provide a very convenient approach to accelerator beam dynamics, and will be used extensively throughout this thesis to study the motion of the particles in the accelerator lattice.

Action-angle variables and phase space ellipse

The action variable is introduced here as it is used in the definition of emittance which is one of the parameters of primary interest for this thesis. Additionally, the octupole magnets that will be used in the CC studies introduce betatron detuning which is linearly expressed in terms of action (see Eqs. (2.43) and (2.44)).

The solution of equation of motion (Eq. (2.11)) can alternatively be expressed in action-angle co-ordinates (J_u, ψ_u) as follows:

$$u(s) = \sqrt{2\beta_u(s)J_u} \cos(\psi_u(s)). \quad (2.21)$$

By differentiation the divergence u' is written as:

$$u'(s) = -\sqrt{\frac{2J_u}{\beta_u(s)}} (\sin(\psi_u(s)) + \alpha_u(s) \cos(\psi_u(s))), \quad (2.22)$$

where $\beta_u(s), \alpha_u(s)$ are the Twiss parameters as defined in Eq. (2.16), $\psi_u(s)$ the betatron phase as defined in Eq. (2.15) and J_u is an integration constant which is defined by the initial conditions.

The action, J_u is an invariant of the motion and can be written in terms of the Twiss parameters as:

$$J_u = \frac{1}{2}(\gamma_u(s)u^2(s) + 2\alpha_u(s)u(s)u'(s) + \beta_u(s)u'^2(s)) = \text{constant}. \quad (2.23)$$

The trajectory of each individual particle can be plotted in phase space (u, u') at a given position s in the ring turn after turn. In phase space, the particle's path is an ellipse whose shape and orientation are determined by the Twiss parameters at the position s . This ellipse, named phase space or Courant-Snyder ellipse, is illustrated in Fig. 2.2 and it has an area of $2\pi J_u$. It is worth mentioning, that the ellipse's size is different for each particle as it depends on their individual actions, J_u i.e. their individual initial conditions. The center of the ellipse is the closed orbit which, in the absence of steering errors in a synchrotron, can be identified with the reference trajectory and is also shown in the plot.

Normalised phase space

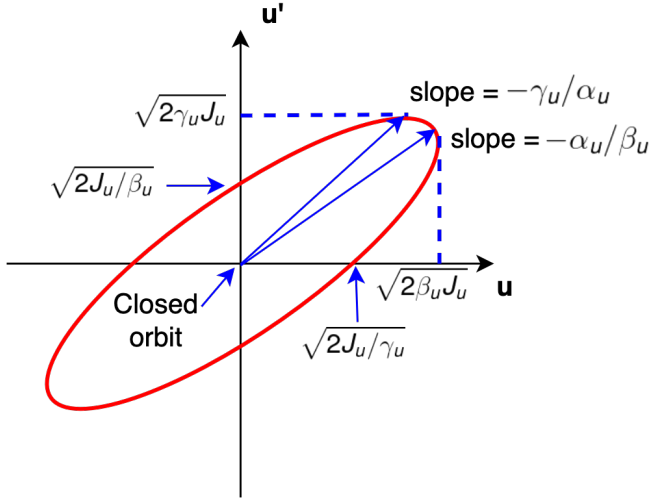


Figure 2.2: Phase space co-ordinates (u, u') turn by turn, for a particle moving along the ring but at a particular position s which is characterised by the following twiss parameters $[\alpha_u(s), \beta_u(s), \gamma_u(s)]$. In the labels shown on the diagram, the dependence on the s parameter has been omitted.

Often in accelerator physics, it is useful to transform the transverse phase space ellipse into a normalised phase space circle. In the normalised phase space the co-ordinates (u, u') are normalised with the twiss parameters (α_u, β_u) for the particular location s around the ring, as follows [27]:

$$u_N(\phi) = \frac{u(s)}{\sqrt{\beta_u(s)}}, \quad (2.24)$$

$$u'_N(\phi) = \frac{du_N}{d\phi} = \sqrt{\beta_u(s)} u'(s) + \frac{\alpha_u(s)}{\beta_u(s)} u(s), \quad (2.25)$$

where $\phi = \frac{\psi_u}{Q_u}$. It can be seen that the independent variable in the normalised co-ordinates is the phase advance (normalised with the betatron tune), ϕ , instead of the location s along the ring. Both of the normalised co-ordinates, (u_N, u'_N) are expressed in units of $m^{1/2}$.

Combining Eq. (2.23), Eq. (2.16), Eq. (2.24) and Eq. (2.25) the action variable can also be written as:

$$J_u = \frac{1}{2}(u_N^2 + u'^2_N). \quad (2.26)$$

The phase space in normalised co-ordinates is shown in Fig. 2.3.

Transverse emittance

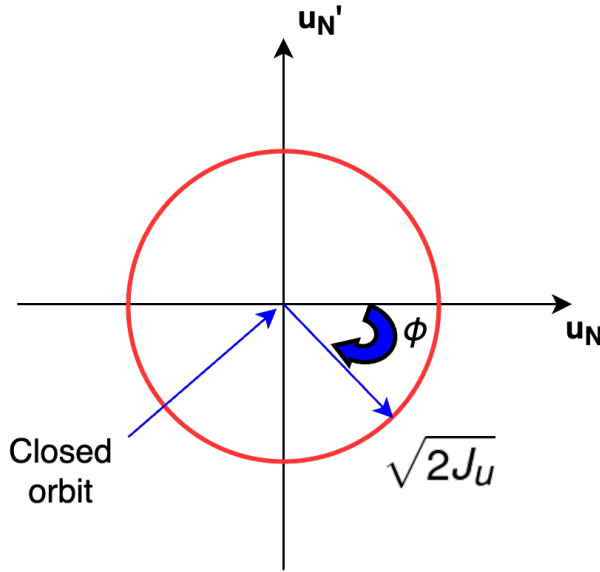


Figure 2.3: Normalised phase space: the trajectory shown represents the particle motion as the particle moves around the synchrotron. This is not the case in the regular (not normalised) phase space, since the shape of the phase space ellipse will change with position around the ring. The particle moves turn by turn in a circle of radius $\sqrt{2J_u}$.

Up to now, the Twiss parameters were used to describe the dynamics of single particles. However, they also describe the distribution of the particles within a bunch. The statistical average of u^2 over all particles at a given point s along the reference trajectory, from Eq. (2.21) equals to [26]:

$$\langle u^2(s) \rangle = 2\beta_u(s) \langle J_u \cos^2 \psi_u(s) \rangle. \quad (2.27)$$

Assuming that the angle and action variables are uncorrelated Eq. (2.27) becomes:

$$\langle u^2(s) \rangle = 2\beta_u(s) \langle J_u \rangle \langle \cos^2 \psi_u(s) \rangle. \quad (2.28)$$

Considering that the angle variables are uniformly distributed from 0 to 2π , it is written:

$$\langle \cos^2 \psi_u(s) \rangle = \int_{s_0}^{s_0+C} \cos^2 \psi_u(s) ds = \int_0^{2\pi} \cos^2 \psi_u(\phi) d\phi = \frac{\pi}{2\pi} = \frac{1}{2}. \quad (2.29)$$

where for the integration the phase advance ϕ is used instead of the location s along the ring for convenience.

2. Basics of accelerator beam dynamics

Inserting Eq. (2.29) in Eq. (2.27) gives:

$$\langle u^2(s) \rangle = \beta_u(s) \epsilon_u, \quad (2.30)$$

where

$$\epsilon_u^{\text{geom}} = \langle J_u \rangle \quad (2.31)$$

is the geometric emittance of the bunch. Considering the same assumption Eq. (2.21) and Eq. (2.22) results to:

$$\langle u(s) u'(s) \rangle = -\alpha_u(s) \epsilon_u^{\text{geom}}, \quad (2.32)$$

$$\langle u'^2(s) \rangle = \gamma_u(s) \epsilon_u^{\text{geom}}. \quad (2.33)$$

Combining the above equations, the geometric emittance is expressed in terms of the particles' distribution as:

$$\epsilon_u^{\text{geom}} = \sqrt{\langle u^2(s) \rangle \langle u'^2(s) \rangle - \langle u(s) u'(s) \rangle^2} \quad (2.34)$$

which, also equals the square root of the determinant of the covariance or Sigma matrix of the particles' distribution:

$$\Sigma = \begin{pmatrix} \langle u^2(s) \rangle & \langle u(s) u'(s) \rangle \\ \langle u(s) u'(s) \rangle & \langle u'^2(s) \rangle \end{pmatrix} = \begin{pmatrix} \sigma_u^2(s) & \langle u(s) u'(s) \rangle \\ \langle u(s) u'(s) \rangle & \sigma_{u'^2(s)} \end{pmatrix} \quad (2.35)$$

The square root of the top-left element of the covariance matrix, σ_u , is defined as the rms beam size and is also a variable that is used extensively in accelerator physics. The definition of rms and of others of the statistical analysis can be found in Appendix A.

Figure 2.4 illustrates the concepts of emittance and rms beam size. It shows the phase space of a transverse Gaussian bunch along with the histograms of the u (top) and u' (right) variables at a particular point s along the ring. Each particle follows its individual ellipse (of different sizes but with the same orientation) depending on its initial conditions. The rms beam size, σ_u , and the rms

normalised momentum spread, $\sigma_{u'}$, are shown in the top and right histograms of Fig.2.4 with the blue vertical lines. This corresponds to the area of the ellipse enclosed in the blue line in the phase space plot and equals the rms or geometric emittance, ϵ_u^{geom} , as defined in Eq. (2.34).

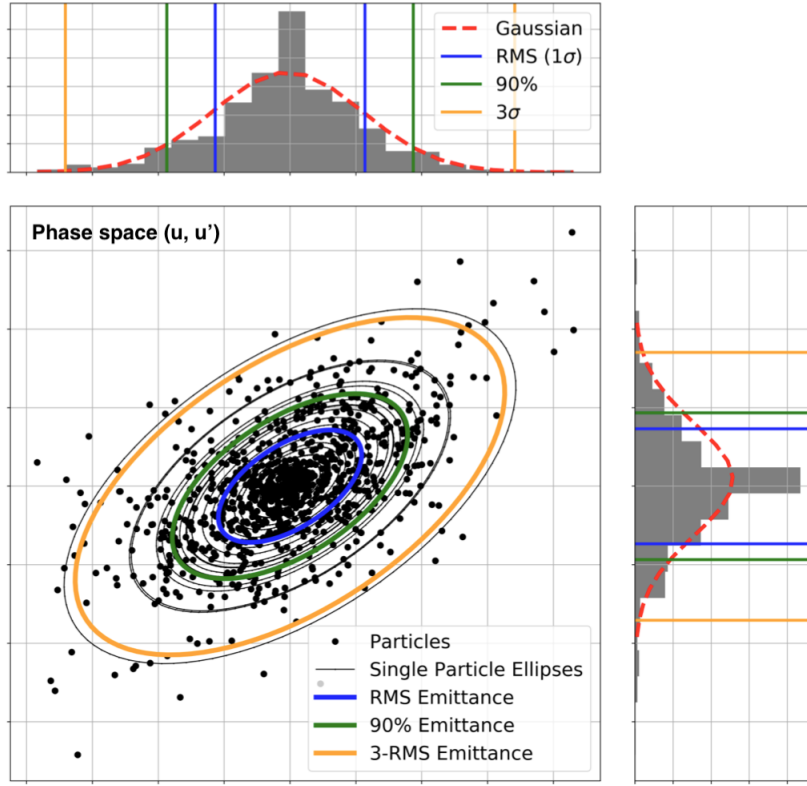


Figure 2.4: Transverse phase space of a Gaussian bunch. The figure is a courtesy of Tarsi Prebibaj [30].

It should be noted, that there are also other conventions to define the emittance such as the 90% emittance (green lines in Fig. 2.4) or the 3-sigma emittance (yellow lines in Fig. 2.4). However, here the term geometric emittance will refer to the rms geometric emittance.

According to Liouville's theorem [26], assuming that there are no interactions between the particles and that the energy of the beam is not changing, the geometric emittance remains constant and therefore is an invariant of bunch motion (similarly to the action J_u for the single-particle motion). The geometric emittance does not remain constant during acceleration, instead, the normalised emittance is defined as:

$$\epsilon_u = \beta_0 \gamma_0 \epsilon_u^{\text{geom}} \quad (2.36)$$

2. Basics of accelerator beam dynamics

The normalised emittance is conserved during acceleration and is often used as an alternative to the geometric emittance, especially in situations where the beam undergoes acceleration or deceleration. It is highlighted here, that throughout this thesis the term "emittance" will refer to the rms normalised emittance.

It is worth noting that for the simulation studies presented in this thesis, the emittance is computed using the statistical definition introduced in Eq. (2.34). In the experimental studies, the emittance is obtained from the rms beam size at a point in the beamline where the beta function is known. The procedure is explained in more detail in Chapter 5, but here we simply note that from Eqs. (2.30), (A.11) and (2.36), we can express the emittance as:

$$\epsilon_u = \frac{\sigma_u(s)^2}{\beta_u(s)} \beta_0 \gamma_0, \quad (2.37)$$

where $\sigma_u(s)$ is the rms beam size, $\beta_u(s)$ is the beta function, at specific location s along the accelerator and β_0, γ_0 are the relativistic parameters.

It should be highlighted that the emittance definitions of Eq. (2.34) (after normalisation with the relativistic parameters) and of Eq. (2.37) are equivalent.

Finally, despite Liouville's theorem, in a real accelerator there are various phenomena that change the emittance such as [31]: scattering by residual gas, intra-beam scattering, beam-beam scattering, stochastic or electron cooling, synchrotron radiation emission, filamentation due to non-linearities of the machine, space charge and noise effects. The studies in this thesis focus on the emittance growth due to noise effects (discussed in more detail in Chapter 3).

Off-momentum effects: dispersion

Up to now, the discussion was limited to on-momentum particles $\delta = 0$: their momentum equals the reference momentum, p_0 . In a more realistic beam, however, the momenta of the individual particles are spread around the reference momentum, p_0 . The "spread" of momenta (or simply "momentum spread") is described by the rms momentum deviation $\sigma_\delta = \sqrt{\langle \delta^2 \rangle}$. As an example, in the SPS machine, which is of interest for this thesis, σ_δ is in the order of magnitude of 10^{-4}

to 10^{-3} .

The response of the off-momentum particles to a given force, during their passage from the different magnets in an accelerator, varies with their momentum. Here their motion through the dipole magnets which leads to dispersion effects is discussed.

Particles with $\delta < 0$ ($\delta > 0$) undergo larger (smaller) deflections from the dipole magnets than the reference particle due to lower (higher) magnetic rigidity. Therefore, they travel along the accelerator performing betatron oscillations not around the reference trajectory but around a different closed orbit as illustrated in Fig. 2.5 which depends on their momentum deviation, δ . The change in the closed orbit with respect to the momentum deviation is called dispersion. It is evident that the dispersion introduces a coupling between the longitudinal and transverse planes.

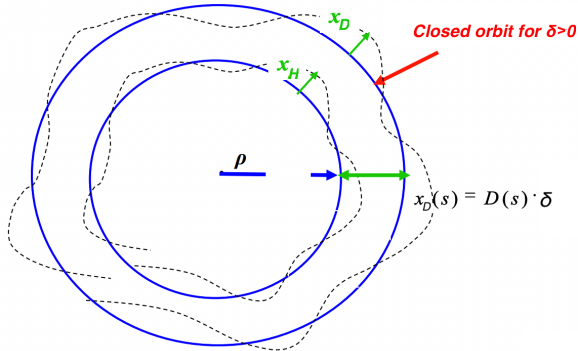


Figure 2.5: The closed orbit and the betatron oscillations around it in the presence of dispersion [32]

The following discussion is focused on the horizontal plane due to the fact that (as stated already) only vertical dipolar fields are considered.³ The equation of motion for the off-momentum particles has already been discussed in Eq. (2.9). Its solution is [28]:

$$x(s) = x_H(s) + D_x(s)\delta, \quad (2.38)$$

where $x_H(s)$ is the homogeneous solution shown in Eq. (2.21) (and corresponding here to betatron oscillations around the off-momentum closed orbit) and $D_x(s)$ is

³A corresponding discussion can be done for the vertical plane to obtain the vertical dispersion but it is out of the scope of this thesis.

2. Basics of accelerator beam dynamics

the dispersion function which can be expressed as:

$$D_x''(s) + K_x(s)D_x(s) = \frac{1}{\rho(s)}, \quad (2.39)$$

where $K_x(s) = \frac{1}{\rho^2(s)} + k_2(s)$ like in Eq. (2.12). As an example, the rms horizontal dispersion of the SPS machine is about 1.8 m (model value).

The dispersion function can be represented using the matrix formalism which therefore allows the addition of the dispersive contribution in the transfer matrix introduced in Eq. (2.19). This aspect is not discussed here, as it is not relevant for the studies in this thesis (the simulation studies consider zero dispersion function in both transverse planes). However, a detailed discussion can be found in Chapter 2 of Ref. [28].

The dispersion was introduced above as it affects the definition of the normalised beam emittance, which is used to compute the emittance values from experimental measurements (see Chapter 5). In particular, in the presence of dispersion the normalised beam emittance (Eq. (2.37)) becomes:

$$\epsilon_u = \frac{\sigma_u(s)^2 - \sigma_\delta^2 D_u^2(s)}{\beta_u(s)} \beta_0 \gamma_0, \quad (2.40)$$

where $\sigma_u(s)$ is the rms beam size, $\beta_u(s)$ is the beta function, $D_u(s)$ is the dispersion at a specific location s along the accelerator, σ_δ is the momentum spread and β_0, γ_0 the relativistic parameters. The subscript $u = (x, y)$ denotes the horizontal and vertical plane. The impact of the vertical dispersion is included here, as only the model vertical dispersion equals zero. In a real machine, vertical dispersion can be introduced by sources such as steering errors of the dipole or quadrupole magnets [33]. For reference, the rms vertical dispersion in the SPS machine is measured to be about 10 cm.

Additionally, the off-momentum particles receive different focusing due to gradient errors in the quadrupoles. This effect is known as chromaticity and is discussed in detail in the next Section 2.2.1.2 which focuses on non-linear beam dynamics.

2.2.1.2 Non-linear dynamics

Up to now, only linear elements (dipoles and quadrupoles) were considered as in theory they are sufficient to create a synchrotron. However, in a real machine non-linearities are also present due to factors such as imperfections in the magnets field and alignment, particles' momentum spread, and higher order magnets (sextupoles, octupoles, etc). Here, the preceding discussion is expanded to include the non-linear beam dynamics. The discussion is limited to the two effects that are important for the work presented in this thesis: the chromaticity and the detuning with transverse amplitude.

Chromaticity

We define the chromaticity as the variation of the betatron tune Q_u with the relative momentum deviation delta. This is a result of the fact that particles with $\delta < 0$ ($\delta > 0$) are focused more (less) strongly from the quadrupoles due to their smaller (larger) magnetic rigidity. The tune shift introduced by the chromaticity for each particle, $\Delta Q_u(\delta) = Q_u - Q_{u0}$, is:

$$\Delta Q_u(\delta) = \sum_{n=1}^m \frac{1}{n!} Q_u^{(n)} \delta^n, \quad (2.41)$$

where:

$$Q_u^{(n)} = \left. \frac{\partial^n Q_u}{\partial \delta^n} \right|_{\delta=0}, n \in \mathbb{N}, \quad (2.42)$$

denotes the chromaticity of order n . The studies in this thesis, are limited to the chromaticity at the first order in δ ($n = 1$) which is often called linear chromaticity. Note that the betatron tune shift of Eq. (2.41) is referred to as an "incoherent" tune shift, since each particle is affected differently, depending on its individual momentum deviation.

Large values of chromaticity can lead to instabilities and therefore to beam loss [28]. Sextupole magnets are typically used to control the natural chromaticity of a machine and achieve the desired values for its operation.

Similarly to the tune, the chromaticity is a property of the machine lattice.

Octupoles and detuning with amplitude

2. Basics of accelerator beam dynamics

Octupole magnets are most often used to increase the transverse tune spread of the beam particles to avoid resonances⁴ and instability effects⁵. This property, of providing incoherent betatron tune spread in a controlled way is used extensively in this thesis and therefore some further details are discussed in the following.

The betatron tune spread or linear detuning that is introduced by the octupoles is action-dependent in both transverse planes. In terms of the action variable it is written as follows:

$$\Delta Q_x(J_x, J_y) = 2(\alpha_{xx}J_x + \alpha_{xy}J_y), \quad (2.43)$$

$$\Delta Q_y(J_x, J_y) = 2(\alpha_{yy}J_y + \alpha_{yx}J_x), \quad (2.44)$$

where J_x, J_y the transverse action as introduced in Eq. (2.26), α_{xx}, α_{yy} and $\alpha_{xy} = \alpha_{yx}$ are the detuning coefficients with units $1/m$. The detuning coefficients depend on the octupoles strength, the beta functions at their location and the magnetic rigidity [35]. This detuning with the transverse action (or amplitude) is an incoherent effect as it depends on the individual action of each particle.

In the SPS and LHC rings, the octupoles are installed in families (focusing and defocusing) in order to avoid the excitation of resonances. They are usually referred to as "Landau octupoles" since they are used to create a betatron tune spread that provides the mechanism of Landau damping [36] (to stabilise the beam).

2.2.2 Longitudinal motion

In the longitudinal plane, the motion is parallel to the reference trajectory and is described by the co-ordinates (z, δ) . In the next paragraphs, only the basic concepts that are required for the explanation of the equations of motion are discussed, as the studies in this thesis mostly concern transverse beam dynamics. However, a complete discussion can be found in Chapter 9 of Ref. [27].

⁴Resonances in circular accelerators are a result of perturbation terms in the equation of motion once the perturbation frequency matches the frequency of the particles' oscillatory motion. The topic of resonances is out of the scope of this thesis, however, more details can be found in Chapter 16 of Ref. [27]

⁵Beam instabilities in an accelerator are a result of the interplay of the wakefields (which will be discussed in Section 2.3.1) and a perturbation (e.g. noise) on equations of motion of the beam particles. Similar to the resonances their detailed study is out of the scope of this thesis, however, more details can be found in Ref. [34].

Synchronous phase

The time that the reference particle needs to complete one complete revolution around the machine is called the revolution period, T_{rev} . Its angular revolution frequency is $\omega_{\text{rev}} = 2\pi/T_{\text{rev}}$ in rad/s or $f_{\text{rev}} = 1/T_{\text{rev}} = v_0/C = \beta_0 c/C$ in Hz, where v_0 the speed of the reference particle, β_0 the relativistic beta, c the speed of light and C the circumference of the accelerator.

In the longitudinal plane the acceleration and the focusing (in phase) of particles are achieved by the longitudinal time-dependent electric field of the main RF cavities:

$$E_{\text{RF}}(t) = E_A \sin(\phi_{\text{RF}} + \phi_s), \quad (2.45)$$

where E_A it the amplitude of the electric field, $\phi_{\text{RF}}(t) = \omega_{\text{RF}} t$ the phase of the RF system, ω_{RF} the angular frequency of the RF system and ϕ_s is the phase of the synchronous or reference particle. The angular frequency needs to be an integer multiple of the revolution frequency: $\omega_{\text{RF}} = h\omega_{\text{rev}}$, where h is called the harmonic number. The harmonic number (number of RF cycles per revolution) defines the maximum number of bunches that can be accelerated (or stored) in the ring. In a synchrotron during the energy ramp the angular frequency increases in order to follow the increasing revolution frequency.

Assuming that the synchronous or reference particle arrives at the RF cavity at phase ϕ_s every turn, the energy gain equals:

$$\Delta E_0 = eV_{\text{RF}} \sin(\phi_s), \quad (2.46)$$

where V_{RF} the amplitude of the RF cavity voltage. The rest of the particles will arrive at the RF cavity at phases $\phi = \phi_s \pm \delta\phi$ and they will gain or lose a different amount of energy per turns which equals: $\Delta E_p = eV_{\text{RF}} \sin(\phi)$.

Dispersion effects

As discussed in the previous chapter, in the presence of dispersion a particle with a momentum offset, δ , from the reference particle will have a different closed orbit of different length (see Fig. 2.5). This change of the orbit length with respect to the momentum offset of each particle is described with the momentum compaction

2. Basics of accelerator beam dynamics

factor [37]:

$$\alpha_p = \frac{\Delta C/C}{\delta} = \frac{1}{C} \oint_C \frac{D_x(s)}{\rho(s)} ds, \quad (2.47)$$

where C is the circumference of the accelerator and $D_x(s)$ and $\rho(s)$ are the horizontal dispersion and bending radius respectively at a given point s .

With the change of the closed orbit length due to the momentum offset the revolution frequency of the particles also changes. The change of the angular frequency depending on the momentum offset is described with the phase slip factor:

$$\eta_p = -\frac{\Delta\omega/\omega_0}{\delta} = \alpha_p - \frac{1}{\gamma_0^2} = \frac{1}{\gamma_{tr}^2} - \frac{1}{\gamma_0^2}, \quad (2.48)$$

where ω_0 is the angular frequency of the reference particle, γ_0 is the Lorentz factor and $\gamma_{tr} = 1/\sqrt{\alpha_p}$ is called the transition energy. When $\gamma_0 < \gamma_{tr} \Rightarrow \eta_p < 0$ ($\gamma_0 > \gamma_{tr} \Rightarrow \eta_p > 0$) and the machine operates below (above) transition. For the nominal optics configuration, the SPS machine always operates above transition as $\gamma_{tr} = 22.8$ which is smaller than the relativistic gamma even for the injection energy ($\gamma_0 = 27.7$ at 26 GeV).

Phase stability and synchrotron oscillations

Even though the particles arrive at different times in the RF cavity, they stay in the vicinity of the reference particle thanks to the effect of longitudinal or phase focusing, which is explained by the concept of phase stability [38, 39, 40]. Its principle is illustrated in Fig. 2.6 for a machine operating above transition. Above transition a particle with $\delta < 0$ will follow a shorter closed orbit (than the reference trajectory) and therefore it will arrive at the RF cavity slightly earlier, than the reference particle and hence it will see a larger voltage. Therefore, it will be accelerated more than the reference particle and subsequently it will need less time to complete the next revolution and, over a number of revolutions, will fall back longitudinally towards the reference particle. The situation is the opposite for a particle with $\delta < 0$.

In particular, the non-synchronous particles oscillate around the phase of the synchronous particle performing synchrotron oscillations (similarly to the betatron oscillations in the transverse plane). It is worth mentioning, that a

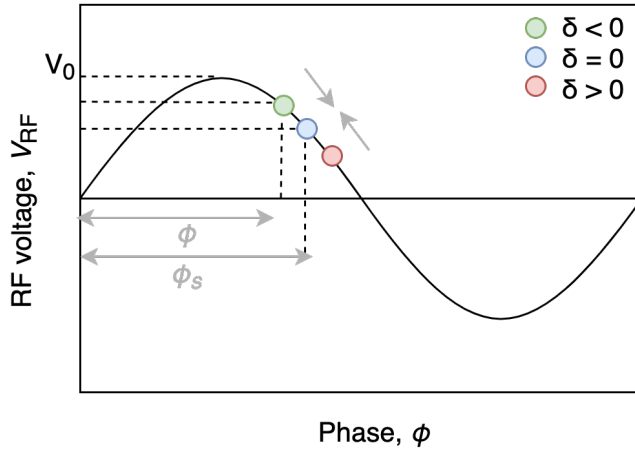


Figure 2.6: Phase stability for particles in a circular accelerator which operates above transition.

complete synchrotron oscillation can take many (~ 100) turns, in contrast to the betatron oscillations (of which there are usually many complete oscillations per turn). The equations of motion for a particle passing through a system of synchronised RF cavities located around the accelerator are [26]:

$$z' = -\eta_p \delta, \quad (2.49)$$

$$\delta' = -\frac{qV_{RF}}{cp_0C} \left(\sin \phi_s - \sin \left(\phi_s - \frac{\omega_{RF} z}{c} \right) \right), \quad (2.50)$$

where $z' = dz/ds$, $\delta' = d\delta/ds$, e is the charge of a proton, c is the speed of light, p_0 is the reference momentum, C is the circumference of the machine, ω_{RF} is the angular frequency of the RF system, ϕ_s is the phase of the synchronous particle and η_p is the phase slip factor.

The synchrotron tune, Q_s , is the number of synchrotron oscillations performed during one complete revolution around the machine and is computed as follows [26]:

$$Q_s = \frac{1}{2\pi} \sqrt{-\frac{eV_{RF}}{cp_0} \frac{\omega_{RF} C}{c} \eta_p \cos \phi_s}. \quad (2.51)$$

2.3 Collective effects

Up to now, the motion of the particles was studied neglecting the interaction between them within the bunch. Collective effects in an accelerator describe the

2. Basics of accelerator beam dynamics

phenomena in which the motion of the particles depends on their interaction with each other or with electromagnetic fields. Examples are beam-beam interactions, space charge effects, wakefields and intra-beam scattering [41]. The collective effects usually become crucial for high-intensity beams as they can lead to instabilities⁶ which then may degrade beam quality, or lead to beam losses. In either case, the performance of the accelerator can be adversely affected. The discussion here is limited in the description of the wakefields and the impedance they are relevant for the studies presented in this thesis. A complete overview of the collective effects can be found in [26, 41].

2.3.1 Wakefields and impedance

The discussion in this section is based in the discussion in Refs. [26, 34, 42, 43, 44].

Wakefields

The charged particles within a beam interact electromagnetically with their surroundings in the beam pipe such as the resistive vacuum pipe walls, the RF cavities, etc. If these structures are not smooth (presence of discontinuities) or not perfectly conducting the interaction with the charged particles will result in electromagnetic perturbations called wakefields. Studying the effects of the wakefields is crucial as they act back on the beam affecting the beam dynamics.

For the study of the wakefields, it is considered that each particle acts as a source of wakefields for the rest of the particles⁷ which are called witnesses. In the ultrarelativistic regime (which is also the regime of these studies) the wakefields from a source particle act only on the particles behind it, hence the term "wake". Wakefields can also act back on the charge generating them when that charge returns to a given location in a storage ring over successive turns. This is the multi-turn effect of the wakefields. In this thesis, only the multi-turn effect from

⁶A beam is called unstable when one of its co-ordinates $(x, x', y, y', z, \delta)$ undergoes exponential growth. Further details on the beam instabilities can be found in Ref. [34]

⁷In studying collective effects, the terms "source particle" and "witness particle" are sometimes used for particles generating wakefields and particles affected by the wakefields, though in reality all charges act as sources of wakefields, and are affected by them

the resistive wall will be considered as it is the only one that has a significant impact on the dynamics.

The longitudinal and transverse wakefields can often be treated separately. In the following only the transverse components will be discussed as the focus of the thesis is on the transverse beam dynamics.

Wake functions

Consider two particles of charge q_1 and q_2 moving with ultrarelativistic speed through a structure of length L as shown in Fig. 2.7 [42]. The particle of charge q_1 is the source particle while the witness particle of charge q_2 travels behind it at a constant distance z . $(\Delta x_1, \Delta y_1)$ are the transverse offsets of charge q_1 , and $(\Delta x_2, \Delta y_2)$ are the transverse offsets of charge q_2 from the symmetric axis of the beam pipe. From the interaction of the source particle with the structure of length L a wakefield is generated.

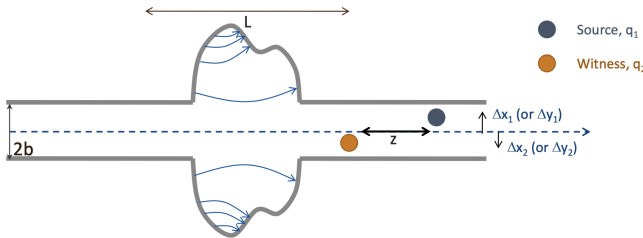


Figure 2.7: Wakefield interaction, where the source particle (blue) affects the witness particle (yellow) travelling at a distance z behind it [42]. $(\Delta x_1, \Delta y_1)$ and $(\Delta x_2, \Delta y_2)$ are the transverse offsets of the source and witness particles respectively.

The wakefields in time domain are described with the concept of wake functions, $W_u(z)$, where $u = (x, y)$ denotes the horizontal and vertical wakefunction. The wakefunction can be expressed as a series of its multipole components as follows:

$$W_u(\Delta u_1, \Delta u_2, z) = W_u^{\text{const}}(z) + W_u^{\text{dip}}(z)\Delta u_1 + W_u^{\text{quad}}(z)\Delta u_2 + o(\Delta u_1, \Delta u_2), \quad (2.52)$$

where $u = (x, y)$ and $W_u^{\text{const}}(z)$, $W_u^{\text{dip}}(z)$, $W_u^{\text{quad}}(z)$ are the transverse constant, dipolar, and quadrupolar wakefunctions respectively. Last, $o(\Delta u_1, \Delta u_2)$ is the higher order term however only the first-order terms will be considered for the rest of the analysis.

2. Basics of accelerator beam dynamics

The dipolar and quadrupolar wakefunctions were named after the way they act on the witness particle. The dipolar wakefunction acts like a dipole magnet: its impact is the same regardless of the transverse position of the witness particle; it depends only on the position of the source particle. The quadrupolar wakefunction acts like a quadrupole magnet: its impact increases linearly with the transverse position of the witness particle (independent of the position of the source particle).

The constant term can change the closed orbit while the dipolar and quadrupolar terms can modify the tunes [43]. The dipolar term is often referred to as a driving term for coherent instabilities. The quadrupolar term is often referred to as the detuning term as it modifies the betatron frequencies of individual particles.

The effect of the wakefields on the witness particles can be modeled as the following kicks on the transverse normalised momentum [45]:

$$\Delta u'_2 = \int_0^L F_u(s, z, \Delta u_1, \Delta u_2) ds = -q_1 q_2 [W_u^{\text{const}}(z) + W_u^{\text{dip}}(z)\Delta u_1 + W_u^{\text{quad}}(z)\Delta u_2], \quad (2.53)$$

where F_u is the transverse force of the wakefield over the length L . If the structure leading to the wakefield is axially symmetric, then the constant term of the wakefunction is zero.

Beam coupling impedance

The beam coupling impedance is the frequency spectrum of the wakefields in a given component or section of the accelerator. The impedance can be obtained from the wakefunction through a Fourier transform and vice versa as shown below [44]:

$$W_u(z) = -\frac{i}{2\pi} \int_{-\infty}^{+\infty} Z_u(\omega) e^{i\omega z/c} d\omega, \quad (2.54)$$

$$Z_u(\omega) = \frac{i}{c} \int_{-\infty}^{+\infty} W_u(z) e^{-i\omega z/c} dz, \quad (2.55)$$

where $u = (x, y)$, i is the imaginary unit and c is the speed of light.

In order to study the beam dynamics effects due to wakefields, impedance models of the particle accelerators have been developed. Details on how an impedance model is built can be found in Ref. [43]. The impedance model for the SPS is discussed in Chapter 7 while its implementation in the simulations is discussed in

Section 2.5.1.

Head-tail modes

The Vlasov equation [46] is often used to describe the beam motion in the presence of wakefields as it allows its mode representation (in frequency domain): the beam motion is described by a superposition of modes. Solving the Vlasov equations for the coupled system between the particle motion (synchrotron and betatron) and wakefield kicks the eigenmodes and eigenfrequencies are obtained. These modes are often referred to as headtail modes as they are related to the betatron phase shift between the head and tail of the bunch in a synchrotron. The headtail modes can either be stable, damped, or excited; in the latter case, they evolve into instabilities. For the beam to become unstable the wakefield kicks (source of energy) need to be synchronized with the bunch motion (e.g. with chromaticity) [42].

Sacherer formulae and complex coherent frequency shift

One of the impedance induced effects, that is relevant for the studies of the thesis, is the complex tune shift. The complex tune shift can be computed analytically based on the Vlasov formalism [46] through the use of perturbation theory. Formulae expressing the results were derived by Sacherer [47, 48].

The headtail modes introduce an exponential dependence on the amplitude of the bunch centroid as follows [45]:

$$u(t) \propto e^{i(\Omega_{u0}^{(l)} + \Delta\Omega_u^{(l)})t} = e^{i(\Omega_{u,0}^{(l)} + \Delta\Omega_{u,\text{re}}^{(l)})t} e^{-\Delta\Omega_{u,\text{im}}^{(l)}t}, \quad (2.56)$$

where $\Omega_{u0}^{(l)}$ is the real-valued, unperturbed frequency of mode l , and $\Delta\Omega_u^{(l)} = \Delta\Omega_{u,\text{re}}^{(l)} + i\Delta\Omega_{u,\text{im}}^{(l)}$ is the complex coherent frequency shift introduced by the beam impedance. From Eq. (2.56) it can be seen that the the real part $\Delta\Omega_{u,\text{re}}^{(l)}$ modifies the oscillation frequency. The second term $e^{-\Delta\Omega_{u,\text{im}}^{(l)}t}$ illustrates that the amplitude of the motion grows for $\Delta\Omega_{u,\text{im}}^{(l)} < 0$ (unstable bunch) and is damped for $\Delta\Omega_{u,\text{im}}^{(l)} > 0$ (stable bunch).

The complex coherent frequency shift for the mode l for a bunched beam is

2. Basics of accelerator beam dynamics

(Chapter 6 in Ref. [44]):

$$\Delta\Omega_u^{(l)} = \Omega_{u0}^{(l)} - \omega_{u0} - l\omega_s = -\frac{1}{4\pi} \frac{\Gamma(l+1/2)}{2^l l!} \frac{N_b r_0 c^2}{\gamma_0 T_{\text{rev}} \omega_{u0} \sigma_z} i Z_{\text{eff}}, \quad (2.57)$$

where ω_{u0} and ω_s are the unperturbed betatron and synchrotron frequencies, $\Gamma(x)$ is the gamma function, N_b is the number of particles in the bunch, $r_0 = 1.535 \cdot 10^{-16}$ is the classical radius of the proton, c is the speed of light, γ_0 is the relativistic gamma, T_{rev} is the revolution period, σ_z is the rms bunch length, i is the imaginary unit and Z_{eff} is the effective impedance.

The effective impedance Z_{eff} is computed as follows:

$$Z_{\perp \text{eff}}^{(l)} = \frac{\sum_{p=-\infty}^{+\infty} Z_{\perp}^{(l)}(\omega_p) h_l(\omega_p - \omega_\xi)}{\sum_{p=-\infty}^{+\infty} h_l(\omega_p - \omega_\xi)}, \quad (2.58)$$

where $\omega_p = (p + Q_u)\omega_0$ is the discrete spectrum of the transverse bunch oscillations with $-\infty < p < +\infty$ for a single bunch (which is the case in the following studies) or several bunches oscillating independently and $\omega_\xi = (\xi \omega_u)/\eta_p = Q' \omega_0 / \eta_p$ is the chromatic angular frequency with η_p being the phase slip factor.

Last, h_l , is the power spectral density (definition in Appendix C) of a Gaussian bunch of l azimuthal mode. h_l is described by:

$$h_l(\omega) = (\omega \sigma_z / c)^{2l} e^{-(\omega \sigma_z / c)^2}, \quad (2.59)$$

where σ_z is the rms bunch length and c the speed of light.

It should be highlighted that all the parameters inserted in Eq. (2.57), Eq. (2.58) and Eq. (2.59) should be converted in CGS (centimetre–gram–second) units. For the conversion from SI to CGS system the following relations are useful:

$$1[\Omega] = \frac{1}{9} \cdot 10^{-11} [\text{s}/[\text{cm}], \quad (2.60)$$

where Ω (Ohm) is the SI unit of resistance.

Finally, the imaginary part of the impedance, leads to a real coherent frequency shift

which can be expressed in tune units as follows [49]:

$$\Delta Q_u^{(l)} = \frac{\Delta\Omega_{u,\text{re}}^{(l)}}{\omega_{\text{rev}}}, \quad (2.61)$$

where $\Delta\Omega_{u,\text{re}}^{(l)}$ the real part of the complex tune shift as defined in Eq. (2.57). The real part of the impedance, leads to an imaginary coherent frequency shift which is also known as the growth (+ sign) or damping (- sign) rate of the mode l and is given by [49]:

$$1/\tau_u^{(l)} = -\frac{\Delta\Omega_{u,\text{im}}^{(l)}}{T_{\text{rev}}}, \quad (2.62)$$

where $\Delta\Omega_{u,\text{im}}^{(l)}$ the imaginary part of the complex tune shift as defined in Eq. (2.57). The $1/\tau_u^{(l)}$ is expressed in units of 1/turns.

The real coherent tune shift appears proportional to the beam intensity. This dependence plays a crucial role in the CC studies discussed in the following.

2.4 Optics models for accelerators

For the study of beam dynamics, it is essential to know the detailed arrangement of the magnets (position and strength) in the lattice, which will be referred to as optics. The optics also provide information on the twiss parameters and phase advances along the ring.

MAD-X [50] is a code which is used extensively for the design and simulation of the accelerators at CERN. The official optics repositories of the CERN machines can be found in Ref. [51].

SPS optics

The studies presented in this thesis are performed for the nominal SPS optics for the LHC filling which are called Q26 optics as the integer part of the tune in both planes is 26. The model for the Q26 optics can be found in the official CERN repository [52] and will be referred to as the nominal SPS model in this thesis. The values of the optics parameters in what follows correspond to the model values unless stated otherwise.

2.5 Tracking simulation codes

In this section the two tracking simulation codes used in this thesis to study the noise-induced emittance growth are presented. Both codes are macroparticle tracking libraries that simulate the particle motion in the six-dimensional (6D) phase space $(x, x', y, y', z, \delta)$. The first code (PyHEADTAIL) performs tracking between interaction points around a circular accelerator at which the particles receive kicks from magnetic elements or from collective effects. The second code (Sixtracklib), uses the detailed optics model of the machine for the tracking. In both cases, the tracking is performed with the use of transfer matrices.

2.5.1 PyHEADTAIL

PyHEADTAIL [53] is an open-source 6D macroparticle tracking code, developed at CERN, which was originally designed to study collective effects in circular machines and to be easily extensible with custom elements. Details on its implementation and its features can be find in Refs. [54, 55]. Below the main steps of a simulation are listed:

1. **Machine initialisation:** The accelerator ring is split into a number of segments of equal length, after each of which there is an interaction point⁸ (IP). At the interaction points the macroparticles experience kicks from various accelerator components (feedback system, multipoles etc) or from collective effects such as the wakefields. The machine parameters, such as the circumference, the betatron and synchrotron tunes and the optics at the interaction points are defined. It should be noted that PyHEADTAIL uses smooth approximation which means that only a few segments are defined per turn.
2. **Bunch initialisation:** A particle bunch is represented by a collection of macroparticles, each of which represents a clustered collection of physical particles. Each macroparticle is described by four transverse (x, x', y, y') and two longitudinal coordinates (z, δ) , a mass and an electric charge. For the

⁸It should be clarified that this is not an "interaction point" in the sense of collision between counter-circulating beams.

studies presented in this thesis 10^5 macroparticles are sufficient for an accurate representation of the bunch, unless it is stated otherwise. There are various distributions available. In this thesis the simulations are performed using a Gaussian distribution in transverse and longitudinal planes.

3. **Transverse tracking:** In the transverse plane, the macroparticles are transported from one interaction point to another (e.g. from IP0 to IP1) following the matrix formalism of Eq. (2.19). The linear transfer matrices, M , introduced in Eq. (2.20) take into account the optics parameters at the beginning and the end of the corresponding segment. The phase advance, for each segment equals:

$$\Delta\psi_{u,\text{IP0}\rightarrow\text{IP1}} = Q_u \frac{L}{C}, \quad (2.63)$$

where Q_u is the transverse betatron tune, C the machine circumference and L the length of the corresponding segment. It should be noted that if no detuning source is added (see next step) the matrix M is the same for all particles.

4. **Chromaticity and detuning with transverse amplitude:** The chromaticity (up to higher orders) and amplitude detuning are implemented as a change of the phase advance of each individual particle as follows (example for the horizontal plane):

$$\Delta\psi_{x,i\text{IP0}\rightarrow\text{IP1}} = \Delta\psi_{x,\text{IP0}\rightarrow\text{IP1}} + (\xi_x^1 \delta_i + \alpha_{xx} J_{x,i} + \alpha_{xy} J_{y,i}) \frac{\Delta\psi_{x,\text{IP0}\rightarrow\text{IP1}}}{2\pi Q_x}, \quad (2.64)$$

where $i = 1, \dots, N$ with N being the number of macroparticles, $\Delta\psi_{x,\text{IP0}\rightarrow\text{IP1}}$ is the phase advance for all macroparticles defined in the previous step, ξ_x^1 the horizontal chromaticity of first order (see Eq. (2.42) for $n = 1$) normalised to the betatron tune, α_{xx} and α_{xy} are the detuning coefficients, while J_x and J_y are the horizontal and vertical actions of the macroparticle. Therefore, in the presence of detuning the elements of the M matrix (introduced in Eq. (2.20)) are different for every particle.

5. **Longitudinal tracking:** The longitudinal coordinates are advanced once per

turn after solving numerically the equations of motion introduced in Eq. (2.49) and Eq. (2.50). The motion can be linear or not (non-linear RF system). The studies presented in this thesis use the linear longitudinal tracking.

6. **Transverse impedance effects:** In PyHEADTAIL, wakefield kicks are used to implement the effect of the transverse impedance in the time domain. To improve the computational efficiency, the total impedance of the full machine is lumped at one of the interaction points along the ring and the kicks are applied to the macroparticles once per turn. Additionally, instead of computing the wakefield kicks from each particle to the rest individually, the bunch is divided into a number of slices longitudinally and the macroparticles in each slice receive a wakefield kick generated by the preceding slices⁹ [56]. This is illustrated schematically in Fig. 2.8. A large number of slices is required such as the wakes can be assumed constant within the slice. A high number of macroparticles is also needed in order to avoid statistical noise effects caused by undersampling [54]. For the studies presented, 500 slices are used over a range of three rms bunch lengths in both directions from the bunch center with the bunch being represented by 10^6 macroparticles (instead of 10^5 required for simulations without impedance effects).



Figure 2.8: Longitudinal bunch slicing for the implementation of wakefield kicks in PyHEADTAIL. Without the slicing technique (left) the wake kicks on the red macroparticle are generated from all the green macroparticles resulting in computationally expensive simulations. Instead, when the bunch is sliced longitudinally (right) the wake kicks on the macroparticles in the red slice i are generated by the macroparticles in the green slices j , decreasing significantly the computation time. The figures are courtesy of M. Schenk [55]

The wakefield kicks are computed using a convolution of the wake function with the moments of each particle. The wake functions are available from

⁹This is valid in the ultrarelativistic scenario when no wakefield is generated in front of the bunch. The condition applies for the SPS experiments described in this thesis, performed at 270 GeV.

detailed impedance model of the machine which are obtained from a combination of theoretical computations and electromagnetic simulations and can be imported in PyHEADTAIL in form of tables. Typically, the impedance model of an accelerator is provided normalised with the average value of the horizontal and vertical beta functions over the machine at the respective plane. Therefore the transverse beta functions at the location where the wakefield kicks are applied on the beam must equal these average values. More details on the SPS impedance model are provided in Section 7.1.

7. **Data acquisition:** The updated macroparticle coordinates after each turn are available at IP0 for post-processing. Typically, 10^5 turns are required for the noise-induced emittance growth simulations presented in this thesis.

Figure 2.9 shows a graphic representation of the accelerator model and the tracking procedure supporting the steps described above.

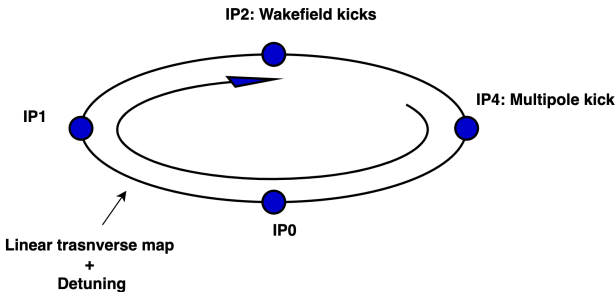


Figure 2.9: Graphical representation of the accelerator model and tracking procedure in PyHEADTAIL (inspired by the graphs in Refs. [55, 57]). In this example the ring is split in four segments separated by the interaction points (IPs). Wakefield and multipole kicks are applied to the macroparticles in IP2 and IP4. The macroparticles are transported between the IPs by a linear transfer map (which can include detuning effects) in the transverse plane. The longitudinal coordinates are updated once per turn.

2.5.2 Sixtracklib

Sixtracklib [58] is a library for performing single charged particle simulations developed at CERN. It simulates the motion of the particles in the six-dimensional (6D) phase space. The individual trajectories are computed taking into account the interactions with all the magnetic elements in the machine using the detailed design optics model described in Section 2.4. The particles advance from one

2. Basics of accelerator beam dynamics

element to the other with transfer maps. Simulations with Sixtracklib are time efficient as the library can run on Graphical Processing Units (GPUs). Further details on Sixtracklib implementation and usage can be found in Ref. [59] and Ref. [60].

Since Sixtracklib code was not used as extensively as PyHEADTAIL for the studies presented here, and was not modified or extended in any way where it was used, we do not give further description here, but refer the reader to the references mentioned above.

3 | Theory of Crab Cavity RF noise-induced emittance growth

This section describes the theoretical formalism which predicts the transverse emittance growth in the presence of CC RF noise. First, it introduces the concept of noise in accelerator beam dynamics. The second section focuses on the CC noise both in amplitude and phase and it provides the equations with which one can estimate the noise-induced emittance growth. The last section, comments briefly on the experiments that took place in KEKB as it's the only time this issue was treated in the past.

3.1 Noise

In particle accelerators, a major issue of concern is the presence of external noise as it leads to transverse emittance growth, particle losses and limits the beam lifetime. Examples of noise sources are ripples in the power converter ripples which lead to fluctuations of the magnetic fields, ground motion, and various instruments in the accelerator structure such as the transverse damper and the Crab Cavities.

From the various noise sources that are present in an accelerator, this thesis focuses on the dipolar noise and mainly on the CC noise. Dipolar noise is the one produced by the majority of the noise sources and is constant along the bunch, i.e. all the particles are affected the same way. On the other hand, the way the CC noise affects the particles depends on their longitudinal position within the bunch (more details in the following paragraphs).

Past studies [61, 62, 63] have dealt with this type of noise in the context of the

3. Theory of Crab Cavity RF noise-induced emittance growth

induced emittance growth theoretically and in simulations. It has been shown, that the noise can be modeled as a sequence of random kicks (stochastic process) that affect the particles within a bunch by changing their transverse momentum each turn as follows:

$$u'_1 = u'_0 + \Delta u', \quad (3.1)$$

where $u = (x, y)$ denoting the horizontal and vertical plane and $\Delta u'$ is the change of the momentum due to the noise in units of rad. In this thesis the term "noise" refers to the above mentioned stochastic process.

3.2 Crab Cavity noise and emittance growth

As already mentioned in the Introduction (Section 1.3) the presence of noise in the CC low-level RF system is an issue of major concern for the HL-LHC project as it results in transverse emittance growth and subsequently in loss of luminosity. To this end, in 2015, P. Baudrenghien and T. Mastoridis developed a theoretical model [63] which predicts this transverse emittance growth induced by CC noise focusing on the HL-LHC scenario. In particular, the model assumes a hadron machine, zero synchrotron radiation damping, long bunches (in the order of cm), and white RF noise (discrete spectral lines are excluded). Additionally, it is assumed that the CC RF zero phase is set at the center of the bunch.

White noise

In signal analysis, white noise is a random signal with the same amplitude (intensity) at all the frequencies which results in a constant power spectral density. For the computational analysis (i.e. simulation studies), the signals are sampled at a finite number of points which are called discrete-time signals. In discrete-time, the white noise can be considered as a sequence of uncorrelated random variables taken from a Gaussian distribution with zero mean and finite standard deviation. More details on the continuous and discrete time analysis and the term of the power spectral density can be found in Appendix C. The definition for the standard deviation of a distribution can be found in Appendix A.

It should be highlighted, that the above mentioned model is also applicable to the

SPS (where the same conditions apply), where the CCs will be tested before their installation in the LHC (Section 1.3). The equations and formulas from the theoretical model that are essential for the understanding of the studies are discussed below.

3.2.1 Crab Cavity amplitude and phase noise

The unperturbed instantaneous CC voltage equals the one of an ideal oscillator:

$$V_{\text{CC}}(t) = V_{0,\text{CC}} \sin(2\pi f_{\text{CC}} t), \quad (3.2)$$

where $V_{0,\text{CC}}$ is the peak amplitude of the CC voltage and f_{CC} the CC frequency. Equation (3.2) can be re-written as a function of the longitudinal position within the bunch z instead of time t as follows:

$$V_{\text{CC}}(z) = V_{0,\text{CC}} \sin\left(\frac{2\pi f_{\text{CC}}}{\beta_0 c} z\right), \quad (3.3)$$

where β_0 is the relativistic parameter and c is the speed of light. The above equation is obtained as: $z = v \cdot t \Rightarrow t = z/v = z/(\beta_0 c)$. In the presence of modulations in amplitude and phase Eq. (3.4) becomes (details in Appendix B.3):

$$V_{\text{CC}}(z) = V_{0,\text{CC}}(1 + \Delta A) \sin\left(\frac{2\pi f_{\text{CC}}}{\beta_0 c} z + \Delta\phi\right), \quad (3.4)$$

where $\Delta\phi$ is the deviation from the nominal phase, $2\pi f_{\text{CC}} z / (\beta_0 c)$, and will be referred to as phase noise in the following. $\Delta A = \Delta V_{0,\text{CC}} / V_{0,\text{CC}}$ is the relative deviation from the nominal amplitude $V_{0,\text{CC}}$ and will be referred to as amplitude noise. The units of $\Delta\phi$ is rad² while ΔA has no units as it's a relative quantity.

In the calculation of the RF noise effects it is assumed that RF phase and amplitude noises are independent. The validity of this hypothesis depends on the actual architecture of the LLRF responsible for the regulation of the cavity field. This is presently being designed at CERN. Further details can be found in Ref. [15] of the above-mentioned publication of Baudrenghien and Mastoridis [63], but discussing them is out of the scope of this thesis.

3. Theory of Crab Cavity RF noise-induced emittance growth

To this end, and following the analysis in Ref. [63] and in accordance with Eq. (3.1) the phase and amplitude noise kicks on each particle within a bunch can be modeled as the following turn-by-turn kicks on the momentum:

$$\textbf{Amplitude noise: } u'_{j+1} = u'_j + \zeta_j A \sin\left(\frac{2\pi f_{CC}}{c\beta_0} z\right), \quad (3.5)$$

$$\textbf{Phase noise: } u'_{j+1} = u'_j + \zeta_j A \cos\left(\frac{2\pi f_{CC}}{c\beta_0} z\right), \quad (3.6)$$

where $j = \{0, \dots, N_{\text{turns}}\}$ denotes the turn number with N_{turns} being the total number of turns that the bunch experiences the noise. Furthermore, u' , with $u = (x, y)$, is the angle co-ordinate and z the longitudinal co-ordinate of each particle as defined in Eq. (2.3), f_{CC} is the CC frequency, c is the speed of light and β_0 the relativistic β . Moreover, $A = V_{0,CC}/(E_b \cdot \Delta A)$ or $A = V_{0,CC}/(E_b \cdot \Delta\phi)$ the scaling factor for the strength of amplitude or phase noise respectively. The typical value of A that will be used in the simulations later is 10^{-8} . Finally, ζ_j is the j th element of a drawn sample from a Gaussian distribution with mean 0, standard deviation 1 and size N_{turns} , such as the above kicks are uncorrelated (white noise).

Figure 3.1 and Fig. 3.2 provide a schematic visualisation of the amplitude and phase noise respectively along with the impact of their kicks on the particles. It can be seen that in the presence of amplitude noise the head and the tail of the bunch are kicked in opposite directions which results in intra-bunch oscillations. On the other hand, in the presence of phase noise, the particles in the bunch receive kicks that are in phase. This results in a shift of the bunch centroid which basically is a dipole or mode 0 motion.

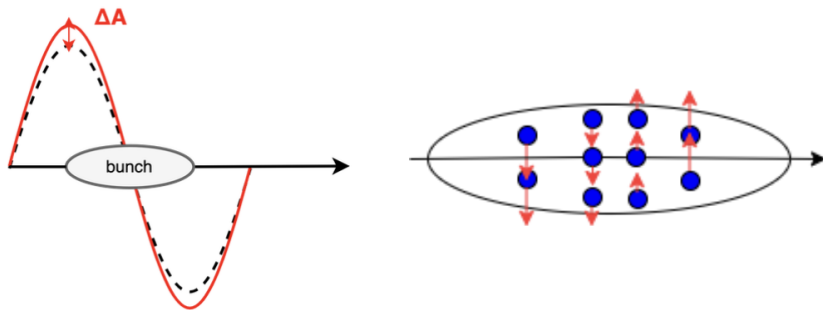


Figure 3.1: Modulation in amplitude or amplitude noise (left) and its impact on the particles within the bunch (right). The blue dots represent the individual particles while the red arrows indicate the direction of the noise kicks which act on them.

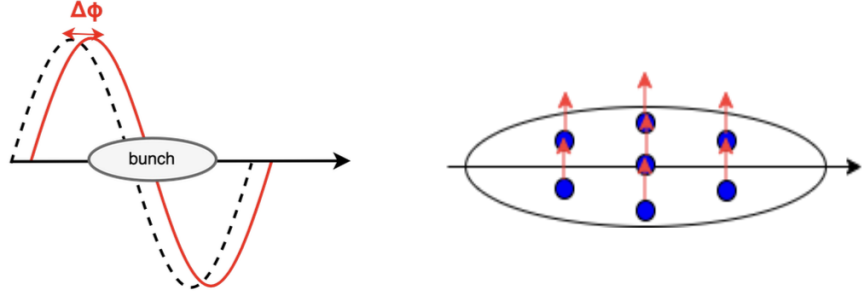


Figure 3.2: Modulation in phase or phase noise (left) and its impact on the particles within the bunch (right). The blue dots represent the individual particles while the red arrows indicate the direction of the noise kicks which act on them.

Finally, it is worth mentioning, that for the LHC, HL-LHC and SPS CCs the amplitude and phase RF noise are represented by white noise spectra. In that case, they can be considered as a sequence of uncorrelated random variables taken from a Gaussian distribution with zero mean and standard deviation $\sigma_{\Delta A}$ and $\sigma_{\Delta\phi}$ respectively which equals the total noise power (see Appendix B.2 for definitions).

3.2.2 Emittance growth formulas

As already mentioned, the theoretical formalism for predicting the transverse emittance growth in the presence of CC RF amplitude and phase noise was derived in Ref. [63]. The derivation assumes a single bunch, that the noise kicks are represented by a stochastic process, zero coupling between the horizontal and vertical plane, the beam energy is constant (no acceleration) and, CC RF zero phase is at the center of the bunch, $z = 0$ and a uniform noise spectrum across the betatron tune distribution which is also symmetric in negative and positive frequencies.

Taking these conditions into account, the emittance growth resulting from amplitude noise is estimated from:

$$\frac{d\epsilon_u^{\text{geom}}}{dt} = \beta_{u,\text{CC}} \left(\frac{eV_{0,\text{CC}} f_{\text{rev}}}{2E_b} \right)^2 C_{\Delta A}(\sigma_\phi) \sum_{k=-\infty}^{+\infty} S_{\Delta A}[(k \pm \bar{q}_u \pm \bar{q}_s) f_{\text{rev}}]. \quad (3.7)$$

3. Theory of Crab Cavity RF noise-induced emittance growth

For phase noise, the emittance growth is estimated from:

$$\frac{d\epsilon_u^{\text{geom}}}{dt} = \beta_{u,\text{CC}} \left(\frac{eV_{0,\text{CC}}f_{\text{rev}}}{2E_b} \right)^2 C_{\Delta\phi}(\sigma_\phi) \sum_{k=-\infty}^{+\infty} S_{\Delta\phi}[(k \pm \bar{q}_u)f_{\text{rev}}]. \quad (3.8)$$

In these formulas, which are valid for both transverse planes as $u = (x, y)$, $\beta_{u,\text{CC}}$ is the transverse beta function at the location of the CC, $V_{0,\text{CC}}$ the CC voltage, f_{rev} the revolution frequency of the beam, E_b the beam energy, and \bar{q}_u and \bar{q}_s the mean of the betatron and synchrotron tune distribution¹ where q_u, q_s (with lower case) denote the decimal part of the betatron and synchrotron tunes respectively. $S_{\Delta A}$ and $S_{\Delta\phi}$ are the power spectral densities (PSD) of the noise at all the betatron and synchrobetatron (for the amplitude noise case) sidebands and they are expressed in units of Hz^{-1} and $\text{rad}^2\text{Hz}^{-1}$, respectively. In particular, $k \in \mathbb{Z}$ is the harmonic number of the revolution frequency and the \pm signs refer to the upper (+) and lower (-) sidebands at each multiple of the revolution frequency, $k f_{\text{rev}}$, from the betatron tune.

The definition of the power spectral density along with the fundamental terminology for the signal-processing can be found in Appendix C². $C_{\Delta A}$ and $C_{\Delta\phi}$ are correction terms to account for the bunch length:

$$C_{\Delta A}(\sigma_\phi) = e^{-\sigma_\phi^2} \sum_{l=0}^{+\infty} I_{2l+1}(\sigma_\phi^2), \quad (3.9)$$

$$C_{\Delta\phi}(\sigma_\phi) = e^{-\sigma_\phi^2} \left[I_0(\sigma_\phi^2) + 2 \sum_{l=1}^{+\infty} I_{2l}(\sigma_\phi^2) \right], \quad (3.10)$$

with σ_ϕ the rms bunch length, in rad, with respect to the CC frequency f_{CC} , and $I_n(x)$ the modified Bessel function of the first kind.

Figure 3.3 illustrates the correction term for different values of bunch length for amplitude (left) and phase (right) noise. The SPS nominal bunch length used in the CC tests is shown in the orange for reference.

Comment on the use of the emittance growth formulas

Here some additional comments on the use of the Eq. (3.7) and Eq. (3.8) for

¹For white noise spectra the effect of noise is independent of the actual tune distribution, hence the use of the mean quantities. The generic formulas can be found in Ref. [63]

²In the Appendix amplitude and phase noise are noted with just α and ϕ , instead of ΔA and $\Delta\phi$, for simplicity.

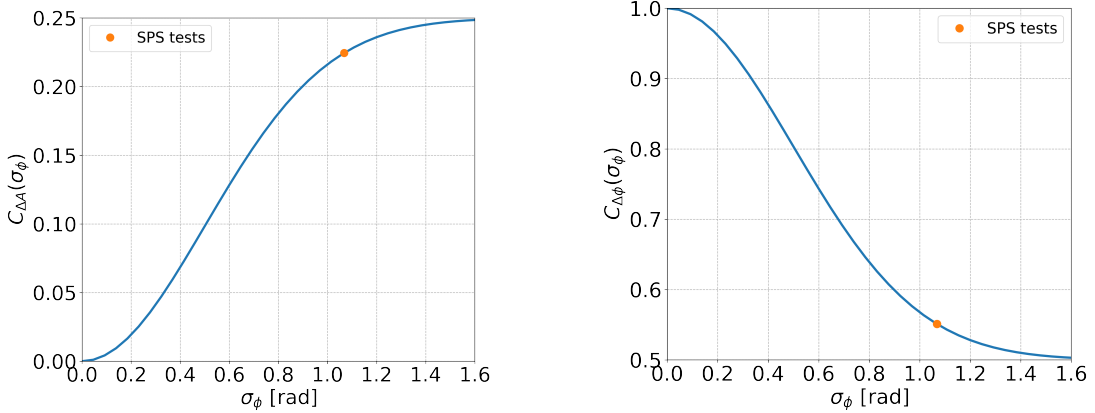


Figure 3.3: Correction term for amplitude (left) and phase (right) noise over a range of bunch length values.

predicting the emittance growth rate for both measurements and simulation studies of this thesis are made to facilitate the discussion in the following chapters.

In this thesis, the emittance growth in the vertical plane is addressed. The reason is that for both experimental campaigns that took place in 2018 and 2022, the CC module that was available provided a vertical deflection on the beam. For reference, the CC module which provides horizontal deflection is planned to be available by the end of 2022. Additionally the studies were performed for the SPS machine for which the parameters are listed in Table 5.1: $q_y = 0.18$, $f_{\text{rev}} = 43.38 \text{ kHz}$, and $q_s = 0.0051$.

To this end, the emittance growth induced by CC RF noise depends on the PSD value of the noise at the vertical betatron and synchrobetatron sidebands for the phase and amplitude noise case respectively (see Eq. (3.7) and Eq. (3.8)). The upper and lower sidebands of the first and second vertical betatron sidebands are observed in the following frequencies:

$$k = 0 : (0 \pm \bar{q}_y) f_{\text{rev}} = \pm 0.18 \times 43.38 \text{ kHz} \approx \pm 7.8 \text{ kHz}. \quad (3.11)$$

$$k = \pm 1 : (\pm 1 \pm \bar{q}_y) f_{\text{rev}} = (\pm 1 \pm 0.18) \times 43.38 \text{ kHz} \approx \begin{cases} -51.2 \text{ kHz and } -35.6 \text{ kHz}, & \text{if } k = -1 \\ 51.2 \text{ kHz and } 35.6 \text{ kHz}, & \text{if } k = 1 \end{cases}. \quad (3.12)$$

The upper and lower sidebands of the first and second vertical synchrobetatron

3. Theory of Crab Cavity RF noise-induced emittance growth

sidebands are observed in the following frequencies:

$$k = 0 : (0 \pm \bar{q}_y \pm \bar{q}_s) f_{\text{rev}} = (\pm 0.18 \pm 0.0051) \times 43.38 \text{ kHz} \approx \pm 8.02 \text{ kHz and } \pm 7.6 \text{ kHz.} \quad (3.13)$$

$$k = \pm 1 : (\pm 1 \pm \bar{q}_y \pm \bar{q}_s) f_{\text{rev}} = (\pm 1 \pm 0.18 \pm 0.0051) \times 43.38 \text{ kHz} \approx \\ \approx \begin{cases} -35.35, -35.79, -50.96, -51.40 \text{ kHz,} & \text{if } k = -1 \\ 35.35, 35.79, 50.96, 51.40 \text{ kHz,} & \text{if } k = 1 \end{cases}. \quad (3.14)$$

The experimental studies with CCs (more details in Chapter 5) were conducted with an artificial noise spectrum which was up to 10 kHz, which as it becomes clear from the Eqs. (3.11)- (3.14) is overlapping and therefore exciting only the first betatron and synchrobetatron sidebands, $k = 0$ (upper and lower).

In the simulations, the beam particles encounter the phase or amplitude noise kicks once per turn (more details in Chapters 6 and 7). This means that the sampling frequency of the noise spectrum in the frequency domain equals, $f_s = f_{\text{rev}} = 43.38 \text{ kHz}$. This means, that the frequency spectrum of the noise applied in the simulations extends from $-f_s/2 \approx -22 \text{ kHz}$ to $+f_s/2 \approx 22 \text{ kHz}$. Further explanation can be found in Appendix C and specifically in the Section B.4.3. Again, from Eqs. (3.11)- (3.14) it becomes clear that the noise kicks in the simulations excite only the first betatron and synchrobetatron sidebands for $k = 0$ (upper and lower).

To sum up, when using Eqs. (3.7) and (3.8) to predict the emittance growth rate due to CC RF noise, $k = 0$ will be considered.

3.3 Studies in KEKB

The CCs have been tested in the past with lepton beams in KEKB in Japan (further references on their operation were given in the Introduction). As expected, the sensitivity of the beam to the CC RF noise was also studied. However, there were significant differences in the conditions in the HL-LHC, LHC, and SPS. In particular, the studies in KEKB were conducted for lepton bunches (instead of hadron bunches), they were about an order of magnitude shorter than the ones of

the hadron machines (no effect from amplitude noise), and there was significant damping from the synchrotron radiation and the RF noise was characterised by a single spectral line (instead of white noise). Due to these differences, the studies at KEKB are not applicable to the studies presented in this thesis. Nevertheless, these studies can be found in Ref. [64] and they consist the only other available experience with CC RF noise but going into further details is out of the scope of this thesis.

Now that the theoretical formulas for the CC RF noise-induced emittance growth have been introduced, they will be used through the following chapters for comparison against numerical simulations and experimental measurements (in the SPS) for developing confidence in the theoretical model and its predictions for the HL-LHC.

4 | Calibration of the Crab Cavities for the SPS tests in 2018

This chapter focuses on the setup and the calibration of the CCs in the SPS for the 2018 tests. The objective is to provide a full understanding of the operational aspects of the CCs in the SPS and clarify the measurement of the CC voltage.

The presented studies were performed by the author in addition to the first round of analysis in 2018. They were motivated by the results of the experimental campaign (Chapter 5), which appeared to differ significantly from the theoretical predictions without apparent reason. As the reason for that discrepancy was not understood, having a closer look and reviewing the procedure of the CC voltage calibration was essential, given that it is one of the most crucial parameters for the emittance growth studies (see Chapter 3, Eq. (3.7) and Eq. (3.8)).

The chapter is structured as follows: Section 4.1 describes the installation of the CC system in the SPS. Thereafter, Section 4.2 elaborates on details for their operation in the SPS machine. In Section 4.3, the use of the Head-Tail (HT) monitor as the main diagnostic in the CC tests is discussed, focusing on the reconstruction of the CC voltage from its reading. Last, Section 4.4 provides a characterisation of the beam based CC voltage measurement and defines the voltage amplitude and its uncertainty.

4.1 Crab Cavities' installation in the SPS

For the SPS tests two prototype CCs of the Double Quarter Wave (DQW) type, which will be referred to as CC1 and CC2 throughout this thesis, were fabricated by

CERN and were assembled in the same cryomodule, shown in Fig. 4.1 [22]. For its installation an available space was found at the SPS Long Straight Section 6 (SPS-LSS6) zone. As this section is also used for the extraction of the beam to the LHC, the cryomodule was placed on a mobile transfer table [65] which moved the cryomodule in the beamline for the CC tests and out of it for the usual SPS operation without breaking the vacuum.

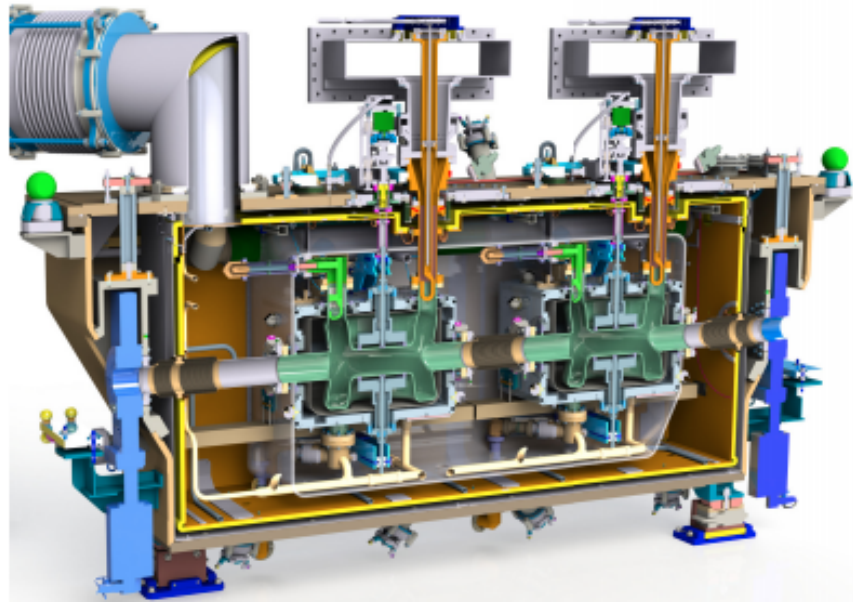


Figure 4.1: Cross section view of the CC cryomodule [22]. It has a total length of 3 m [66] and at its core there are the two DQW cavities, which are illustrated with light green color.

The main CCs parameters are listed in Table 4.1. Their location along the SPS ring is also indicated, in case someone would like to repeat the analysis described in this thesis.

4.2 Operational considerations

For the beam tests with CCs in the SPS the approach regarding the energy ramp and the adjustment of the phasing with the main RF system needed to be evaluated and they are briefly discussed here.

Energy ramp

SPS receives the proton beam at 26 GeV from the PS. It was found that the ramp to

4. Calibration of the Crab Cavities for the SPS tests in 2018

Table 4.1: Crab Cavities design parameters for the SPS tests in 2018.

Parameter	Value	
	CC1	CC2
crabbing plane	vertical	vertical
s-location*	6312.72 m	6313.32 m
CC voltage, V_{CC}	≤ 3.4 MV	≤ 3.4 MV
CC frequency, f_{CC}	400.78 MHz	400.78 MHz
Horizontal / Vertical beta function, $\beta_{x,CC} / \beta_{y,CC}$	29.24 m / 76.07 m	30.31 m / 73.82 m
Horizontal / Vertical alpha function, $\alpha_{x,CC} / \alpha_{y,CC}$	-0.88 m / 1.9 m	-0.91 m / 1.86 m
Horizontal / Vertical dispersion, $D_{x,CC} / D_{y,CC}$	-0.48 m / 0 m	-0.5 m / 0 m

* The s-location is referred to the location of the elements along the SPS ring with respect to the start of the lattice i.e. element QF10010 which is a focusing quadrupole. The s-location is given to allow the studies to be reproduced.

higher energies could not be performed with the CC on, as the beam was getting lost while crossing one of the vertical betatron sidebands due to resonant excitation [67, 68]. Therefore, it was established that the acceleration has to be performed with the CC off and its voltage must be set up only after the energy of interest has been achieved. It is worth noting that this approach will also be used in the HL-LHC.

Crab Cavity - main SPS RF synchronisation

It was important to ensure that during the "coast" the beam will experience the same kick from the CC each turn. In other words the SPS main RF system operating at 200 MHz needed to be synchronous with the CC operating at 400 MHz. Due to the larger bandwidth of the SPS main RF system the CC was used as a master. Therefore the CC was operating at a fixed frequency and phase, while the main accelerating cavities were adjusted to the exact half of the CC frequency and were re-phased so that they become synchronous with the crabbing signal. For the studies at higher energies the synchronisation took place at the end of the ramp shortly after the cavity was switched on [67].

4.3 SPS Head-Tail monitor as the main diagnostic

The SPS is equipped with a high bandwidth pick-up of approximately 2 GHz allowing to resolve the intra-bunch motion. This instrument is called Head-Tail (HT) monitor and was originally designed for measuring chromaticity and

transverse instabilities. However, in the SPS CC tests, the HT monitor was the main diagnostic device deployed for the demonstration of the crabbing and the measurement of the CC voltage (explained in details in Section 4.4). Therefore its use as a crabbing diagnostic should be explained here. The methods and procedures described in this section were developed at CERN and they are described here for the completeness of the thesis.

In the first part of this section some general information on the instrument along with example signals will be presented. Subsequently, the post processing of the HT signal in the presence of the CC will be discussed. Last, the calibration of the CC voltage from the HT data is described and the visualisation of the crabbing is displayed. The experimental data presented in this section were acquired, on May 30, 2018 (time-stamp: 13:51:05), at the SPS injection energy of 26 GeV with only one CC, CC1, at phase $\phi_{CC} = 0$ (this means that the particle at the center of the bunch doesn't receive any transverse deflection) for simplicity. That energy of 26 GeV was chosen to provide a better understanding of the methods used as the orbit shift from the CC kick is stronger and thus more visible than at higher energies.

4.3.1 General information

As already mentioned, the HT monitor is a high bandwidth version of a standard beam position monitor, which means that it can measure the transverse displacement within the bunch. This makes it ideal for the measurement of the intra-bunch offset caused from the CC kick. Its reading consists of the sum (Σ) and the difference (Δ) of the electrode signals of a straight stripline coupler (Fig. 4.2) [69, 70] over a defined acquisition period. The sum signal is the longitudinal line density while the difference signal corresponds to the intra-bunch offset. The system operates on timescales such that the signals are given as a function of the position within the bunch.

The raw signals from the HT monitor require a specific post-processing procedure [70], in order to provide useful information. Figure 4.3 shows some example signals obtained from the HT monitor after the basic post-processing is applied. Moreover, Fig. 4.4 shows a 2D representation of the HT monitor reading. It

4. Calibration of the Crab Cavities for the SPS tests in 2018

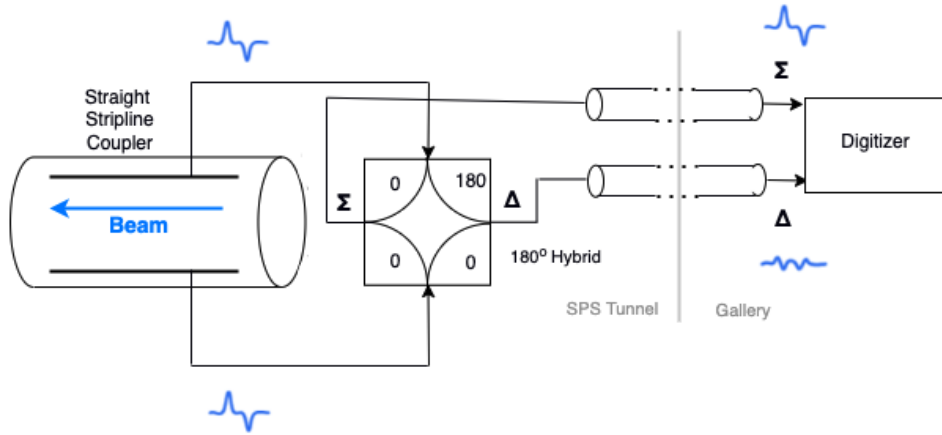


Figure 4.2: Diagram of the SPS HT monitor [70]. The beam is passing through a straight stripline coupler which is followed by a 180° hybrid. This configuration provides the sum (Σ) and the difference (Δ) signal of the two electrodes.

is worth noting here that in the specific example a clear modulating pattern in time of the vertical intra-bunch offset (vertical Δ) signal is observed. This is a result of the phase slip between the CC and the main RF system because they are not yet synchronised.

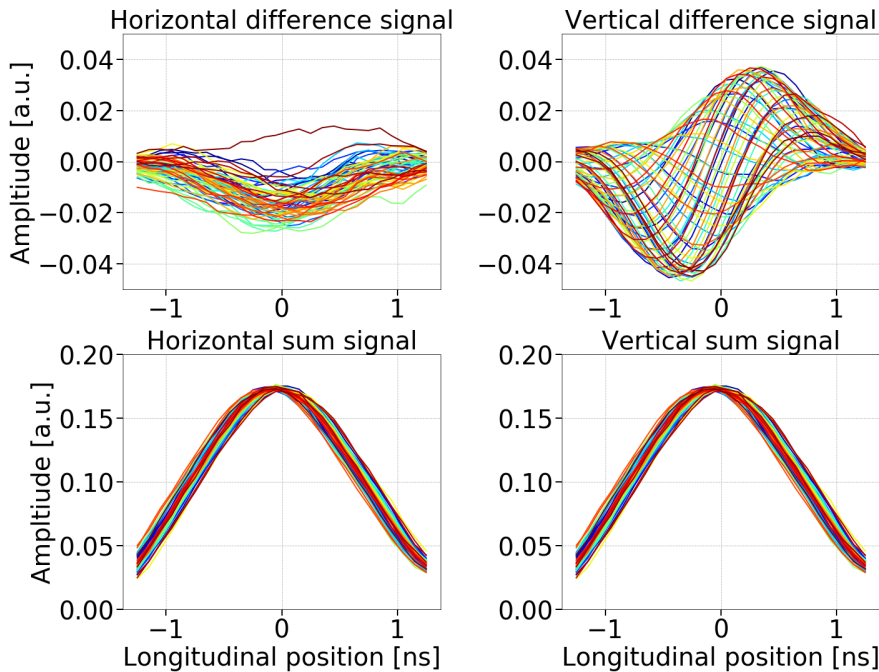


Figure 4.3: Example difference and sum signals (top and bottom plots, respectively) from the HT monitor, in time scale, with respect to the longitudinal position within the bunch over several SPS revolutions, after the basic post processing [70] but before the baseline correction. The different colors indicate the signals from different turns (every 100 turns).

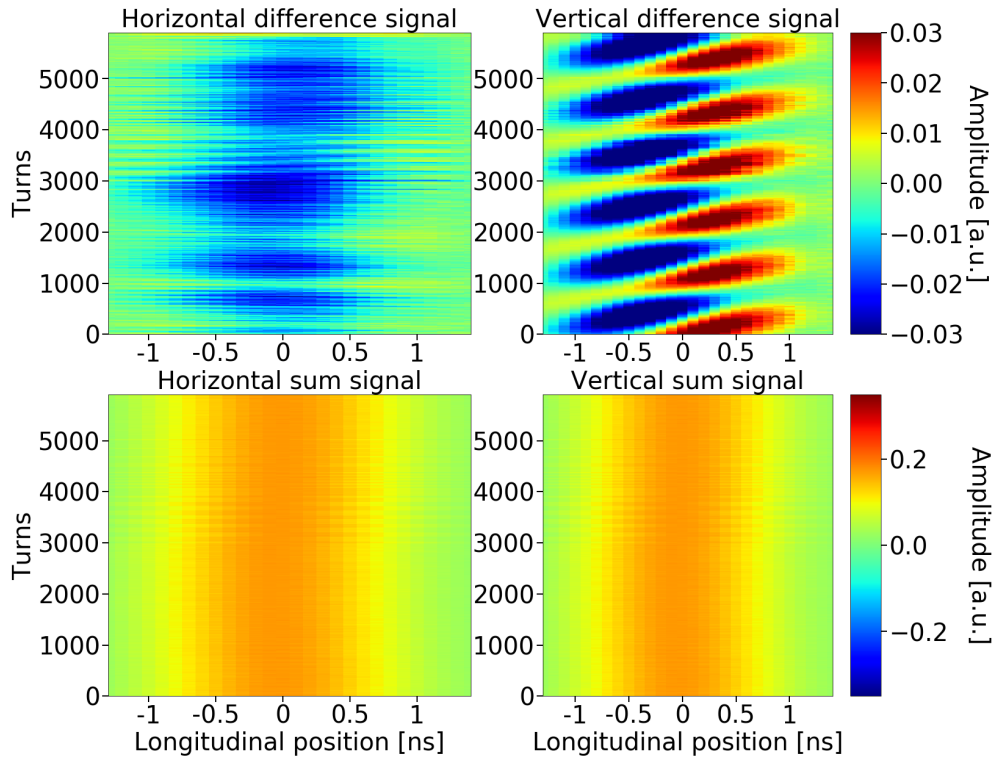


Figure 4.4: 2D representation of example difference and sum signals with respect to the longitudinal position within the bunch obtained from the HT monitor over several SPS revolutions.

4.3.2 Post processing in the presence of Crab Cavities

To obtain useful information from the HT monitor signal in the presence of the CCs there are a few steps that differ from the standard post processing procedure and they are described below.

Head-Tail monitor baseline correction

The HT monitor measurement has a baseline on the difference signal which needs to be removed. The baseline is a result of orbit offsets and non-linearities of the instrument and is constant from turn to turn [70]. Therefore, during the normal post processing procedure (without CCs), the baseline is computed as the mean of the difference signals over all turns and then the correction is achieved by subtracting this static offset from the signal of each turn. However, in the SPS tests, where the CCs are well synchronised with the main RF system (Section 4.2), the crabbing signal is also a static intra-bunch position offset and thus would also be removed with the usual method. Because of technical limitations it was not feasible to switch off the CC for those kind of measurements. Thus, the following

4. Calibration of the Crab Cavities for the SPS tests in 2018

technique was used.

For the CC experiments a reference measurement had first to be made with the CC not being synchronous with the main RF system. The baseline was computed as the mean of the difference signals over this reference period and subsequently it was subtracted from the average of the difference signals acquired after the synchronisation (Fig 4.5). The datasets before and after synchronisation are easily distinguishable in the 2D HT monitor reading as displayed in Fig. 4.6

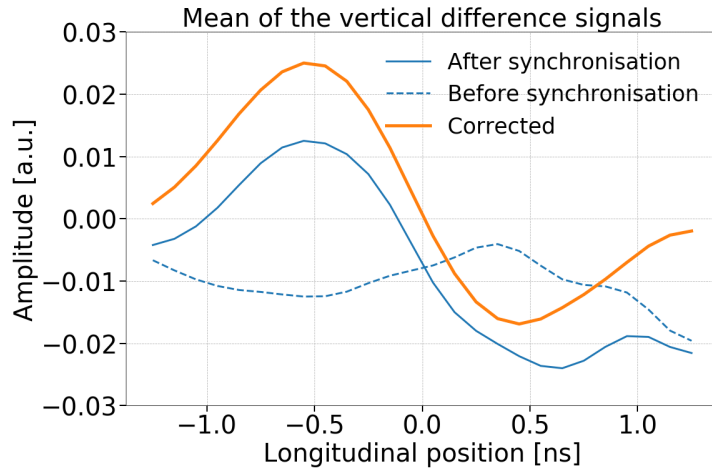


Figure 4.5: HT monitor baseline correction for the SPS CC tests. The baseline signal (blue dashed line) refers to the mean of the difference signals acquired before the CC - main RF synchronisation. The measured signal (blue solid line) corresponds to the mean of the difference signal acquired after the synchronisation. Last, the corrected signal (orange solid line) is obtained after subtracting the baseline from the measured signal.

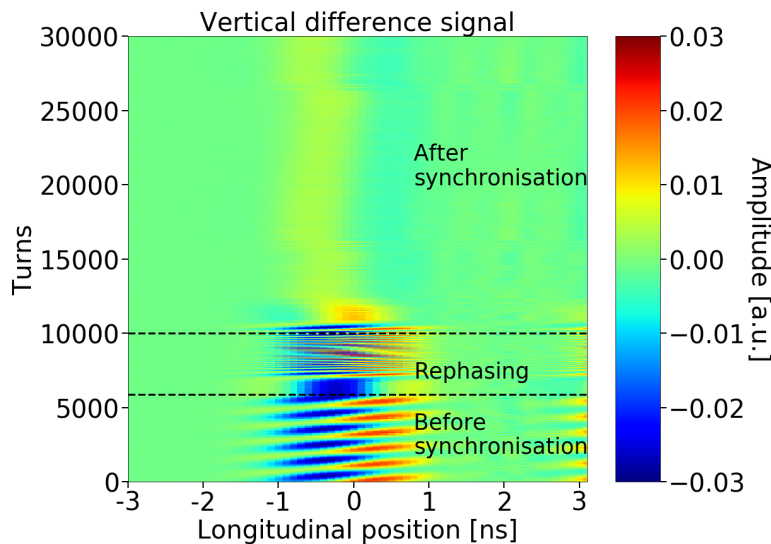


Figure 4.6: HT acquisitions before and after the synchronisation of the SPS main RF with the CC.

Head-Tail monitor scaling

The last step to make the HT acquisitions meaningful is to convert the measured intra bunch offset (the mean of the difference signals following phase synchronisation and baseline correction) from arbitrary units to millimeters. The scaling is achieved by dividing by the mean of the sum signals (which is a function of the position along the bunch and is calculated for each point individually over many turns) after the synchronisation and with a normalisation factor which is provided by the calibration of the HT monitor [71]. The normalisation factor for the SPS was measured at 0.1052 in 2018 [72]. Figure 4.7 shows the intra-bunch offset from the CC kick in millimeters and after the baseline correction.

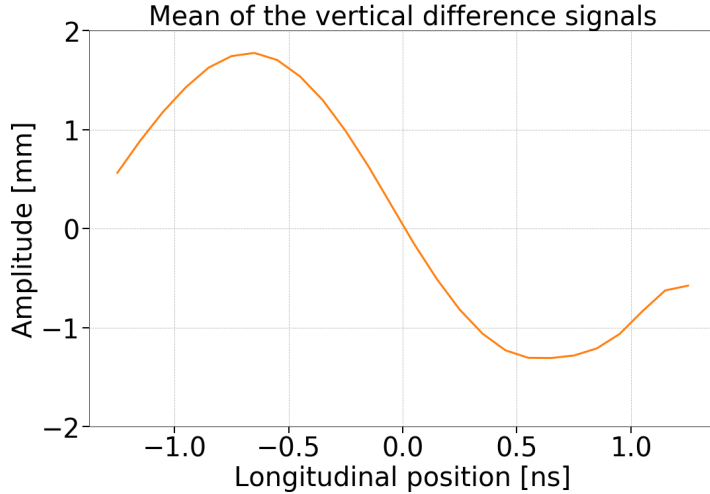


Figure 4.7: Intra-bunch offset from the CC kick expressed in millimeters after the removal of the baseline.

4.3.3 Crab Cavity voltage reconstruction

This section discusses the reconstruction of the CC voltage from the HT monitor signal. First, Eq. (4.1) was used to calculate the CC kick, θ , required to reconstruct the measured intra-bunch offset. Equation (4.1), which is obtained from Eq. (1) from chapter 4.7.1 in Ref. [73], gives the vertical orbit shift (in meters) from the CC kick, θ , at the HT monitor location as follows:

$$\Delta y_{HT} = \frac{\sqrt{\beta_{y,HT}}}{2 \sin(\pi Q_{y0})} \theta \sqrt{\beta_{y,CC}} \cos(\pi Q_{y0} - |\psi_{y,HT} - \psi_{y,CC}|), \quad (4.1)$$

where β_y is the beta function, Q_{y0} is the tune, and $|\psi_{y,HT} - \psi_{y,CC}|$ is the vertical

4. Calibration of the Crab Cavities for the SPS tests in 2018

phase advance (in tune units) between the CC and the HT monitor. The same applies for the horizontal plane. The subscripts HT and CC indicate quantities at the location of the HT monitor and CC respectively.

The CC voltage is then reconstructed from the CC kick which is written as $\theta = -\frac{qV_{CC}(t)}{E_b}$, where q is the charge of the particle, E_b the beam energy and $V_{CC}(t) = V_{CC} \sin(2\pi f_{CC} t + \phi_{CC})$ is the voltage that a particle experiences while passing through the CC. In the context where the HT monitor measures the signal as a function of time, t , the voltage in the above formula is expressed accordingly as $V_{CC}(t)$, where $t = 0$ the center of the bunch.

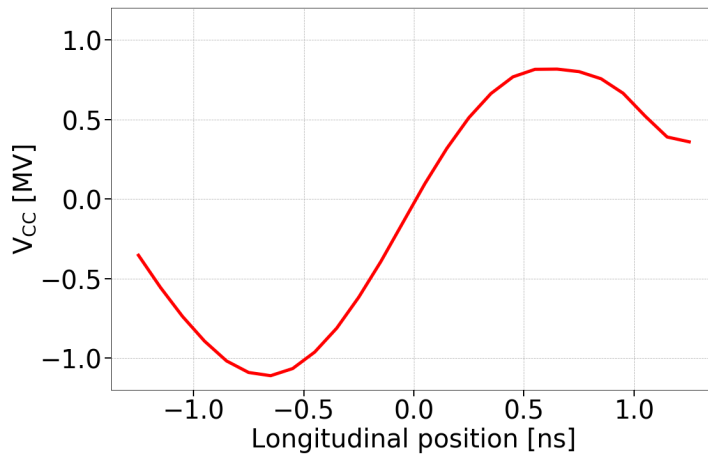


Figure 4.8: CC voltage reconstruction from the HT monitor.

It should be noted here, that the measured intra-bunch offset, Δy_{HT} , is inserted in Eq. (4.1) after removing the baseline and converting it to millimeters as discussed in Section 4.3.2. Figure 4.8 illustrates the cavity voltage computed from the HT signals shown already in this section. The corresponding beam and optic parameters are listed in Table 4.2.

4.3.4 Demonstration of crabbing with proton beams

Additionally, the measurements from the HT monitor were used for reconstructing the crabbing and representing schematically the beam projection in the transverse plane. The technique for reconstructing the crabbing was developed at CERN in 2018 and was extensively used throughout the experimental campaign with CCs since (together with the calibrated voltage) it gives a straightforward estimate of the applied CC kick, as illustrated in Fig. 4.9.

Table 4.2: Parameters for computing the CC voltage from the example HT monitor measurements discussed in this chapter.

Parameter	Value
Beta function at the HT monitor, $\beta_{y,HT}$	49.19 m
Phase advance to the HT monitor*, $\psi_{y,HT}$	$15.68 \times 2\pi$
Beta function at the CC1, $\beta_{y,CC1}$	76.07 m
Phase advance to the CC1*, $\psi_{y,CC1}$	$23.9 \times 2\pi$
Vertical betatron tune, Q_{y0}	26.18
Beam energy, E_b	26 GeV

* The phase advances are measured from the start of the lattice which is considered the element QE10010 that is a focusing quadrupole.

To obtain this schematic representation, which in practice is a density plot showing the effect of the CC kick on the beam, one needs to multiply the measured longitudinal profile (the mean of the sum signals acquired after phase synchronisation) with the measured intra-bunch offset, mean of the difference signals acquired after the synchronisation. An example of this is shown in Fig. 4.7. For the transverse plane a gaussian distribution is considered with σ obtained from the wire scanner (addressed in more detail in the following section). The color code of Fig. 4.9 is normalised to the maximum intensity within the bunch.

4.4 Characterisation of measured Crab Cavity voltage

This section gives the definitions of the amplitude of the beam-based measurement of the CC voltage and its uncertainty that will be used in this thesis. Additionally, their dependence on the CC phase is discussed for completeness.

4.4.1 Definitions of the amplitude and the uncertainty of the measurement

The voltage amplitude, V_{CC} , is obtained from a sinusoidal fit on the reconstructed voltage, $V_{CC}(t)$, from the HT monitor reading. The standard procedure of least squares fitting (see Appendix section A.2) is followed. In particular, $V_{CC}(t)$ is fitted with the following three-parameter (V_{CC} , ϕ_{CC} , k) model function which also

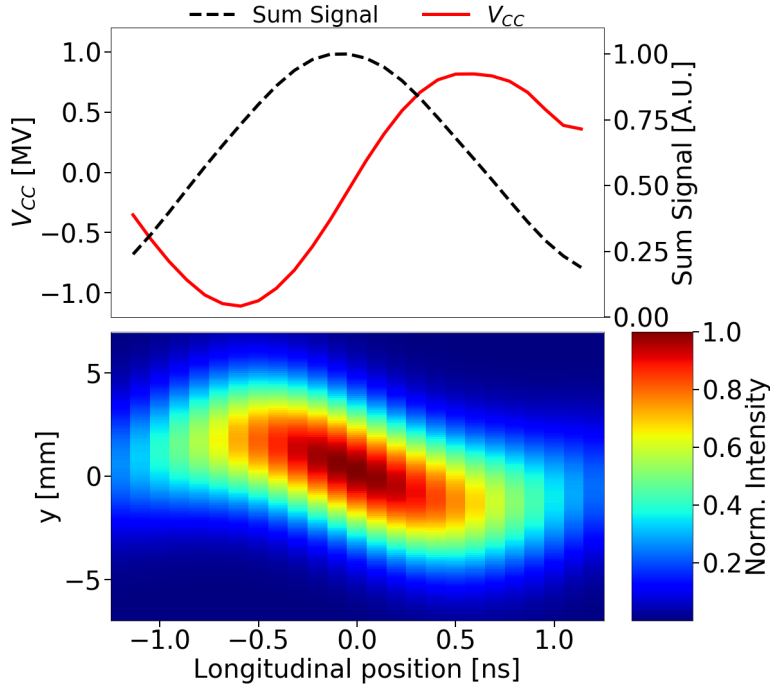


Figure 4.9: Demonstration of the crabbing from the HT monitor signal. CC voltage and sum signal (longitudinal line density) measured from the HT monitor (top) together with the density plot (bottom) which visualises the effect of the CC kick on the beam.

provides the CC phase and voltage offset:

$$f(x) = V_{CC} \sin(2\pi f_{CC}x + \phi_{CC}) + k, \quad (4.2)$$

where V_{CC} is the amplitude of the CC voltage, ϕ_{CC} the CC phase and k the voltage offset. The fit is performed for a fixed CC frequency, as the operational value is well known and in particular it equals, $f_{CC}=400.78$ MHz. The offset parameter is added to the model function as it is clear from Fig. 4.8 and 4.9 that the reconstructed CC voltage, $V_{CC}(t)$, is not centered around zero. The asymmetry seems to be a result of the HT monitor pick up and cable response [74]. However its origin is not yet fully understood and will have to be addressed in the future.

In order to obtain results that correspond to the experimental conditions the following constraints are imposed to the fit. First the voltage amplitude, V_{CC} , is requested to always be positive and higher than 0.7 MV. Furthermore, the part of the signal that corresponds to the tails of the bunch is excluded from the fit in order not to degrade its quality. Consequently, only the part of the signal for which the

corresponding normalised sum signal is above 0.4 is used for the fit.

Fig. 4.10 shows the result of the fit for the same signal that was analysed in the previous section. As indicated on the top of the plot, the red solid line corresponds to the reconstructed CC voltage, while the blue solid line corresponds to the result of the sinusoidal fit. It can be seen that only the part of the signal for which the normalised sum signal (black dashed line) is above 0.4 is used. Finally the blue dashed line shows the result of the fit after the voltage offset is subtracted, so that is centered around zero. The parameter values obtained from the fit are given in the legend. Last, the density plot is also shown at the bottom of the figure for a complete visualisation of the crabbing.

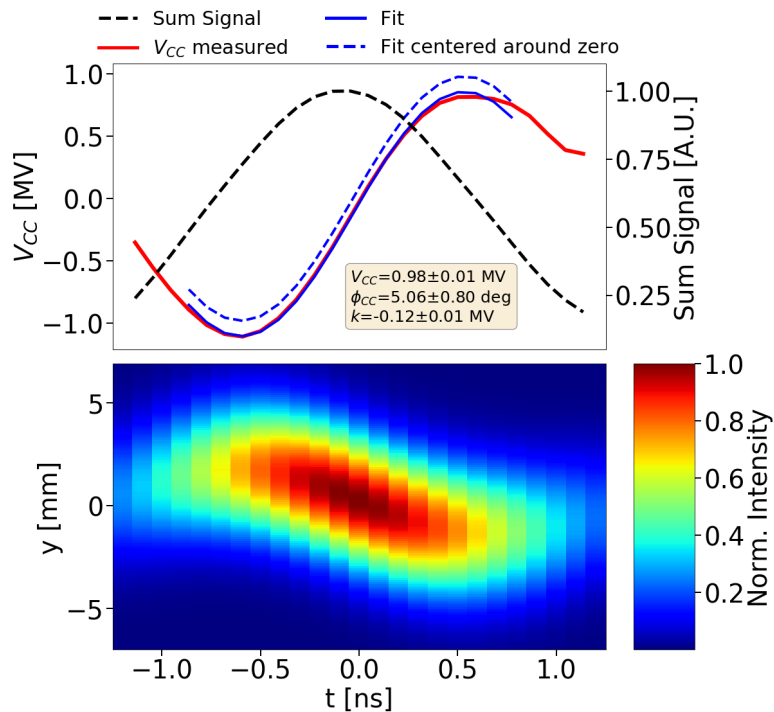


Figure 4.10: Demonstration of the sinusoidal fit on the HT monitor reading in order to obtain the CC parameters. A four-parameter sinusoidal fit is performed using Eq. (4.2) in order to obtain the amplitude, V_{CC} , the frequency, f_{CC} , the phase, ϕ_{CC} , and the voltage offset, k . The fit results are given in the yellow box.

In this thesis, the uncertainty on the measured voltage amplitude, ΔV_{CC} is defined as the absolute value of the voltage offset, k , instead of the error of the fit on the voltage amplitude. This is because the voltage offset depicts better the uncertainty of the voltage seen by the beam, V_{CC} . Therefore, for the analyzed example here the CC voltage was measured to be $V_{CC} = 0.98 \text{ MV}$ and its uncertainty $\Delta V_{CC} =$

0.12 MV.

4.4.2 Dependence of the crab cavity voltage and offset on the phase

The impact of the CC phase on the voltage experienced by the beam and on the uncertainty of its measurement was also studied experimentally. Data for the study were collected on 30 May. 2018, at the SPS injection energy of 26 GeV for a range of different settings of the phase of CC1. The results are summarised in Fig. 4.11.

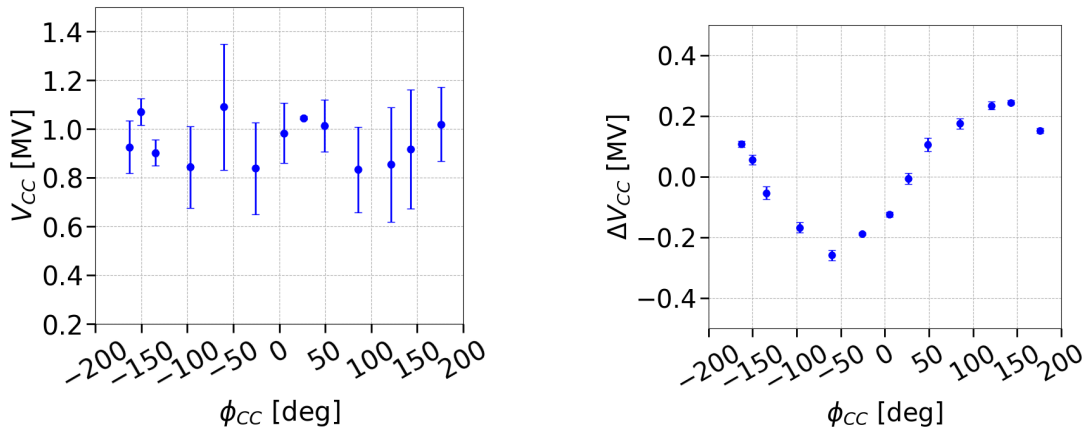


Figure 4.11: Phase scan with CC1 at 26 GeV. The sensitivity of the measured CC voltage (left) and its uncertainty (right) on the phase is studied. The error bars of the voltage, V_{CC} , indicate the uncertainty, ΔV_{CC} . The error bars of the uncertainty, ΔV_{CC} , and the phase, ϕ_{CC} , correspond to the error of the respective fit result (see Appendix A.2). The error bars are not visible here as they are smaller than the markers.

In the left plot the error bars of the voltage, V_{CC} , indicate the uncertainty, ΔV_{CC} . In the right plot, the error bars of the uncertainty, ΔV_{CC} , correspond to the error of the fit result for the V_{CC} parameter (see Appendix A.2). The horizontal error bars in both left and right plots, of the phase, ϕ_{CC} , correspond to the error of the fit result for the phase parameter (see Appendix A.2). It should be noted that the error bars of the phase values are smaller than the markers and are hence not visible in the plots.

The phase scan does not reveal any systematic dependence of the measured voltage, V_{CC} , on the phase, as expected. However, there is a variation of the voltage offset, ΔV_{CC} , with the phase. The origin of this, which seems to be a systematic effect, is not

yet understood and will be addressed in the future to fully characterise the behavior of the beam in the presence of a phase offset in the CC. It should be pointed out that the impact of this effect on the interpreting the CC noise induced emittance growth measurements is limited and thus it will not be a matter of concern for this thesis.

5 | Experimental studies 2018: emittance growth from Crab Cavity noise

In Chapter 3 the theoretical model for the transverse emittance growth caused by amplitude and phase noise in a CC was discussed. On September 5, 2018, a dedicated experiment was conducted in the SPS to benchmark this model against experimental data and confirm the analytical predictions. In particular, the aim was to inject artificial noise in the CC RF system and compare the measured emittance growth rates with the the theoretically computed ones. In this chapter the measurement results from the SPS are presented and discussed. The work published in Ref. [75] is the basis of this chapter.

Section 5.1 describes the machine setup and the beam configuration for the emittance growth measurements. This includes a summary of the preparatory studies conducted in the previous years. In Section 5.2 information on the noise injected in the CC RF system is provided. The measurements of transverse emittance growth are presented in Section 5.3 while the complementary measurements of bunch length and intensity in Section 5.4. The conclusions of the first experimental campaign with CC noise in SPS are drawn in Section 5.6.

5.1 Experimental configuration and procedure

This section gives an overview of the experimental setup and the procedure that was followed. First, it briefly discusses the preparatory studies that were performed during 2012-2017 [76, 77, 78], explaining the choice of the intensity and energy values for which the emittance growth measurements were conducted. Furthermore, it presents in detail the rest of the beam and machine conditions

during the experiment. Last, the experimental procedure is explained.

5.1.1 Preparatory experimental studies

For studying the long-term emittance evolution a special mode of operation was set up in the SPS which is called "coast" (in other machines, it is referred to as storage ring mode) with bunched beams. In this mode, the bunches circulate in the machine at constant energy for long periods, from a few minutes up to several hours, similar to the HL-LHC case.

To make sure that the SPS can be used as a testbed for the emittance growth studies with CCs an extensive preparatory campaign was carried out through 2012-2017 [76, 77, 78]. The primary concern was the emittance growth that was observed in the machine from other sources than injected noise and will be referred to as the natural emittance growth in this thesis. The natural emittance growth needs to be well characterised and be kept sufficiently small in order to distinguish and understand the contribution from the CC noise.

From these studies, it was concluded that the optimal coast setup is at high energies, with low chromaticity and bunches of low intensity as it minimises the natural emittance growth [78]. The highest energy for which the SPS could operate in "coast" was 270 GeV and thus the experiments were performed at this energy. That limitation was introduced due to limited cooling of the magnets to transfer away the heating when operating at high energy and thus at large currents for long periods. Moreover, as the natural emittance growth was found to be a single bunch effect four bunches were used. That choice was made to reduce the statistical uncertainty of the measurements but not to increase the beam intensity.

5.1.2 Machine and beam configuration

During the experiment the Landau octupoles were switched off. Nevertheless, a residual non-linearity was present in the machine mainly due to multipole components in the dipole magnets [79, 80]. The transverse feedback system was also switched off. Unfortunately, no measurements of chromaticity are available from the day of the experiment. However it was ensured that the chromaticity was

5. Experimental studies 2018: emittance growth from Crab Cavity noise

corrected to small positive values.

Last, only one CC, CC2, was used for simplicity and it operated at 1 MV. This value was validated with the HT monitor (post-processing procedure described in Chapter 4). Unfortunately, only one beam based measurement of the CC voltage is available which is displayed in Fig. 5.1. It is clear that the measured value of voltage amplitude, $V_{CC} = 0.99 \pm 0.04$ MV, is in good agreement with the requested one. It should be noted, that due to the beam energy of 270 GeV the crabbing is less visible than the example discussed in Chapter 4 (see Fig. 4.10) for 26 GeV. Therefore, here the part of the signal that is used for the fit is the one for which the normalised sum signal (black dashed line) is above 0.2 (instead of 0.4 that was the condition for the case of 26 GeV)

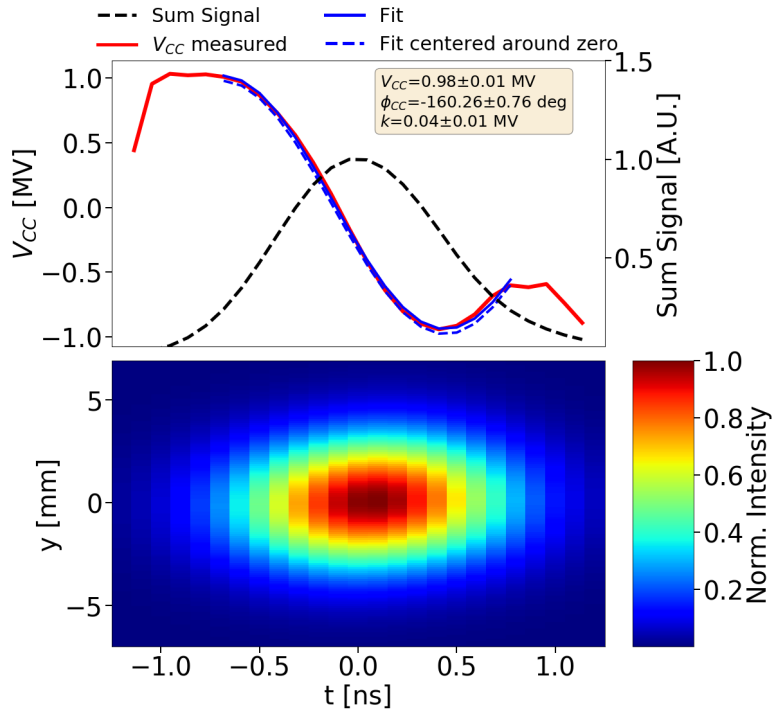


Figure 5.1: Demonstration of the sinusoidal fit on the HT monitor reading in order to obtain the CC parameters as described in Section 4.4. The fit results, are given in the yellow box. The measured voltage amplitude, V_{CC} , was found to be 0.99 MV while its uncertainty, ΔV_{CC} , was measured at 0.04 MV. The measured voltage value agrees well with the requested value of 1 MV.

The main machine and beam parameters used for the emittance growth measurements in 2018 are listed in Table 5.1.

Table 5.1: Main machine and beam parameters for the emittance growth studies with CCs in SPS in 2018.

Parameter	Value
Beam energy, E_b	270 GeV
Revolution frequency, f_{rev}	43.375 kHz
Main RF voltage / frequency, V_{RF} / f_{RF}	3.8 MV / 200.39 MHz
Horizontal / Vertical betatron tune, Q_{x0} / Q_{y0}	26.13 / 26.18
Horizontal / Vertical first order chromaticity, Q'_x / Q'_y	$\sim 1.0 / \sim 1.0$
Synchrotron tune, Q_s	0.0051
CC2 voltage / frequency, V_{CC} / f_{CC}	1 MV / 400.78 MHz
Number of protons per bunch, N_b	3×10^{10} p/b*
Number of bunches	4
Bunch spacing	524 ns
Rms bunch length, $4\sigma_t$	1.8 ns*
Horizontal / Vertical normalised emittance, $\epsilon_x^n / \epsilon_y^n$	$2 \mu\text{m} / 2 \mu\text{m}^*$
Horizontal / Vertical rms tune spread, $\Delta Q_x^{rms} / \Delta Q_y^{rms}$	$2.02 \times 10^{-5} / 2.17 \times 10^{-5}$ †

* The value corresponds to the requested initial value at the start of each coast. The measured evolution of the parameter through the experiment is presented in the Sections 5.3 and 5.4.

† Here the rms betatron tune spread includes only the contribution from the detuning with amplitude present in the SPS machine. More details along with the calculations for the listed values can be found in Appendix C.2.

5.1.3 Experimental procedure

The experiment took place on September 5, 2018, and was given a total time window of about 6 hours (start:~10:30, end:~17:00). In order to characterize the CC noise induced emittance growth, different levels of controlled noise were injected into the low-level RF system and the bunch evolution was recorded for about 20-40 minutes (for each noise setting). The experiment was conducted over three coasts, since a new beam was injected every time the quality of the beam was seen to be degraded e.g. very large beam size. In the following, the different noise settings will be denoted as "Coast N -Setting M ", where N stands for the coast number and M for the different noise levels applied in each coast in chronological order. After the experiment, the measured growth rates would be compared with the theoretically expected values from the model described in Chapter 3.

5.2 Injected RF noise

The noise injected in the CC RF system was a mixture of amplitude and phase noise

5. Experimental studies 2018: emittance growth from Crab Cavity noise

up to 10 kHz, overlapping and primarily exciting the first betatron sideband at ~ 7.8 kHz¹. The phase noise was always dominant. The noise levels were measured with a spectrum analyzer E5052B [81] and are expressed as $10 \log_{10} \mathcal{L}(f)$ [dBc/Hz]. The relation between the measured noise levels and the power spectral densities (PSDs) in Eq. (3.7) and Eq. (3.8) is given by $S_\Delta = 2\mathcal{L}(f)$, with $S_{\Delta A}$ in 1/Hz and $S_{\Delta\phi}$ in rad²/Hz. This relation is extensively discussed in Appendix C and specifically in B.3. Figure 5.2 displays an example measurement of amplitude (left) and phase (right) noise acquired during the experiment.

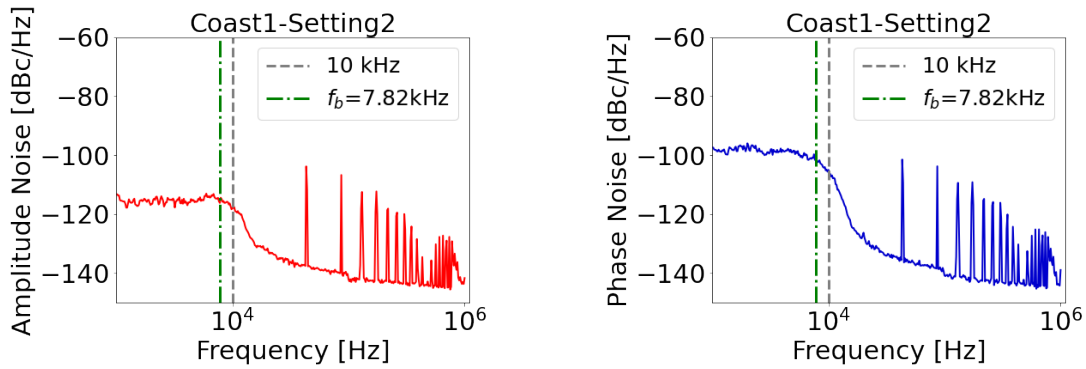


Figure 5.2: Example amplitude (left) and phase (right) noise spectra measured with a spectrum analyzer E5052B [81] during the emittance growth studies with CCs in SPS. The noise extends up to 10 kHz (grey dashed line) overlapping the first betatron sideband at ~ 8 kHz (green dashed line). The spikes at high frequencies correspond to the harmonics of the revolution frequency and are a result of the bunch crossing.

PSD values of interest

As already discussed in Chapter 3 the noise induced emittance growth depends on the noise power at the betatron and synchrobetatron sidebands for the phase and amplitude noise respectively (see Eq. (3.8) and Eq. (3.7)). Therefore, the noise power values of interest for this thesis are the ones at the first betatron $f_b = 0.18 \times f_{rev} = 7.82$ kHz and at the synchrobetatron sidebands at $f_b \pm Q_s \times f_{rev} = f_b \pm \sim 220$ kHz.

However, it can be clearly seen from Fig. 5.2 that the measured noise spectra are noisy: random changes in amplitude are observed from point to point within the signal. To this end, the PSD value at the first betatron sideband, f_b , is determined

¹The frequency in Hz of the first betatron sidebands (vertical plane) is computed according to Eq. (3.6) for $k = 0$: $\pm \bar{q}_y \times f_{rev} = 0.18 \times 43.38$ kHz ≈ 7.8 kHz.

as the average of the PSD values over a frequency range of ± 500 Hz around it, while its uncertainty is considered to be the standard deviation over that range. In the following, it is assumed for simplicity that the PSD at the synchrobetatron sidebands equals the PSD at the first betatron sideband as they lie very close to each other. At this point, it should be mentioned that the validity of these assumptions was tested with numerical simulations which used the measured spectra (Chapter 6).

The emittance growth measurements were performed with seven different noise levels. The values of the phase and amplitude noise for each setting are listed in Table 5.2.

Effective phase noise

In order to make a meaningful comparison between the different levels of noise, the concept of effective phase noise is introduced: this is the phase noise level that would lead to the same emittance growth as that from both phase and amplitude noise according to the theoretical model (Chapter 3).

For the calculation of the effective phase noise the averaged bunch length for each case is used (bunch length measurements at Section 5.4). The uncertainty on the effective phase noise is computed following the standard procedure of the propagation of the uncertainty (Appendix A.3). [Do I need to show all the calculations?](#) The calculated effective phase noise values for the experimental conditions are also listed in Table 5.2. The values shown correspond to the results using the parameters of the first bunch. However, the difference between the values for the other bunches is very small and is also within the displayed uncertainties. The noise levels mentioned in the following analysis of the experimental data correspond to the calculated effective phase noise.

5.3 Emittance growth measurements

This section presents the transverse emittance growth measurements with CC RF noise. It discusses first the measurement of the beam emittance with the SPS wire scanners (WS) and then it provides an overview of the emittance growth measurements for the four bunches over all the different noise settings.

5. Experimental studies 2018: emittance growth from Crab Cavity noise

Table 5.2: Phase and amplitude noise levels injected in the CC RF system for the emittance growth studies of 2018. The listed values correspond to the average PSD values over a frequency range of ± 500 Hz around the first betatron sideband, f_b . The calculated effective phase noise for the parameters of the first bunch are also listed.

	$10 \log_{10} \mathcal{L}(f)$ [dBc/Hz]		
	Phase noise	Amplitude noise	Effective phase noise
Coast1-Setting1	-122.6 ± 0.6	-128.1 ± 0.6	-121.8 ± 0.5
Coast1-Setting2	-101.4 ± 0.8	-115.2 ± 0.6	-101.3 ± 0.8
Coast2-Setting1	-115.0 ± 0.8	-124.1 ± 0.5	-114.6 ± 0.7
Coast2-Setting2	-111.4 ± 0.6	-115.7 ± 0.4	-110.2 ± 0.5
Coast3-Setting1	-110.9 ± 0.9	-116.9 ± 0.4	-110.1 ± 0.8
Coast3-Setting2	-106.4 ± 0.3	-112.9 ± 0.6	-105.8 ± 0.3
Coast3-Setting3	-101.4 ± 0.7	-106.9 ± 0.5	-100.6 ± 0.6

5.3.1 SPS Wire Scanners

The SPS is equipped with wire scanners (WS) to measure the transverse beam emittance. The SPS WS system is described in detail in Ref. [82, 83]. For the SPS tests, the emittance was measured with WS both for the horizontal and vertical plane (BWS.51995.H and BWS.41677.V respectively).

The working principle is shown in Fig. 5.3. A thin wire rapidly moves across the proton beam and a shower of secondary particles is generated. The signal from the secondary particles is then detected by a system of scintillator and photomultiplier (PM) detectors outside of the beam pipe. By measuring the PM current as a function of wire position over multiple turns the transverse beam profile is reconstructed. An example of a vertical profile is shown in Fig. 5.4.

Fitting of transverse profiles

Assuming gaussian beams and for $u = x, y$ being the index that respectively corresponds to the horizontal and vertical plane, the rms beam size, σ_u , is obtained following the standard procedure of least squares fitting (see Appendix A.2). In particular, the measured beam profiles from each scan are fitted with the following four-parameter (A, k, μ, σ_u) gaussian function:

$$f(x) = k + Ae^{-\frac{(x-\mu)^2}{2\sigma_u^2}}, \quad (5.1)$$

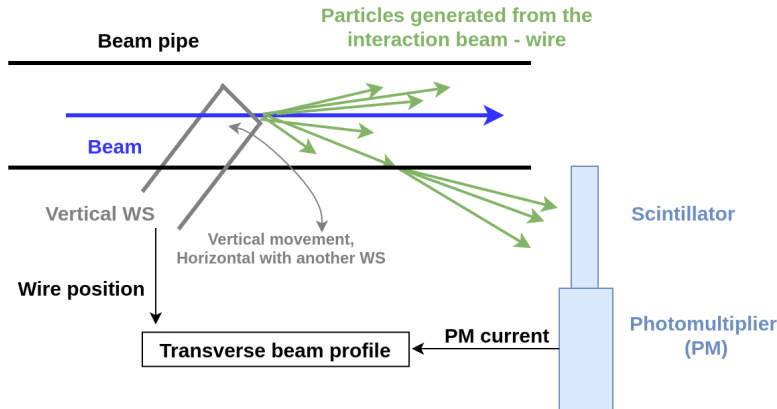


Figure 5.3: Sketch of the SPS rotational wire scanners [83]. The wire moves across the proton beam generating secondary particles which are then detected by a scintillator and a photomultiplier. From the measured photomultiplier current the beam profile is reconstructed.

where k is the signal offset of the PM, A is the signal amplitude, μ is the mean of the gaussian distribution and σ_u its standard deviation. The uncertainty of the measured rms beam size, $\Delta\sigma_u$, is defined as the error of the fit of the σ_u parameter (see Appendix A.2).

An example of the beam profile measured from the SPS WS at a specific time is shown in Fig. 5.4 (light blue dots) along with the gaussian fit (orange line).

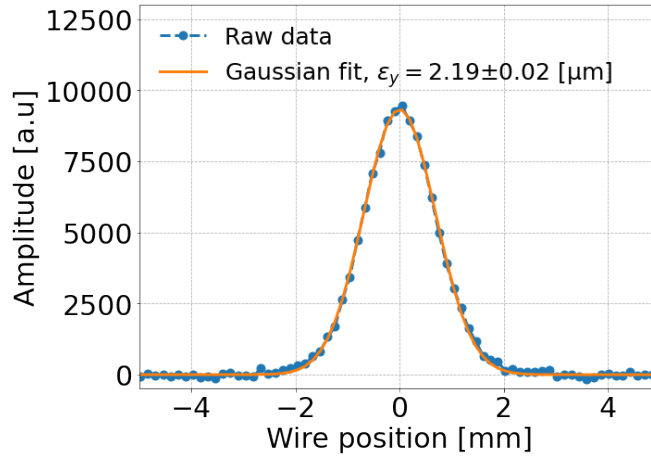


Figure 5.4: Vertical beam profile obtained from the BWS.41677.V instrument. The measured data points (light blue) are fitted with a four parameter gaussian (orange) to obtain the beam size. The calculated emittance and its uncertainty are also shown.

Computing the normalised beam emittance

The formula for computing the normalised beam emittance from the beam size, σ_u is given by:

$$\epsilon_u = \frac{\sigma_u^2}{\beta_{u,WS}} \beta_0 \gamma_0, \quad (5.2)$$

where σ_u is the rms beam size, $\beta_{u,WS}$ the beta function at the WS location and β_0, γ_0 the relativistic parameters. Note that $u = x, y$ is the index that respectively corresponds to the horizontal and vertical plane.

Assuming that the relativistic parameters are free of error, the uncertainty of the computed emittance, $\Delta\epsilon_u$, depends on the uncertainty of the measured beam size, $\Delta\sigma_u$ and of the beta function at the location of the WS, $\Delta\beta_{u,WS}$, as follows:

$$\Delta\epsilon_u = \sqrt{\left(\frac{\partial\epsilon_u}{\partial\sigma_u}\right)^2 \Delta\sigma_u^2 + \left(\frac{\partial\epsilon_u}{\partial\beta_{u,WS}}\right)^2 \Delta\beta_{u,WS}^2} = \epsilon_u \sqrt{\left(\frac{2\Delta\sigma_u}{\sigma_u}\right)^2 + \left(\frac{\Delta\beta_{u,WS}}{\beta_{u,WS}}\right)^2}. \quad (5.3)$$

For the computation of the emittance values from the CC experiment of 2018, the following points were considered. First, in the 2018 SPS operational configuration, the dispersion was small at the WS location and thus its contribution to the beam size was considered to be negligible ². Moreover, for the studies at 270 GeV beam energy, $\beta_0 \gamma_0$ equals 287.8 and the beta functions were 81.5 m and 62.96 m at the locations of the horizontal and vertical WS respectively. Last, the uncertainty on the beta functions at the location of the WS, $\Delta\beta_{u,WS}$, is 5% in both planes, which represents the rms beta-beating in the SPS [84].

Further considerations

It is worth noting here that during each measurement with the WS the beam profile is actually acquired twice as the wire crosses the beam in the forward direction (IN scan) and then in the reverse direction (OUT scan). For the 2018 measurements the emittance values obtained from IN and OUT scans, $\epsilon_{\text{IN}} \pm \Delta\epsilon_{\text{IN}}$ and $\epsilon_{\text{OUT}} \pm \Delta\epsilon_{\text{OUT}}$,

²The dispersion at BWS.51995.H location in 2018 was $D_x = -15$ mm. At 270 GeV, the energy spread, δ , is of the order of 10^{-4} . Thus, from Eq. (2.37) the horizontal normalised emittance from the dispersion is expected at the order of $10^{-6} \mu\text{m}$. Comparing to the observed beam size during the CC tests of a few microns the dispersion is negligible. **The measured D_x, D_y were found to be very small and thus their contribution is also considered negligible. The plan is to perform some measurements in 2022 to get a feeling of their values at the location of the wire scanners**

were found to be very similar. In the analysis of the 2018 measurements, the average emittance from the two scans, $\epsilon_{\text{avg}} = \langle \epsilon_{\text{IN}}, \epsilon_{\text{OUT}} \rangle$, is used. The uncertainty in the average, $\Delta\epsilon_{\text{avg},1}$, is given by [85]:

$$\Delta\epsilon_{\text{avg},1} = \frac{|\epsilon_{\text{IN}} - \epsilon_{\text{OUT}}|}{2\sqrt{2}}. \quad (5.4)$$

The propagated uncertainty from the measurement errors, $\Delta\epsilon_{\text{IN}}$ and $\Delta\epsilon_{\text{OUT}}$, is given by:

$$\Delta\epsilon_{\text{avg},2} = \frac{1}{2} \sqrt{\Delta\epsilon_{\text{IN}}^2 + \Delta\epsilon_{\text{OUT}}^2}. \quad (5.5)$$

Assuming that $\Delta\epsilon_{\text{avg},1}$ and $\Delta\epsilon_{\text{avg},2}$ are independent, the combined uncertainty in the average, $\Delta\epsilon_{\text{avg}}$, is given by:

$$\Delta\epsilon_{\text{avg}} = \sqrt{\Delta\epsilon_{\text{avg},1}^2 + \Delta\epsilon_{\text{avg},2}^2}. \quad (5.6)$$

Finally, some emittance increase is expected during each wire scan, due to multiple Coulomb scattering. This effect has been extensively studied in Ref. [86]. For the rotational SPS WS and the energy of 270 GeV, at which the CC experiments were performed the expected emittance growth from the WS is expected to be between 0.0-0.2% per scan in both transverse planes. However, a conservative number of scans were carried out, ~ 20 scans per bunch and per plane during ~ 1 hour, in order to minimise the contribution from this effect.

5.3.2 Experimental results

In this section, an overview of the emittance growth measurements is presented. Figure 5.5 displays the bunch by bunch transverse emittance evolution through the total duration of the experiment. The three different coasts are distinguished in this plot with the blue dashed vertical lines. The values of the effective phase noise are also displayed (see Table 5.2), while the moments when the noise level changed are shown with the grey vertical lines. The four different colors (blue, orange, red, green) correspond to the four different bunches. For the bunches the notation "bunch N " will be used, where $N = \{1, 2, 3, 4\}$ according to their position in the bunch train. The errorbars of the emittance values correspond to the uncertainty computed using

5. Experimental studies 2018: emittance growth from Crab Cavity noise

Eq. 5.6. However, as they are very small compared to the scale of the plots they are barely visible. Last, the emittance growth rates, $d\epsilon_u/dt$, for each setting and for each bunch are displayed at the bottom of each plot along with their uncertainties. The growth rates are obtained following the standard procedure of weighted least squares fitting (see Appendix A.2). In particular, the measured beam profiles from each scan are fitted with the following polynomial:

$$p(x) = c_0 + d\epsilon_u/dt \times t \quad (5.7)$$

where t is the time in seconds, $d\epsilon_u/dt$ the growth rate in meters per second and c_0 the constant offset in meters. The uncertainties of the growth rates correspond to the error of the fit (see Appendix A.2).

First observations and comments

Figure 5.5 demonstrates a clear emittance growth in the vertical plane which is expected due to the vertical CC. However, the CC noise is observed to induce growth also in the horizontal emittance as a result of residual coupling in the machine. Thus, the total emittance growth given by $d\epsilon_x/dt + d\epsilon_y/dt$ should be considered in the following. That was confirmed by PyHEADTAIL simulations [87] in the presence of CC RF noise and transverse coupling.

Furthermore, both the phase and amplitude noise levels for Coast1-Setting1 were found to be below the noise floor of the instrument. Therefore, the transverse emittance growth observed during that case is a result of other sources (natural emittance growth, see Section 5.1.1) and will be considered as the background growth rate in the analysis below. [Is this approach ok? instead of using 0.45 and 0.55 um/h for the y and x planes respectively.](#)

Summary plot

Figure 5.6 provides a clearer view of the measurements presented in Fig. 5.5. It displays the measured emittance growth rates for each one of the four bunches for the different levels of injected noise. The horizontal error bars correspond to the uncertainty of the effective phase noise (see Section 5.2) while the vertical error

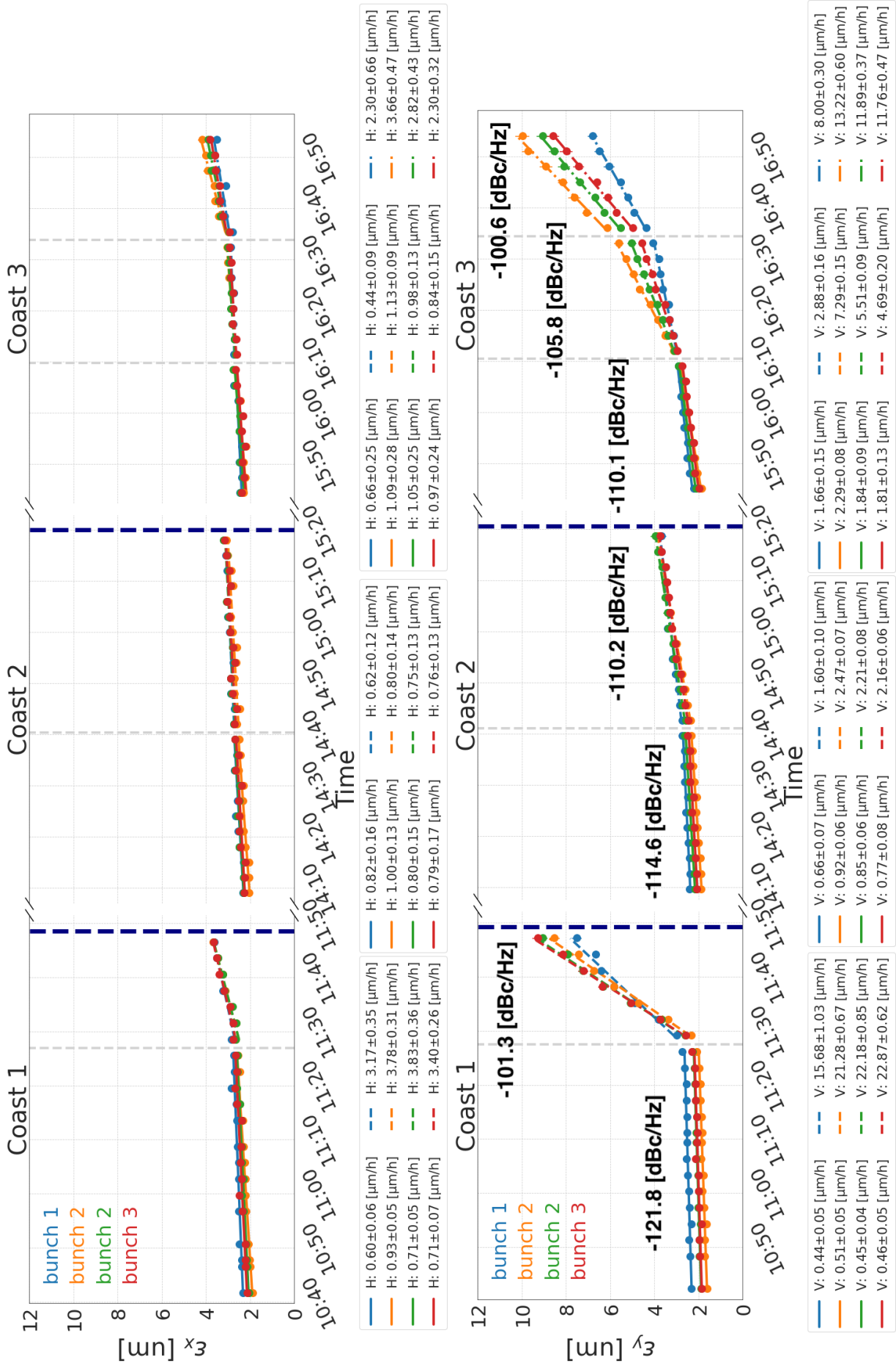


Figure 5.5: Bunch by bunch horizontal (top) and vertical (bottom) emittance evolution during the experiment on September, 15, 2018. The four different colors indicate the different bunches. The different applied noise levels are also shown while the moments when the noise level changed are indicated with the grey vertical dashed lines. The emittance growth rates along with their uncertainties for the seven different noise settings are displayed at the bottom of the plots.

bars correspond to the uncertainty of the total transverse emittance growth calculated from the uncertainties of the horizontal and vertical growth rates following the standard procedure of the propagation of the uncertainty (Appendix A.3).

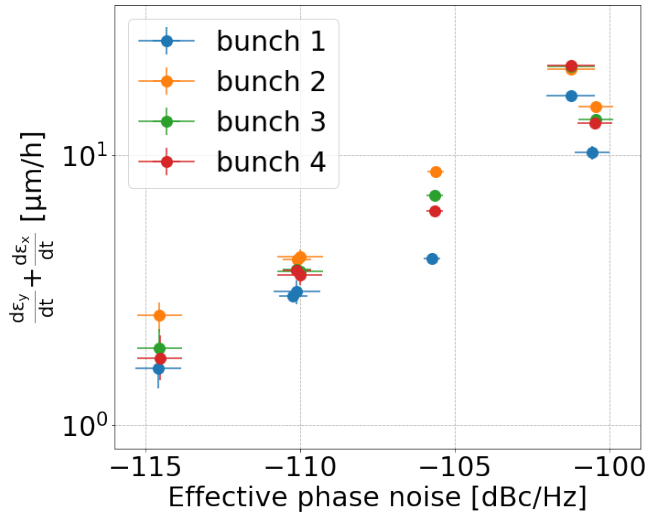


Figure 5.6: Summary plot of the emittance growth study with CC noise in 2018. The transverse emittance growth rate, for the four bunches, is shown as a function of the different levels of applied noise.

From the plot it becomes clear that the measured emittance growth was different for the four different bunches. Furthermore, the first bunch (blue) had systematically the smallest growth rate.

An attempt to understand these observations will be presented in the following section, based on a possible correlation between the transverse emittance growth and the beam evolution in the longitudinal plane.

5.4 Bunch length and intensity measurements

The measurements of the bunch length and intensity that took place in parallel with the emittance growth measurements are presented in this section. The goal is to get a more complete insight of the experimental conditions and possibly explain the different emittance growth rates observed for the four bunches which was discussed in the previous section. Initially, a short introduction on the instruments used for the measurements is provided. After that, the evolution of the longitudinal plane and of the intensity is analysed and discussed.

5.4.1 ABWLM and Wall Current Monitor

The bunch length was measured with two different instruments the ABWLM³ [88] and the Wall Current Monitor [89]. Both ABWLM and Wall Current Monitor acquire the longitudinal bunch profiles, while ABWLM is much faster than the Wall Current Monitor. In the ABWLM case the bunch length is obtained by performing a gaussian fit on the acquired profiles. Only the calculated bunch length values are available but not the profiles themselves. For the case of the Wall Current Monitor the bunch length is estimated by computing the full width half maximum of the profiles and then using it to estimate the standard deviation of a gaussian distribution. The longitudinal profiles and the calculated bunch lengths are available for each acquisition. Furthermore, the Wall Current Monitor provides additional information on the relative bunch position with respect to the center of the RF bucket, which will also be used in the following analysis. No further details on the operation of these instruments are discussed here as the offline analysis was not performed by the author.

[How is the intensity calculated?](#)

5.4.2 Bunch length measurements

The bunch length measurements that took place during the CC noise induced emittance growth studies are shown in the bottom plot in Fig. 5.7. The small markers correspond to the data acquired with the ABWLM while the bigger markers correspond to the data acquired with the Wall Current Monitor. The two upper plots contain the transverse emittance growth as discussed in Section 5.3.2. This is for easier comparison of the beam evolution in the transverse and in the longitudinal plane. The color code corresponds to the four different bunches.

Four main observations can be made. First, the plot demonstrates a very good agreement between the ABWLM and the Wall Current monitor. Second, an approximately bunch length increase of ~9%/h is observed for bunch 1 (blue) in all the three coasts. This rate, which is computed from the ABWLM data, is similar

³(A for RF, B for Beam, W for Wideband, L for Longitudinal, M for Measurement)

5. Experimental studies 2018: emittance growth from Crab Cavity noise

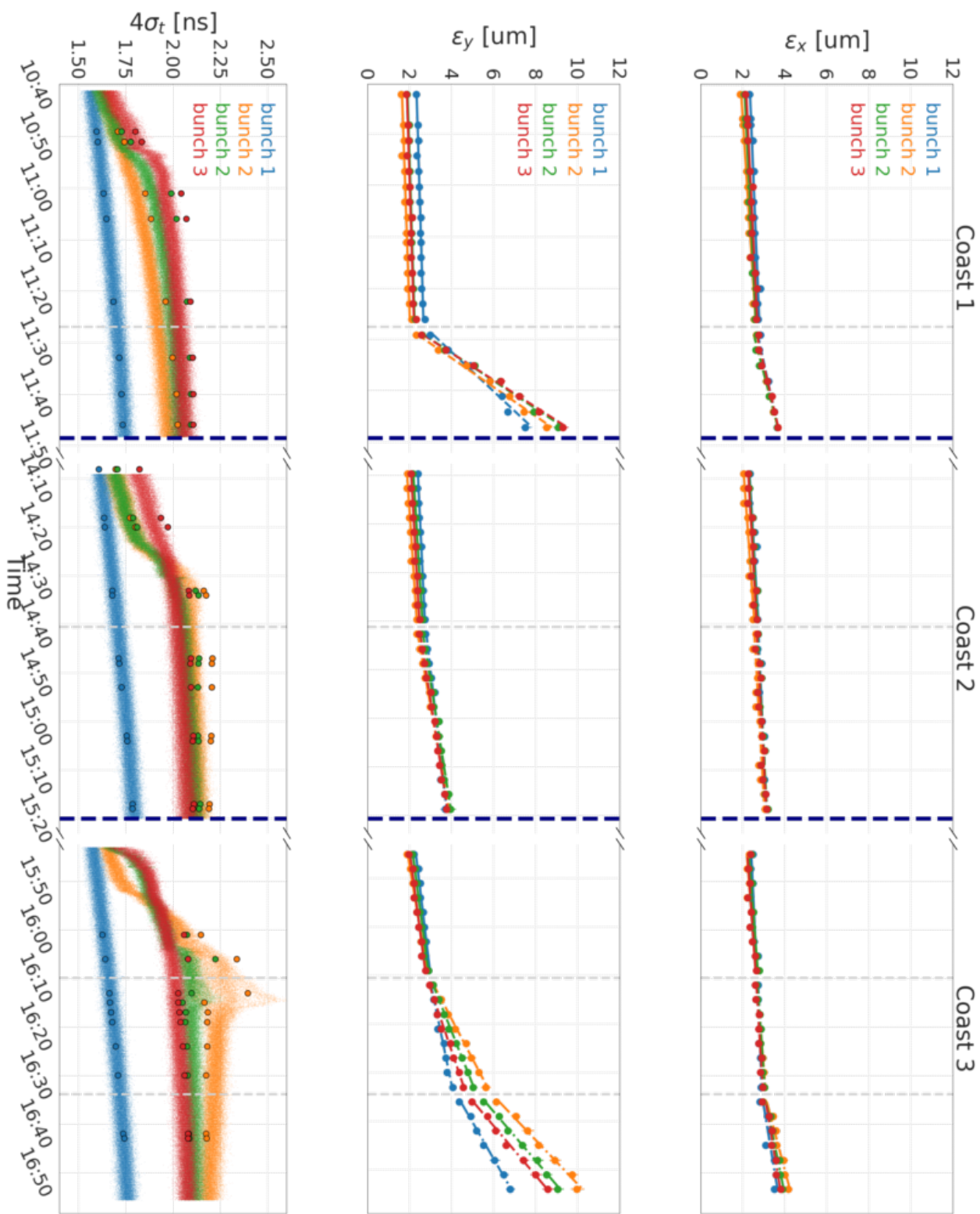


Figure 5.7: Evolution of the beam in transverse and longitudinal planes during the CC noise induced emittance growth experiment. Top: Horizontal emittance growth measured with the SPS WS. Middle: Vertical emittance growth measured with the SPS WS. Bottom: Bunch length evolution measured with the ABWLM (small markers) and the Wall Current Monitor (bigger markers).

to the blow-up observed in the SPS for similar machine conditions [77]. Third, the bunch length increase for the last three bunches (2, 3, and 4) is larger than the increase for bunch 1. However, bunches 2, 3, and 4 seem to be longitudinally unstable as sudden jumps appear in their bunch length evolution and this could explain the faster bunch length increase. Last, no correlation is observed between the bunch length evolution and the change of noise level. In order to validate that bunches 2, 3, and 4 are unstable, the longitudinal profiles acquired with the Wall Current Monitor are studied in the next paragraph.

5.4.3 Longitudinal profile measurements

Two example longitudinal profile acquisitions from the Wall Current Monitor are discussed here as they can provide further insight on the sudden jumps observed in the bunch length values for bunches 2, 3, and 4. The selected acquisitions correspond to the moments where the sudden jumps are performed in the second and third coast and are shown in Fig 5.8. The relative bunch position with respect to the center of the RF bucket of each bunch for an acquisition period of 7 ms is also illustrated in the bottom plots of Fig. 5.8 for completeness.

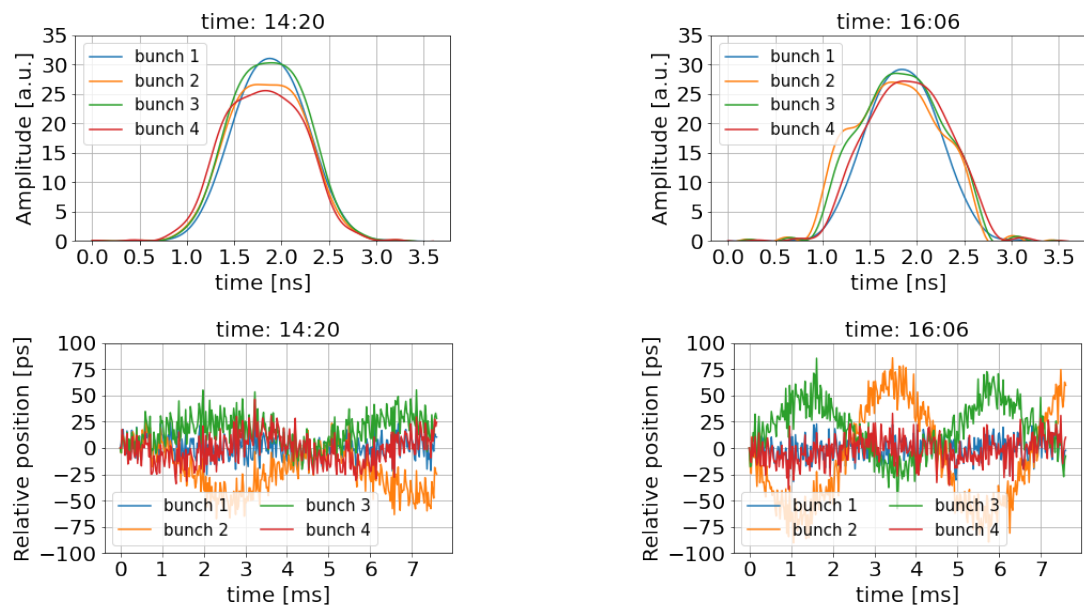


Figure 5.8: Longitudinal profiles (top) and relative bunch position with respect to the center of the RF bucket (bottom) acquired with the Wall Current Monitor. The acquisitions correspond to the times when the sudden jumps in the bunch length evolution are observed (see Fig. 5.7).

5. Experimental studies 2018: emittance growth from Crab Cavity noise

From Fig. 5.8, it becomes clear that bunches 2,3, and 4 (orange, green, and red) are longitudinally unstable. This is believed to be due to the fact that the phase loop was sampling only the first bunch because of the large bunch spacing of 525 ns [90]. For this reason, the following analysis is focused only on bunch 1, which was not affected by the instability. However, in the next paragraph the intensity measurements for all the four bunches are exceptionally illustrated.

5.4.4 Intensity measurements

The bunch by bunch intensity measurements that were performed along the experiment with artificial CC noise are displayed in Fig. 5.9. In particular the intensity values normalised with the intial value are shown for each bunch. The four different bunches are indicated with the four different colors. The acquisitions from both the ABWLM and the Wall Current Monitor are illustrated with the small and bigger markers respectively.

The following observations can be made. First, there is very good agreement between the measruments from the ABLWM and the Wall Current Monitor. Second, losses of $\sim 2\text{-}4\%/\text{h}$, computed from the ABLWM acquisitions, are observed for bunch 1 (blue) in all the three coasts. This rate is even smaller than observed in the SPS in coast studies without external noise ($\sim 10\%/\text{h}$) [77]. Last, more significant losses are observed for the longitudinally unstable bunches (bunch 2,3, and 4). However, this is not of concern as the last three bunches will not be included in the following analysis as discussed in the previous paragraph (5.4.3).

5.5 Comparison of measured transverse emittance growth with the theoretical predictions

This section focuses on the main objective of the experiment which was the comparison of the measured transverse emittance growth with the expected values as computed from the theoretical model discussed in Chapter 3. As already discussed (Section 5.4.3), the comparison considers only bunch 1 as the other three

5.5. Comparison of measured transverse emittance growth with the theoretical predictions

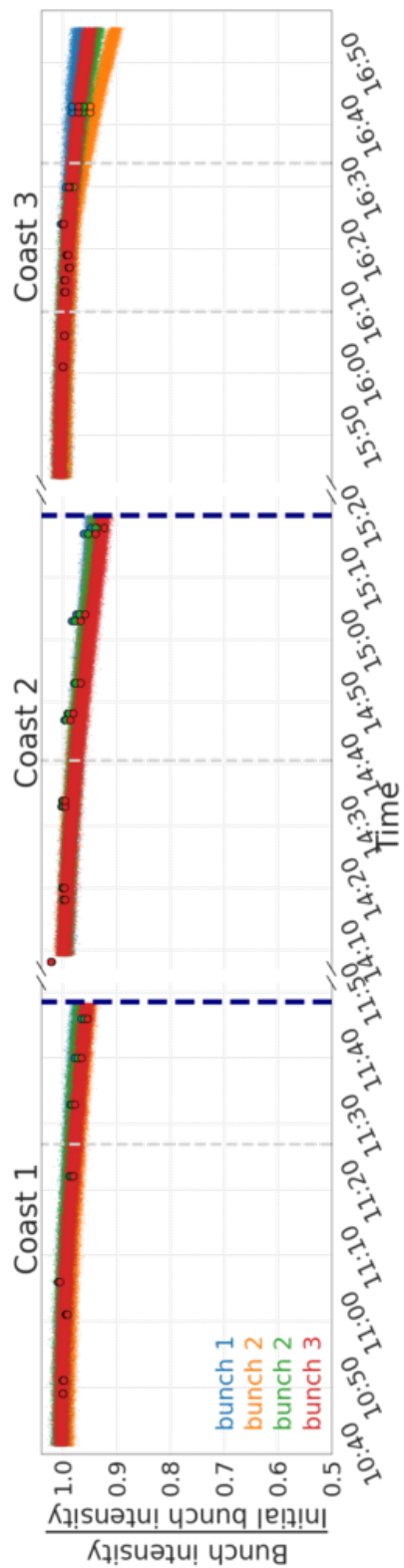


Figure 5.9: Intensity evolution as measured with ABLWM (smaller markers) and with the Wall Current Monitor (bigger markers) during the experiment with CC noise in 2018.

5. Experimental studies 2018: emittance growth from Crab Cavity noise

bunches were found to be longitudinally unstable.

Figure 5.10 compares the measured (blue) and the theoretically calculated (black) emittance growth rates of bunch 1 for the different noise levels. For the comparison, the background growth rate from other sources (measured during Coast1-Setting1, as discussed in Section 5.3) is subtracted from the measured values. In particular the background growth was measured $0.6 \mu\text{m}/\text{h}$ and $0.44 \mu\text{m}/\text{h}$ for the horizontal and vertical plane respectively. One should keep in mind that background subtraction has practically no impact for high noise levels. Instead, it is significant for small noise levels.

The expected emittance growth due to CC noise was estimated for all noise settings using Eq. (3.8). The growth was computed for the beam energy of 270 GeV, considering the vertical beta function at the location of the CC2 of 73.82 m and the revolution frequency of SPS which is 43.37 kHz. For each setting, the measured noise PSDs (i.e. effective phase noise) and the average bunch length over each observation window were used in the calculation. These values are listed in the first two columns of Table 5.3.

The horizontal error bars, for both measured and calculated growths, correspond to the uncertainty of the effective phase noise values (see Table 5.2). The vertical error bars for the measured growth are defined as the error of the linear fit on the emittance values (see Section 5.3). The vertical error bars on the theoretically calculated rates are computed following the standard procedure of propagation of the uncertainty. It should be mentioned here that only the uncertainties on the effective phase noise ($\sim 13\%$ on average for bunch 1) are included in the error propagation. The beam energy and the revolution frequency are assumed to be free of error, while the uncertainties of the rest of the parameters: bunch length, CC voltage and beta function ($\sim 2\%$, 0.01% , and 5% respectively) are not included as they are much smaller than those of the noise.

From Fig. 5.10 it becomes evident that the theory systematically overestimates the measured growth rates. The averaged discrepancy over all noise levels is a factor of 4: numerical values are given in Table 5.3. The measurements seem to go in the good direction but actually they show that there is a significant uncertainty on the

5.5. Comparison of measured transverse emittance growth with the theoretical predictions

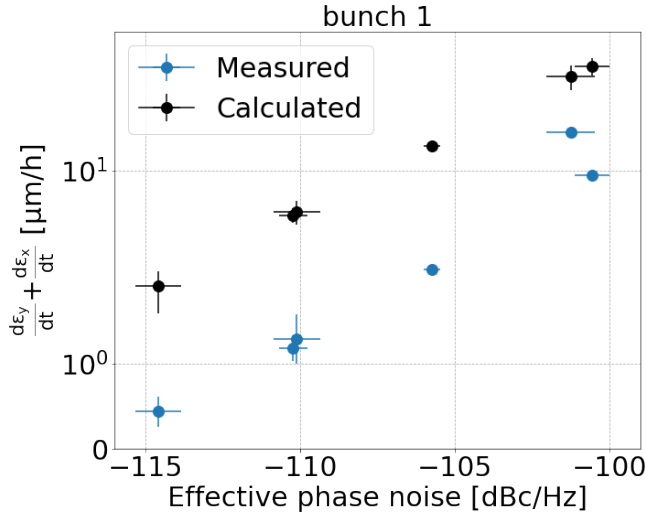


Figure 5.10: Summary plot of the emittance growth study with CC noise in 2018 focused on bunch 1 only. The measured emittance growth rate (blue) and the expected growths from the theoretical model (black) are shown as a function of the different levels of applied noise.

predictions of the theoretical model. The accuracy of the model is essential for defining the specifications for the design of the HL-LHC CC LLRF. Therefore, understanding the reason behind the observed discrepancy with the measurements which would also allow to decide if the reduction of the factor 4 can be propagated for the HL-LHC predictions is fundamental. The studies performed to explain the discrepancy will be described in the following chapters.

Table 5.3: Comparison between the measured and the calculated transverse emittance growth rates for bunch 1 for the different noise levels, and average bunch length for each case.

$10 \log_{10} \mathcal{L}(f)$ [dBc/Hz]	$\langle \sigma_\phi \rangle$ [rad]	Growth rate [$\mu\text{m}/\text{h}$]	
		Measured	Calculated
-114.6	1.05	0.44	1.9
-110.2	1.10	1.18	5.10
-110.1	1.03	1.28	5.38
-105.8	1.06	2.28	14.50
-101.3	1.08	17.81	40.55
-100.6	1.09	47.42	9.26

5.6 Conclusions and outlook

The objective of the first experimental campaign with CC noise in the SPS was to benchmark the available theoretical model which predicts the noise induced transverse emittance growth against measurements. For this reason, a dedicated experiment took place in the SPS in September of 2018, with different levels of artificial noise injected in the CC RF system. Four bunches circulated in the machine for long periods of time and their emittance evolution was recorded to be compared with the theoretical predictions.

The experiment demonstrated that the transverse emittance of all the four bunches increased for stronger noise. However, during the analysis it was found that only the first bunch of the train was stable in the longitudinal plane. For this reason, only the data from the first bunch were used for the comparison with the theoretically calculated emittance growth rates. The comparison showed that the theoretically overestimates the measurements by a significant factor of 4. The reason behind this discrepancy needs to be understood as the predictions of the theoretical model will be used to define limits and acceptable noise levels for the HL-LHC CCs. Therefore, the next chapters focus on explaining the observed discrepancy.

6 | Investigation of the discrepancy

6.1 Benchmarking with different simulation software

Benchmarking of theory with pyheadtail (one turn map) and Sixtracklib (element by element tracking).

6.1.1 PyHEADTAIL

- real CC element - local vs global cc scheme - How emittance is computed. No dispersive contribution. studies vertical plane.
- It was verified in Sixtracklib simulations that the result from this simplified implementation is equivalent to the simulation with the true CC kick including phase noise.
- Need to say why in the simulations we have excitation of only the first betatron sideband.

6.1.2 Sixtracklib

Remember that in chapter 6 it was demonstrated that there is no visible difference on the cc rf noise induced emittance growth if the noise kicks are modeled as kicks on the momentum or the real rf multiple + used in a global or local scheme.

pyheadtail vs sixtracklib:

6.2 Sensitivity to the non-linearities of the main SPS dipoles

Simulation studies with sixtracklib

6.3 Simulations using the measured noise spectrum

Sixtracklib PyHEADTAIL and the exact machine parameters

6.4 Sensitivity studies

1. Sensitivity to how noisy is the noise spectrum
2. On the CC voltage
3. On the different bunch lengths.

6.5 b3b5b7 multiple errors

Contribution of the non-linearities with sixtracklib.

All these factors were excluded as possible sources of the discrepancy.

7 | Simulation studies: Suppression mechanism from the beam transverse impedance

During the dedicated experiment that took place in the SPS in 2018 with the CCs, the measured emittance growth was found to be a factor four (on average) lower than expected from the theory (see Section 5.5). The reason for this discrepancy remained unresolved for some time, as detailed follow-up studies (see Chapter 6) investigated and excluded a number of possible explanations for the discrepancy. It was recently found, that the beam transverse impedance, which is not included in the theory [63] used for the comparison with the measurements may impact the noise-induced emittance growth and explain the experimental observations. Here, the damping mechanism from the beam transverse impedance is investigated as observed in detailed PyHEADTAIL simulations.

The structure of this chapter is as follows:

7.1 SPS transverse impedance model

The PyHEADTAIL studies presented in this chapter are performed including the detailed transverse impedance model of the SPS machine [91]. This model has been developed through a combination of theoretical computations, electromagnetic simulations and was benchmarked with beam-based measurements [56, 92, 93, 94]. It includes the contributions from all the individual elements in the SPS lattice i.e. the resistive wall, the indirect space charge, the kickers, the RF cavities (200 MHz and 800 MHz), the step transitions and the

7. Simulation studies: Suppression mechanism from the beam transverse impedance

horizontal and vertical beam position monitors [94]. As discussed in Section 2.5.1, the model needs to represent the global impedance of the full machine. Thus, the total impedance is obtained by summing up the impedance of each element weighted with the beta function at its location and by dividing the sum by the average beta function of the SPS. For the Q26 optics the average horizontal and vertical beta functions are 42.09 m and 42.01 m respectively. Figure 7.1 shows the complete transverse impedance model of the SPS machine with the disentangled dipolar (blue) and quadrupolar (orange) terms to be plotted separately.

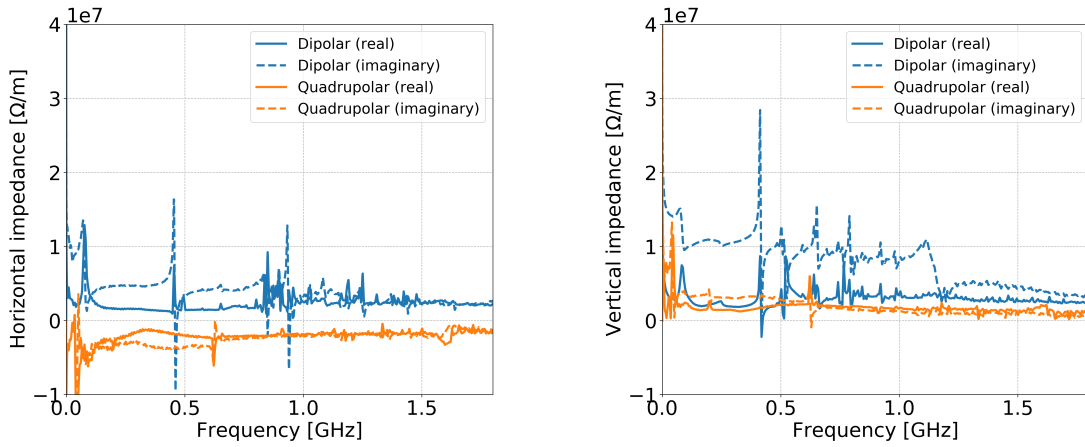


Figure 7.1: Horizontal (left) and vertical (right) impedance model of the SPS. The model is available in the public gitlab repository of Ref. [91].

The contributions from the wall, the kickers and the step transitions are visible at the low frequencies (up to ~ 0.4 GHz). The impedance of the RF cavities and the beam position monitors (BPMs) corresponds results to the peaks observed between ~ 0.4 -1 GHz.

Wake functions

As already discussed in Section 2.5.1, in order to include the impedance effects in PyHEADTAIL simulations the real-value wakefields in time domain are used. The wakefield kicks are computed as a convolution of the wake function with the moments of each particle. The total transverse dipolar (blue) and quadrupolar (orange) wake functions for both planes of the SPS can be found in the gitlab repository of Ref. [91] and they are plotted in Fig 7.2.

The constant terms, in both transverse planes, equal zero in the SPS impedance model. The reason behind this, is that firstly the constant term is usually coming

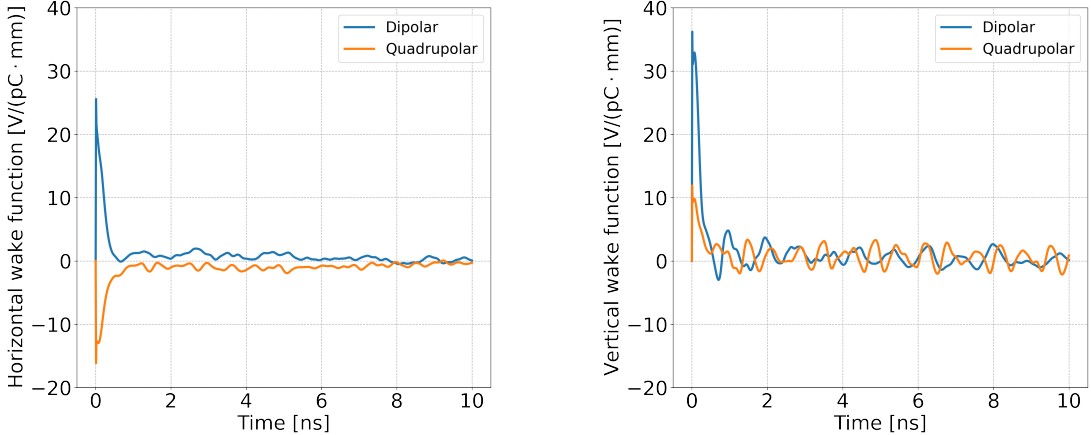


Figure 7.2: Horizontal (left) and vertical (right) wakefunctions of the SPS. The wake functions are available in the public gitlab repository of Ref. [91]. For comparison the bunch length in the SPS CC experiments is ~ 1.85 ns ($4\sigma_t$).

from asymmetries in the various structures which are not significant, and secondly the constant term does not lead to instabilities or tune shift, so usually is not of big concern.

It should be highlighted that the impedance model is not obtained from a simple Fast Fourier Transform algorithm on the wakefunctions but rather with more complex procedures described in the references provided above. Last the impedance model is used as an input in the Sacherer formula (Eq. (2.57)) for analytical estimations while the wake functions are used as an input in simulation codes such as PyHEADTAIL.

7.1.1 Testing the implementation in PyHEADTAIL

As discussed in Section 2.3.1 the imaginary part of the impedance leads to a coherent tune shift which depends on the bunch intensity. One of the most common ways to test the correct implementation of the impedance model in a tracking simulation code is to benchmark the simulated intensity-dependent coherent tune shift with the theoretically predicted behavior (using Eqs. (2.57) and (2.62)).

Typically, in tracking simulations, the coherent tune is obtained by applying a frequency analysis technique to the oscillations of the centroid of the particle distribution (the center of mass of the bunch). Here, the analysis is limited to the

7. Simulation studies: Suppression mechanism from the beam transverse impedance

coherent mode $l = 0$ as it can be obtained using a simple Fast Fourier Transform (FFT) algorithm [95]. Higher modes (in absolute value, i.e. $l = \pm 1, \pm 2$ etc) can be obtained with more complex algorithms such as the ones provided from the SUSSIX code [96]¹. Nevertheless, the study of mode $l = 0$ is sufficient for the purpose of the studies presented here. For simplicity in the following the term "coherent tune" will refer to the coherent tune of mode $l = 0$.

Simulations setup

The parameters used for setting up the linear transfer map, the longitudinal tracking, and the beam initialisation are shown in Table 7.1 and are the ones used in the SPS CC experiment of 2018. The ring is consisted of one segment, with one interaction point at which the beam interacts with the wakefields. At that location, the horizontal and vertical beta functions equal the corresponding average beta functions over the SPS machine (see Section 2.5.1). The latest transverse wakefield model (as of February 2019 in Ref. [91]) of the SPS was used.

The bunch population of the different intensity values, was represented by 5×10^5 macroparticles and the number of slices of the longitudinal distribution was 500.

Table 7.1: PyHEADTAIL simulation parameters used to study impedance induced effects for the SPS.

Parameter	Value
Beam energy, E_b	270 GeV
Machine circumference, C_0	6911.5623 kHz
Horizontal / Vertical betatron tune, Q_{x0} / Q_{y0}	26.13 / 26.18
Synchrotron tune, Q_s	0.0051
Momentum compaction factor, α_p	1.9×10^{-3}
Number of bunches	1
Rms bunch length, $4\sigma_t$	1.7 ns
Horizontal / Vertical normalised emittance, ϵ_x / ϵ_y	$2 \mu\text{m} / 2 \mu\text{m}$
Average horizontal / vertical beta function, $\langle \beta_x \rangle / \langle \beta_y \rangle$	42.0941 m / 42.0137 m *
Number of macroparticles, N_{mp}	5×10^5
Number of longitudinal slices, N_{slices}	500

* Model values for the Q26 optics.

For all the PyHEADTAIL simulation studies presented in this thesis, the Twiss

¹The SUSSIX code is applied to the complex position in phase space, $u - ip_u$, while an FFT algorithm is applied only to the transverse position u , where $u = (x, y)$ [56].

parameter $\alpha_u(s)$ and the dispersion function $D_u(s)$ equal zero. This is a valid assumption for the studies as these parameters have no direct impact on the effects under investigation.

To facilitate the observation of the coherent tune, the bunch was initialised with a static offset of $0.15\sigma_{x,y}$ in both transverse planes², such as it performs dipole oscillations around the machine. Then, it was tracked for 600 turns and the coherent tune was computed using a NAFF algorithm [97, 98], which provides a refined FFT analysis, and its python implementation, NAFFlib, can be found in the corresponding package in Ref. [99], on the turn-by-turn centroid motion. The coherent tune shift was computed by subtracting the obtained tune value from the unperturbed coherent tune (in the absence of impedance) which equals the Q_{u0} value.

Finally, the dependence of the coherent tune on the intensity value was studied in the absence of other detuning effects (such as chromaticity or detuning with transverse amplitude, even though they mainly introduce incoherent tune shifts).

The simulation was repeated for a range of bunch intensities, N_b , equally-spaced from 0 to 5×10^{10} protons per bunch. This range was chosen to be in the vicinity of the bunch intensity of the CC experiments of 2018, where N_b was 3×10^{10} protons per bunch. $N_b = 0$ is not a realistic value. However, it is used here as the reference point for which the coherent betatron tune equals zero. The simulation results are plotted against the theoretically expected tune shifts in Fig. 7.3.

The theoretically expected values are computed from Eqs. (2.57) and (2.62) for $l = 0$ and using only the imaginary part of the impedance. Given that $\Gamma(1/2) = \sqrt{\pi}$ and $Q_u = \omega_{u0}/\omega_{\text{rev}}$ equation Eq. (2.57) becomes:

$$\Delta\Omega_u^{(0)} = \Omega_{u0}^{(0)} - \omega_{u0} = \frac{\sqrt{\pi}}{4\pi} \frac{N_b r_0 c^2}{\gamma_0 \frac{2\pi}{\omega_{\text{rev}}} \omega_u \sigma_z} Z_{\text{eff,im}} = \frac{N_b r_0 c^2}{8\pi^{3/2} \gamma_0 Q_u \sigma_z} Z_{\text{eff,im}} \quad (7.1)$$

All the parameters inserted in Eq. (7.1) should be converted in CGS (centimetre–gram–second) units.

²The rms transverse beam size at the only interaction point along the ring i.e. at the location where the beam interacts with the wakefields.

7. Simulation studies: Suppression mechanism from the beam transverse impedance

Then the coherent betatron tune shift is computed by inserting the result of Eq. (7.1) in Eq. (2.62) such as

$$\Delta Q_u = \frac{\Delta \Omega_u^{(0)}}{\omega_{\text{rev}}}. \quad (7.2)$$

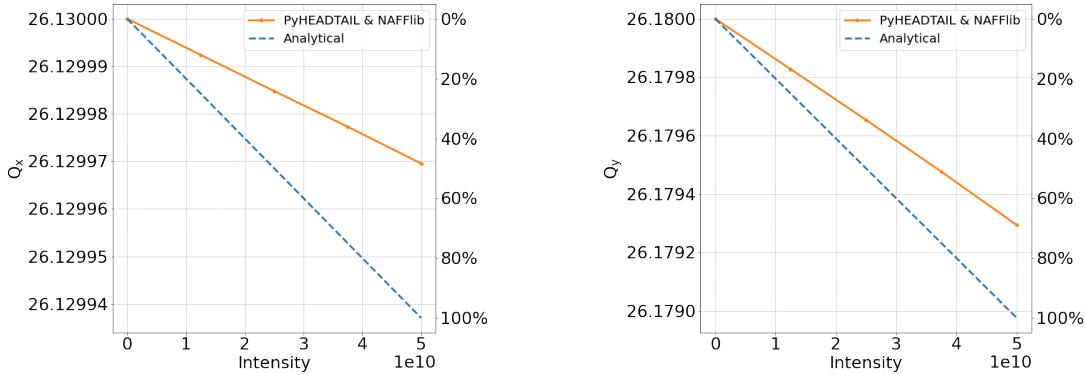


Figure 7.3: Horizontal (left) and vertical (right) coherent tunes as a function of intensity in the presence of the beam coupling SPS impedance obtained using analytical formula (blue dashed line) and PyHEADTAIL tracking simulations (orange line). The impedance model and the wake functions used are available in the public gitlab repository of Ref. [91].

Figure 7.3 shows that the coherent tune shift from the analytical model does not agree with simulation results. In particular the wakefields implementation in the PyHEADTAIL results just to $\sim 50\%$ and $\sim 70\%$ of the total coherent tune shift estimated using the analytical formula of Sacherer with the impedance model. This discrepancy hadn't been observed before as this study has not been conducted for such low intensities (the usual intensity range for this type of study is in the order of 10^{11} protons per bunch [100]) and short bunches. The analytical predictions from Sacherer formula have been repeatedly successfully benchmarked against beam measurements [101, 102] which indicates that there is an issue with the model of the wakes or with their implementation in the simulation. Given the fact that the studies with CCs are quite sensitive on the coherent tune shift with intensity from the coupling impedance (this will be discussed in the following paragraphs of this chapter) it is crucial to identify the reason for the observed discrepancy and resolve it.

After several studies and discussions with the experts on the topic ³ it was identified that the components of the resistive wall and the step transitions needed

³In particular with Carlo Zannini, carlo.zannini@cern.ch.

to be re-computed to provide higher accuracy at the lower frequencies. The details of this work are not discussed here as they are out of the scope of this thesis and they were not performed by the author. The re-computed wake functions along with the rest of the components of the original model can be found in the gihub repository of Ref. [103] and it will be referred to as the "updated wakefields" model.

The coherent betatron tune as a function of intensity obtained using PyHEADTAIL and the updated wakefields model is plotted in Fig. 7.4 against the analytical predictions from Sacherer formula. In the both transverse planes, the results from the simulations and the theory are in very good agreement ($\leq 5\%$) which is within the uncertainty that one can expect from the model implementation.

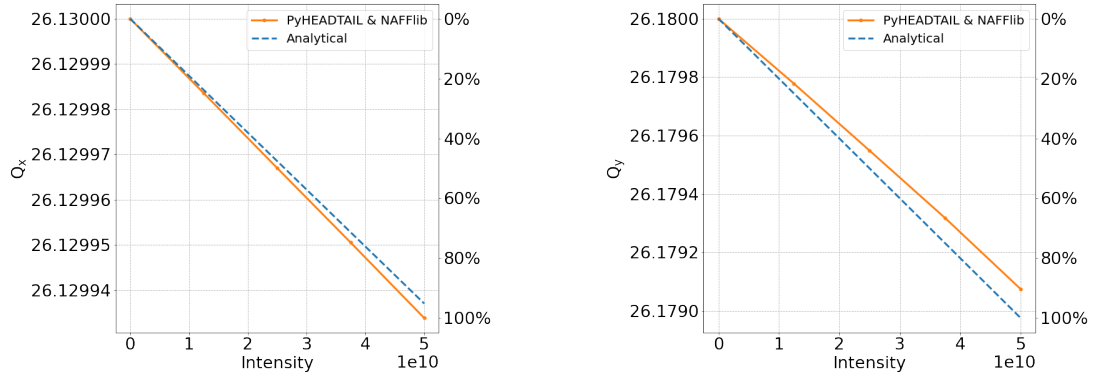


Figure 7.4: Horizontal (left) and vertical (right) coherent tunes as a function of intensity in the presence of the beam coupling SPS impedance obtained using analytical formula (blue dashed line) and PyHEADTAIL tracking simulations (orange line). The impedance model and the wake functions ("updated wakefields" model) used are available in the public repositories of Ref. [91] and Ref. [103] respectively.

The above figure demonstrates that the updated wakefields model is reliable and it confirms that its implementation in PyHEADTAIL is correct. Therefore it will be used to study the interplay of the CC noise induced emittance growth with impedance induced effects. These studies are presented in the following chapter.

7.2 Emittance growth simulations setup

The simulations that were performed to investigate the impact of the beam coupling impedance on the CC RF noise-induced emittance growth were performed following the procedure and using the parameters that are described below. Any change in the choice of parameters, e.g. for some of the parametric studies, will be mentioned in the corresponding paragraph.

The parameters used for setting up the linear transfer map, the longitudinal tracking, and the beam initialisation are shown in Table 7.1 and are the ones used in the SPS CC experiment of 2018. The ring is consisted of two segments with two interaction points. In the first one CC noise-like kicks are applied on the beam particles while in the second one the beam interacts with the wakefields as discussed in the previous section. The updated wakefields model Ref. [103] of the SPS was used.

At the location of the CC RF noise kick the horizontal and vertical beta functions equals the values at the location of the CC2 which was used in the experiments of 2018. At the location, where the wakefield kicks are applied the transverse beta functions equal the corresponding average beta functions over the SPS machine (see Section 2.5.1).

As already discussed in the previous section, the simulations are performed for the Twiss parameter $\alpha_u(s)$ and the dispersion function $D_u(s)$ equal zero. This is a valid assumption for the studies as these parameters have no direct impact on the effects under investigation.

The emittance growth studies were performed for intensity of 3×10^{10} protons per bunch in accordance with the 2018 experiments. The bunch population was represented by 5×10^5 macroparticles and the number of longitudinal slices was 500. The emittance growth was also simulated without including the wakefields. For the latter case the bunch population was represented by 10^5 particles and no longitudinal slicing was applied. The studies were performed using an initial Gaussian bunch distribution in the six-dimensional phase space. This is a good approximation for the bunches used in the experimental studies of 2018.

At the location of the CC RF noise kick, the angle, y' , of each particle within the bunch is updated every turn according to the kicks of Eqs. (3.5) and (3.6) for amplitude and phase noise kick respectively. The scaling factor, A equals 10^{-8} except if it is stated otherwise. This noise level, which corresponds to power spectral density of $1.68 \cdot 10^{-10} \text{ rad}^2/\text{Hz}$ or $1/\text{Hz}$ for phase and amplitude noise respectively is much stronger than the ones of the actual CC RF system and was chosen such as it results in a reasonable growth in the simulation time of 10^5 turns (it corresponds to ~ 2.5 seconds in the SPS). The emittance growth over the course of the simulation is comparable to that during a coast though. This approach is valid due to the linear growth of emittance with time and the linear scaling with the noise level [63]. The parameters used for the implementation of the CC RF noise kick in the simulations are shown in Table 7.2.

Table 7.2: PyHEADTAIL simulation parameters used for the implementation of the CC RF noise kicks for the emittance growth studies. This table is complementary of Table 7.2.

Parameter	Value
Horizontal / vertical beta function, $\beta_{x,\text{CC}}/\beta_{y,\text{CC}}$	30.31 m / 73.82 m
CC frequency, f_{CC}	400.78 MHz
Scaling factor for amplitude and phase noise, A	10^{-8}

Last, the emittance growth simulation studies were performed for non-zero linear chromaticity and for non-zero detuning with the transverse amplitude. Both effects were introduced as changes in the phase advance of the individual particles according to Eq. (2.64). The value of the linear chromaticity, $Q'_{x,y} = 0.5$ for most of the studies according to the experimental conditions of 2018. Higher order chromaticities were considered negligible. The values of the detuning coefficients will be given in the following sections.

In the following sections, the emittance growth rates will be expressed in nm/s due to the simulation time scale and will be referred to the growth of the normalised emittance values to be in agreement with the analysis of the measured data in Chapter 5.

7.3 First observations of emittance growth suppression by the impedance

The first emittance growth simulations were performed for the beam and machine conditions of the 2018 experiments. The parameters are listed in Tables 7.1 and 7.2 and the detailed procedure is described in Section 7.2. To give an overview, the study was conducted for a single proton bunch, energy of 270 GeV, bunch intensity of 3×10^{10} protons, rms bunch length $4\sigma_t = 1.7$ ns and linear chromaticity of 0.5 in both transverse planes.

CC phase noise was applied as it was the dominant type in the 2018 experiment, with power spectral density of $1.68 \times 10^{-10} \text{ rad}^2/\text{Hz}$ which corresponds to $A = 10^{-8}$ for the scaling factor of Eq. (3.6). For this noise power a growth rate of about 25 nm/s is expected (exciting the first betatron sidebands at ± 7.8 kHz, see further discussion in Section 3.2.2).

The geometric emittance value was computed every 100 turns (for computational efficiency) using the statistical definition which can be found in Eq. (2.34). The emittance growth rate was computed by performing a linear fit to the normalised (using Eq. (2.36)) emittance values over the simulation turns ($N_{\text{turns}} = 10^5$). Twenty simulation runs were conducted, to reduce the uncertainty of the results. The initial bunch distribution and the sequence of the uncorrelated noise kicks were regenerated randomly for every run. The mean and the standard deviation (including the uncertainty on the slope of the fit) were computed over all the trials.

As mentioned in Chapter 5 the Landau octupoles were switched off during the 2018 CC experiment. Nevertheless, a residual non-linearity was present in the machine mainly due to multipole components in the dipole magnets [79, 80]. As the machine non-linearities were not explicitly characterised during the experiment, the dependence on the octupole-like amplitude dependent tune spread was studied. Instead of using an actual octupolar (non-linear) element which would result to resonance excitation⁴, the amplitude dependent tune shift was

⁴In the real SPS machine the Landau octupoles are installed in families of focusing and defocusing

introduced as changes to the phase advance of the particles depending on their individual action as discussed in Eq. (2.64). More specifically, the dependence on the detuning coefficient in the vertical plane, α_{yy} , was studied. In particular α_{yy} ranges from -20000 to 20000 1/m . For the studies presented here and in the following sections of this chapter, the horizontal detuning coefficient and the cross-term were left at zero for simplicity, i.e. $\alpha_{xx} = \alpha_{xy} = 0$. The sensitivity on the cross-term is discussed in the Chapter 8, again for $\alpha_{xy} = 0$ as the horizontal coefficient does not affect the vertical emittance growth since there is no coupling between the two transverse planes.

The simulations were performed with and without the SPS impedance model to study its impact on the emittance growth induced by CC noise. Figure 7.5 shows the dependence of the growth rates on the amplitude detuning coefficient, α_{yy} . The secondary horizontal axis shows the resulting rms tune spread computed using Eq. (C.12). Incoherent tune shift from other sources, than the detuning with transverse amplitude are not included. In particular, the effect of chromaticity is not taken into account in the computation of the tune spread as it varies periodically with the synchrotron period (does it cancel out?) and the incoherent tune shift from the impedance is considered negligible.

It can be seen that when the wakefield kicks are not applied on the beam the emittance growth rate agrees very well with the value predicted by Eq. (3.8) and (within the reproducibility of the simulation) is independent of the tune spread value. It should be noted that the theoretical model is not valid for zero tune spread, and that the observed emittance growth rate for $\alpha_{yy} = 0$ is a result of the geometric distortion of the beam caused by the CC kick.

Figure 7.5 also shows a clear suppression of the transverse emittance growth when the wakefield kicks are included. The suppression depends on the tune spread and is asymmetric for positive and negative values of the detuning coefficient. Over a realistic range of tune spread values (estimated with MAD-X [50] including the non-linearities of SPS [79, 80] and $Q'_{x,y} = 0.5$, and shown by the grey shaded area in Fig. 7.5) the suppression reaches up to a factor 4-5. This suppression is very close

in order to avoid the excitation of resonances.

7. Simulation studies: Suppression mechanism from the beam transverse impedance

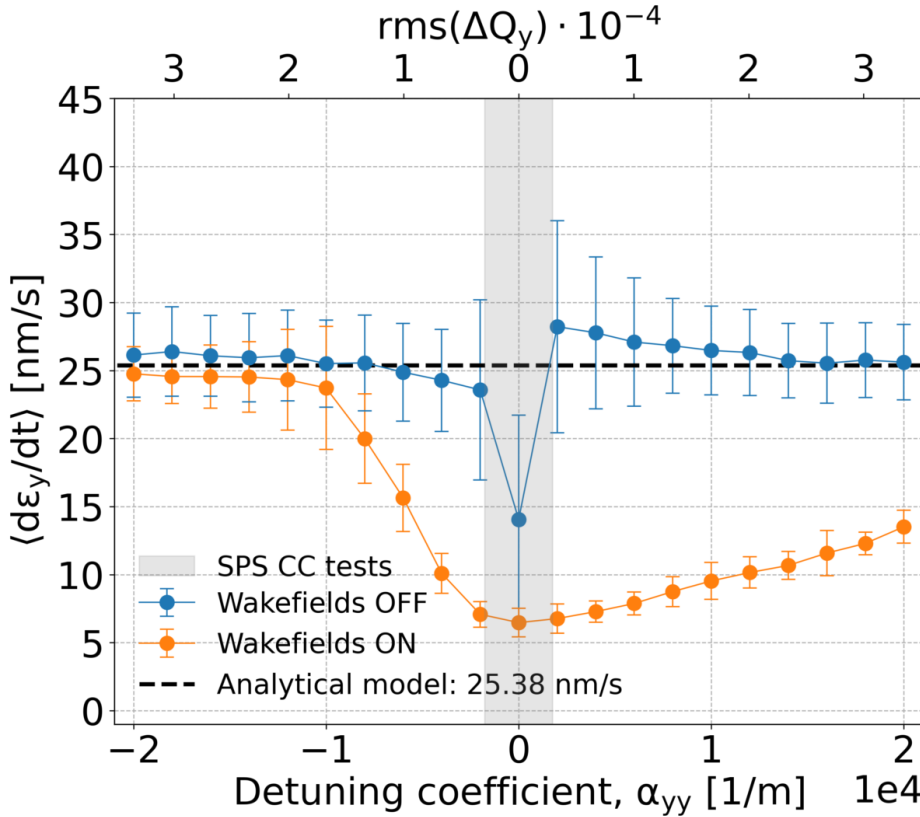


Figure 7.5: Transverse emittance growth driven by CC RF phase noise without (blue) and with (orange) the impedance effects.

to that observed in the experiments and suggests that the impedance effects might explain the discrepancy between the measured and theoretically estimated emittance growth rates.

To sum up, PyHEADTAIL simulations showed for the first time that the transverse beam impedance (which is not included in the theory of P. Baudrenghien and T. Mastoridis [63]) has a significant impact on the emittance growth driven by CC RF noise. The effect of the suppression of noise-induced emittance growth from the impedance has not been observed before. To characterise this effect and to be able to understand the mechanism behind it, a series of exploratory studies were conducted and are discussed in the following section.

7.4 Characterisation of the emittance growth suppression by the impedance

This section, discusses the results of the exploratory simulation studies which investigate the suppression of the CC RF noise-induced emittance growth by the transverse beam coupling impedance. The goal is to characterise the effect and understand the mechanism behind it. First, the impact of the impedance is studied in the presence of amplitude noise and in the presence of a noise kick (both in amplitude and phase) from a CC with the same frequency as the main RF system of the machine (HL-LHC scenario). Then, the effect of the impedance in the presence of a pure dipolar noise kick was simulated followed by a sensitivity study on the impact of the linear chromaticity. Finally, the impact of the dipolar and quadrupolar wakefields was disentangled.

The simulations were conducted following the same pattern as the case discussed in the previous section. Nevertheless, the main relevant parameters for each case will also be listed in the corresponding section.

7.4.1 Amplitude noise

The simulations discussed here were performed with and without the SPS impedance model in the presence of CC RF amplitude noise, with power spectral density of 1.68×10^{-10} 1/Hz which corresponds to $A = 10^{-8}$ for the scaling factor in Eq. (3.5). The amplitude of the amplitude noise kicks equals the one of the phase noise kicks used in the previous section. The results are shown in Fig. 7.6.

It can be seen that the emittance growth rate agrees very well with the value predicted by Eq. (3.7) and (within the reproducibility of the simulation) is independent of the tune spread value both when the wakefields are included and when they are not. In other words, the simulations demonstrate that the emittance growth driven by CC RF amplitude noise (which is associated with the headtail mode 1) is not suppressed by impedance induced effects. As the phase noise kick is similar to a dipolar noise kick (headtail mode 0) but with a high order distortion it seems that the suppression form the impedance is related to the dipole

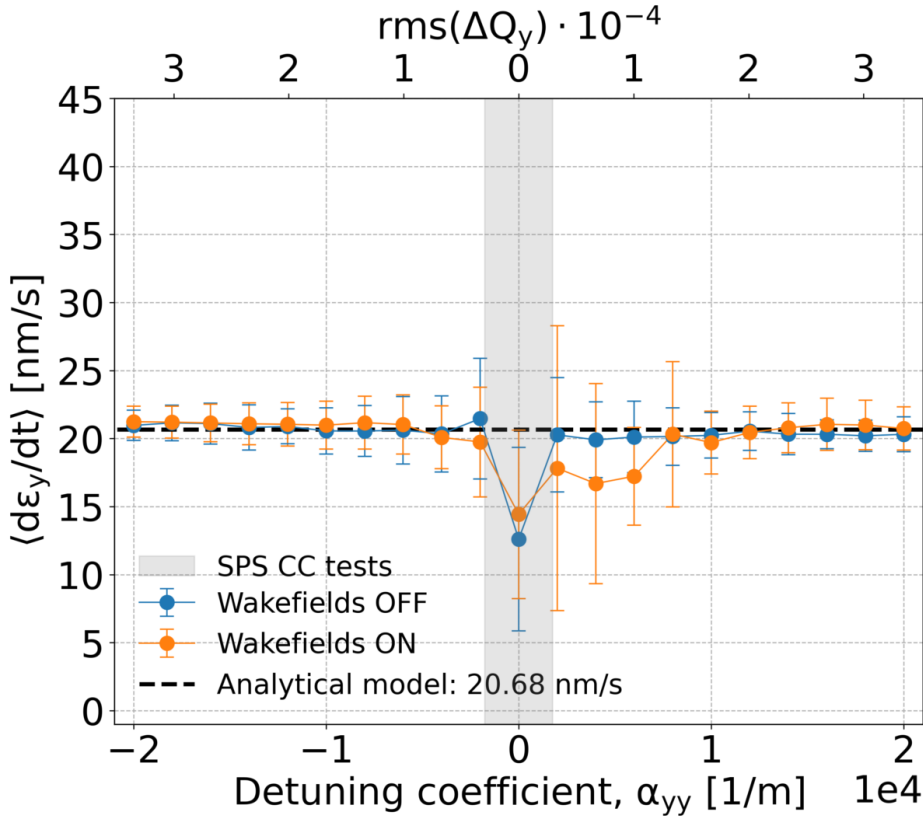


Figure 7.6: Transverse emittance growth driven by CC RF amplitude noise without (blue) and with (orange) the impedance effects.

motion.

7.4.2 CC RF noise at 200 MHz

The study was repeated for CC RF noise kick at 200 MHz, i.e. $f_{CC} = 200$ MHz, which equals the frequency of the main accelerating RF system of the SPS (see Table 5.1). The main reason for this study is that in that case in the presence of phase (amplitude) noise the headtail mode 0 (1) is more dominant than in the case of RF noise at 400 MHz. Additionally, this is also similar to the HL-LHC scenario where the main RF system and the CCs will operate at the same frequency ($f_C = f_{RF,HL-LHC}=400$ MHz).

The simulations were performed with and without the SPS impedance model in the presence of both amplitude and phase noise with power spectral density of $1.21 \times 10^{-10} \text{ rad}^2/\text{Hz}$ ($A=10^{-8}\sqrt{0.72}$) and $3.06 \times 10^{-10} \text{ rad}^2/\text{Hz}$ ($A=10^{-8}\sqrt{1.82}$) respectively. The noise strength was scaled such as it results in ~ 25 nm/s to be comparable with the initial studies presented in Section 7.3.

7.4. Characterisation of the emittance growth suppression by the impedance

The PyHEADTAIL simulation results are summarised in Fig. 7.7. The first plot (left) displays the amplitude detuning dependent emittance growth in the presence of amplitude noise while the second plot (right) in the presence of phase noise.

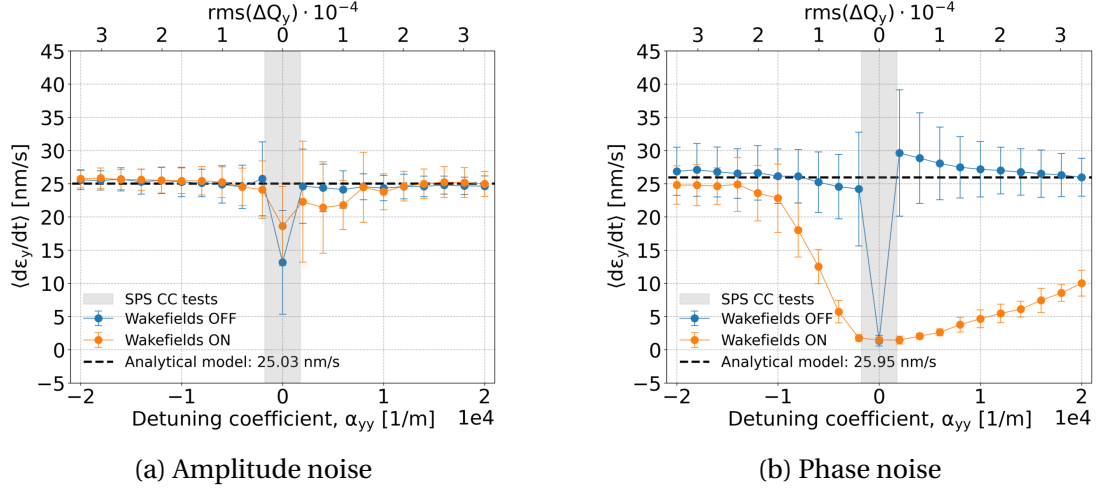


Figure 7.7: Transverse emittance growth driven by CC RF noise at $f_{CC} = 200$ MHz without (blue) and with (orange) the impedance effects.

Comparing Fig. 7.7 (left) and Fig. 7.6 it becomes evident that the behavior of the amplitude noise induced emittance growth is consistent for noise at 200 and 400 MHz (both with and without wakefields). In both cases there is no amplitude detuning dependent suppression of the emittance growth while the obtained growth rates agree very well with the theoretical predictions from Eq. (3.7).

Comparing Fig. 7.7 (right) and Fig. 7.5 it can be seen that emittance growth driven by CC phase noise in the absence of wakefield kicks (blue) is in excellent agreement for noise at 200 and 400 MHz except for the case with zero amplitude detuning, $\alpha_{yy} = 0$. It is already discussed, that for $f_{CC}=400$ MHz the observed emittance growth of ~ 15 nm/s is a result of the geometric distortion of the beam caused by the CC kick. This geometric distortion is minimised when the frequency of the CC kick equals the one of the main RF system hence the almost zero emittance growth observed for the phase noise at 200 MHz.

Repeating the last comparison but in the presence of wakefield kicks (orange) it can be seen that emittance growth driven by CC phase noise is in good agreement for noise at 200 and 400 MHz. The suppression of the emittance growth, which depends on the amplitude detuning, is observed in both cases. However, in the

7. Simulation studies: Suppression mechanism from the beam transverse impedance

case of phase noise at 200 MHz the suppression factor reaches up to a factor of 10 instead of just 4-5 in the case of noise at 400 MHz. The enhanced effect of suppression in the case where the CC has the same frequency with the main RF system of the machine and thus the headtail mode 0 is dominant provides an additional argument that the emittance growth suppression from the beam coupling impedance is associated to that mode. To this end, as a next step the emittance growth induced by a pure dipolar noise is studied.

7.4.3 Pure dipolar noise

Based on this result, the next step is to validate that the suppression is indeed associated with the headtail mode 0.

This can be achieved by applying a pure dipolar noise kick on the beam, as shown in Eq..

7.4.4 Sensitivity to linear chromaticity

The PyHEADTAIL results of the scan in the linar chromaticity values, Q'_y are displayed in Fig

7.4.5 Disentangle quadrupolar and dipolar contribution

7.5 Suppression mechanism

7.5.1 Past studies with beam-beam interactions

7.5.2 Intensity scans

7.5.3 Schottky noise spectra

7.6 Towards HL-LHC case

7.6.1 Damper

Comment on the 200 MHz

I might make a comment: Detailed studies with PyHEADTAIL showed that the emittance growth suppression can reach up to a factor of 2-4 for crab cavity phase noise when the bunch length is longer than the cavity wavelength, which was the case for the SPS experiments. However, for short bunch lengths, which will be the case in the HL-LHC, the suppression factor was found to be similar to the case of pure dipolar noise reaching a factor of 10. The scope of this project is also to characterize the impact of the crab cavities in the long-term emittance evolution in HL-LHC. Thus, the interplay of the transverse impedance and the transverse feedback system, which is planned to suppress the crab cavity noise induced emittance growth in HL-LHC, started being investigated. The first simulation results indicate that the emittance suppression from the feedback system is not affected by the impedance, due to the much faster damping time of the former.

7.7 Conclusions

You need to modiy it a bit. In a second step, simulations including the complete transverse impedance model of SPS, which was not taken into account so far, were performed with PyHEADTAIL. It was found that the transverse impedance can suppress the crab cavity noise induced emittance growth once the coherent tune, which is shifted by the impedance, moves out of the incoherent tune spectrum. It turns out that the decoherence process is slowed down and thus the noise induced emittance growth is suppressed. This mechanism, which has been observed in the past as a result of beam-beam interactions, is related to the transverse dipole oscillation of the beam. To this end the suppression is not observed for amplitude but only for phase noise induced emittance growth.

8 | Experimental studies 2022

9 | Simple model of describing the decoherence suppression from impedance

- The use of damper is an appropriate configuration as it provides dipolar noise kicks in the beam and as shown in Chapter 7 the suppression mechanism is related to the dipole motion.
- More machine time. no cryo module and team needed. only two people..
- Less uncertainties from CC setup.

10 | Conclusion

A | Definitions and methods of statistical analysis

A.1 Basic terminology

This appendix, introduces the basic terminology of statistical analysis and gives the definitions that are used in this thesis. The definitions follow the book by R. J. Barlow [104] where one can find a more detailed insight.

A.1.1 Averages

Arithmetic mean

For a data set of N data $\{x_1, x_2, x_3, \dots, x_N\}$ the arithmetic mean or just mean of the value of x is:

$$\langle x \rangle = \frac{1}{N} \sum_{i=1}^N x_i. \quad (\text{A.1})$$

Below, two properties of the arithmetic mean are discussed as they are used in this thesis.

- The mean of the sum of two variables x and y is equal to the sum of their means, ie:

$$\langle x + y \rangle = \langle x \rangle + \langle y \rangle \quad (\text{A.2})$$

- If x and y are independent the mean of their product equals:

$$\langle x \cdot y \rangle = \langle x \rangle \cdot \langle y \rangle \quad (\text{A.3})$$

A. Definitions and methods of statistical analysis

Another notation for the arithmetic mean that is often found in bibliography is, \bar{x} .

Root mean square

In the classical definition in mathematics, the root mean square (rms) is an alternative to the arithmetic mean and is defined as:

$$x^{rms} = \sqrt{\frac{x_1^2 + x_2^2 + x_3^2 + \dots + x_N^2}{N}} = \langle x^2 \rangle. \quad (\text{A.4})$$

- **Disclaimer:** It is common in physics and in sciences in general for the term rms to correspond to what is actually defined as standard deviation (see definition in Appendix A.1.2). This convention, is also followed in this thesis.

A.1.2 Measuring the spread

Variance

For a data set of N data $\{x_1, x_2, x_3, \dots, x_N\}$ the variance of x expresses how much it can vary from the mean value, $\langle x \rangle$. The variance, $\text{Var}(x)$, is defined as:

$$\text{Var}(x) = \frac{1}{N} \sum_{i=1}^N (x_i - \langle x \rangle)^2. \quad (\text{A.5})$$

Alternatively, the variance can be expressed in a simpler way as follows (see Ref. [104] p.24-25):

$$\text{Var}(x) = \langle x^2 \rangle - \langle x \rangle^2. \quad (\text{A.6})$$

Standard deviation

The square root of the variance is the standard deviation (std):

$$\sigma_x = \sqrt{\text{Var}(x)} = \sqrt{\frac{1}{N} \sum_{i=1}^N (x_i - \langle x \rangle)^2}, \quad (\text{A.7})$$

or as follows from Eq. (A.6):

$$\sigma_x = \sqrt{\langle x^2 \rangle - \langle x \rangle^2}. \quad (\text{A.8})$$

The spread in a data set is usually expressed with the standard deviation instead of the variance, as the standard deviation has the same units with the variable x .

Full width half maximum

An alternative measure of the spread is the full width half maximum (FWHM).

A.1.3 Data sets with more than one variables - Covariance

In the case that each element of the data set consists of a pair of variables, $\{(x_1, y_1), (x_2, y_2), (x_3, y_3), \dots, (x_N, y_N)\}$ the covariance expresses the extent to which x and y tend to vary together. The covariance between x and y is defined as:

$$\text{Cov}(x, y) = \frac{1}{N} \sum_{i=1}^N (x_i - \langle x \rangle)(y_i - \langle y \rangle). \quad (\text{A.9})$$

It can be seen that the covariance of variable x with itself equals the variance. In particular, it is written:

$$\text{Cov}(x, x) = \sqrt{\frac{1}{N} \sum_{i=1}^N (x_i - \langle x \rangle)^2} = \text{Var}(x) = \sigma_x^2. \quad (\text{A.10})$$

Covariance matrix

The covariance as defined above is only calculated between two variables. To express the covariance values of each pair of variables, the covariance matrix or Sigma matrix is introduced as follows and is:

$$\Sigma = \begin{pmatrix} \text{Cov}(x, x) & \text{Cov}(x, y) \\ \text{Cov}(y, x) & \text{Cov}(y, y) \end{pmatrix} = \begin{pmatrix} \sigma_x^2 & \text{Cov}(x, y) \\ \text{Cov}(y, x) & \sigma_y^2 \end{pmatrix} \quad (\text{A.11})$$

as the covariance between the same variables equals to the variance (Eq. (A.10)).

If the data set is a distribution the covariance matrix is a parameter of the distribution.

A.2 Least squares fitting

In sciences, many quantities can not be measured directly but can be inferred from measured data by fitting a model function to them. Common model functions are

A. Definitions and methods of statistical analysis

the Gaussian, polynomial, or sinusoidal. The fitting procedure followed in this thesis is called "least squares" and is described below based on Ref. [105].

Suppose that we have N data points (x_i, y_i) and that $y = f(x, \alpha, \beta)$ is the model function that describes the relationship between the points. The objective of the fit is to determine the optimal parameters α, β such as the model function describes best the data points. This is done by minimising the χ^2 statistics with respect to α and β :

$$\chi^2 = \sum_{i=1}^N [y_i - f(x_i, \alpha, \beta)]^2, \quad (\text{A.12})$$

where y_i is the observed value and $f(x_i, \alpha, \beta)$ the expected value from the model. In other words, χ^2 is a measure of deviation between the measurement and the expected result, and thus its minimisation results in the best fit i.e. to the optimal parameters α, β .

Weighted least squares fitting

Suppose that we have N data points $(x_i, y_i \pm \Delta y_i)$, where Δy_i is the uncertainty of y_i and that $y = f(x, \alpha, \beta)$ is the model function that describes the relationship between the points. To define the optimal parameters α, β taking into account the impact of the uncertainty Δy_i , Eq. (A.12) is written as:

$$\chi^2 = \sum_{i=1}^N \frac{[y_i - f(x_i, \alpha, \beta)]^2}{\Delta y_i^2} \quad (\text{A.13})$$

Error of the fit

The standard deviation of the fit results, $\sigma_\alpha, \sigma_\beta$, is estimated by the square root of the diagonal of their covariant matrix:

$$\begin{pmatrix} \sigma_\alpha^2 & \text{Cov}(\alpha, \beta) \\ \text{Cov}(\beta, \alpha) & \sigma_\beta^2 \end{pmatrix} \quad (\text{A.14})$$

In this thesis, the uncertainties of the fit results, $\Delta\alpha, \Delta\beta$, are defined as the standard deviation, σ_α and σ_β , of the corresponding optimal parameters.

The values of the optimal parameters and their covariance matrix are computed in this thesis using the `scipy.curve_fit` [106] function of the Python programming

language.

A.3 Propagation of uncertainty

Suppose that y is related to N independent variables $\{x_1, x_2, \dots, x_N\}$ with the following function:

$$y = f(x_1, x_2, \dots, x_N). \quad (\text{A.15})$$

If $\{\Delta x_1, \Delta x_2, \dots, \Delta x_N\}$ the uncertainties of $\{x_1, x_2, \dots, x_N\}$ respectively, the uncertainty of y , is given by [104]:

$$\Delta y = \sqrt{\left(\frac{\partial f}{\partial x_1} \Delta x_1\right)^2 + \left(\frac{\partial f}{\partial x_2} \Delta x_2\right)^2 + \dots + \left(\frac{\partial f}{\partial x_N} \Delta x_N\right)^2} \quad (\text{A.16})$$

B | Fundamentals of signal analysis and measurement

This appendix discusses the basic terminology of signal processing and gives the definitions which are used in this thesis. The focus is on Fourier transform and the power spectral density. First the most general mathematical definitions which concern signals continuous in time and with infinite time duration are discussed. Secondly, the definitions are given for signals sampled at a finite number of points, which are considered for the measurements and for the computational analysis. Furthermore, the quantities that are used most often for noise power spectrum measurements and their relationship to the mathematical definitions of the power spectral density are discussed. Finally, the way of applying a measured noise spectrum in numerical simulations is described.

B.1 Continuous-time analysis

Fourier transform

A physical process (or signal or time series) can be described in the time domain by a continuous function of time, e.g. $y(t)$, or else in the frequency domain, where the process is specified by giving its amplitude \hat{y} as a function of frequency, e.g. $\hat{y}(f)$ with $f \in (-\infty, +\infty)$. In other words, $y(t)$ and $\hat{y}(f)$ are essentially different representations of the same function. In general, $\hat{y}(f)$ can be a complex quantity, with the complex argument giving the phase of the component at the frequency f .

One can switch between these two representations using the Fourier transform

method. In this thesis the Fourier transform of a time series $y(t)$, which will be denoted in this document by \hat{y} , is defined as [107]:

$$\hat{y}(f) = \int_{-\infty}^{\infty} y(t) e^{-2\pi i t f} dt, \quad (\text{B.1})$$

where f stands for any real number. If the time is measured in seconds the frequency, f , is measured in hertz.

The inverse Fourier transform, which is used to re-create the signal from its spectrum, is defined as:

$$y(t) = \int_{-\infty}^{\infty} \hat{y}(f) e^{2\pi i t f} df. \quad (\text{B.2})$$

Power spectral density and total power

The power spectral density, $S_{yy}(f)$, of a signal (or a time series), $y(t)$, will be used extensively in this thesis: it describes the distribution of the power in a signal between its frequency components, and is defined as the Fourier transform of the autocorrelation function, $R_{yy}(t)$ [108]:

$$S_{yy}(f) = \hat{R}_{yy}(f) = \int_{-\infty}^{\infty} R_{yy}(\tau) e^{-2\pi i \tau f} d\tau. \quad (\text{B.3})$$

The continuous autocorrelation $R_{yy}(\tau)$ is defined as the continuous cross-correlation integral of $y(t)$ with itself, at lag τ [95]:

$$R_{yy}(\tau) = (y * y)(\tau) = \int_{-\infty}^{\infty} \bar{y}(t) y(t + \tau) dt, \quad (\text{B.4})$$

where $*$ denotes the convolution operation and $\bar{y}(t)$ represents the complex conjugate of $y(t)$.

According to the cross-correlation theorem [95]:

$$\hat{R}_{yy}(f) = \bar{\hat{y}}(f) \hat{y}(f) = |\hat{y}(f)|^2, \quad (\text{B.5})$$

where $\hat{y}(f)$ is the Fourier transform of the signal as defined in Eq. (B.1).

From Eq. (B.3) and Eq. (B.5) the power spectral density of a signal $y(t)$ can be simply

written as the square of its Fourier transform:

$$S_{yy}(f) = |\hat{y}(f)|^2, \quad (\text{B.6})$$

with $f \in (-\infty, +\infty)$.

B.2 Discrete-time analysis

Discrete-time signals

Figure B.1 shows a part of a continuous signal $y(t)$. As already mentioned, for the measurements and the computational analysis, signals (or time series) sampled at a finite number of points are considered. Such signals are called discrete-time signals and in most cases they are sampled at equal points in time. For example, in Figure B.1, it is assumed that the continuous signal, $y(t)$, is sampled at intervals Δt creating a set of N points. The length in time between the first and final sample is $T_{\text{sample}} = \frac{N-1}{N} T$, where $T = N\Delta t$.

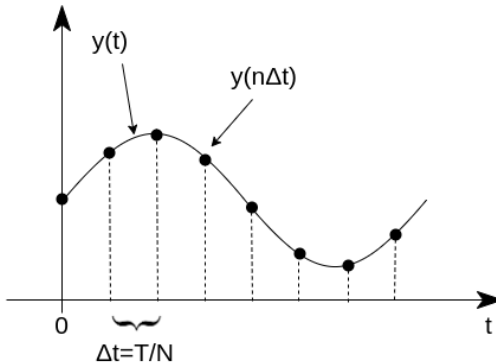


Figure B.1: Sampling of the continuous signal $y(t)$ at a finite number of points N . The sampled signal is the discrete-time signal $y(n\Delta t)$ with Δt the sampling interval and n an integer such that $n \in [0, N - 1]$.

Discrete Fourier transform

Let us consider a discrete-time signal, y_n which is sampled at N consecutive samples, $y_n = y(n\Delta t)$, with $n \in [0, N - 1]$ such that Δt is the sampling interval. For later convenience, we assume that N is an odd integer. As a first step, we note that the integral of Eq. (B.1) can be represented by a discrete sum in the limit that

$\Delta t \rightarrow 0$:

$$\hat{y}(f) = \int_{-\infty}^{\infty} y(t) e^{-2\pi i f t} dt = \lim_{\Delta t \rightarrow 0} \sum_{n=-\infty}^{\infty} y(n\Delta t) e^{-2\pi i f n\Delta t} \Delta t. \quad (\text{B.7})$$

Based on the expression for the summation in Eq. (B.7), we define the discrete Fourier transform as follows:

$$\hat{y}_k = \sum_{n=0}^{N-1} y(n\Delta t) e^{-2\pi i \frac{kn}{N}}. \quad (\text{B.8})$$

Here, the index k is an integer in the range $-\frac{N-1}{2}$ to $\frac{N-1}{2}$. Each component \hat{y}_k of the discrete Fourier transform is related to the component $\hat{y}(f)$ of the continuous Fourier transform of $y(t)$, for $f = k/T$, in the limit $\Delta t \rightarrow 0$ and $N \rightarrow \infty$ (and where it is assumed that $y(t) = 0$ for $t < 0$ and for $t > T$).

It should be noted that the discrete Fourier transform is calculated only at integer values of k , and therefore for N samples the discrete Fourier transform will consist of N numbers. The components of the discrete Fourier transform are calculated at frequencies f_k that are integer multiples of $\Delta f = 1/T = f_s/N$, with $f_s = 1/\Delta t$ the sampling frequency. In that case, $f_k \in [-\frac{N-1}{2T}, \frac{N-1}{2T}]$. An example of a discrete Fourier transform is shown in Fig. B.2.

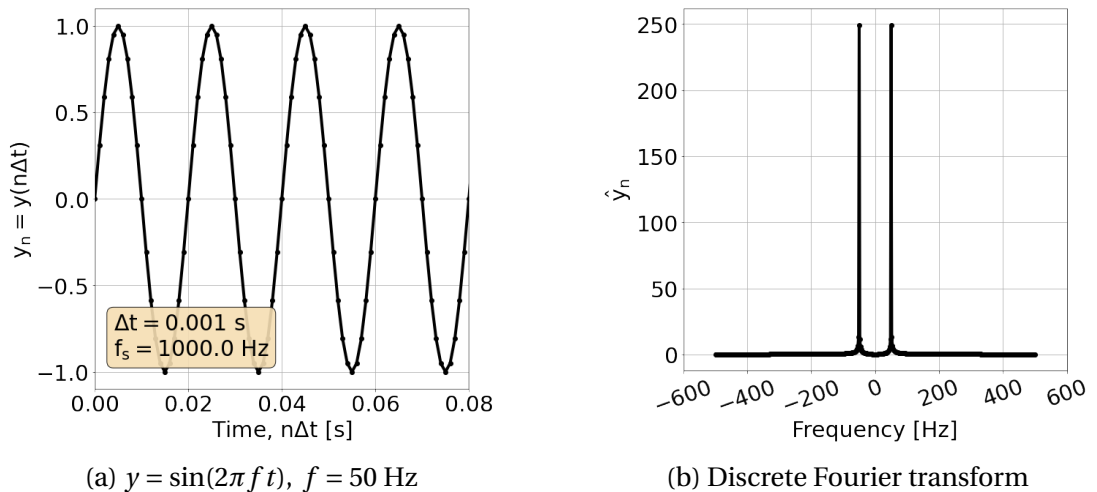


Figure B.2: Example of a signal sampled at discrete time intervals, and the corresponding discrete Fourier transform.

B. Fundamentals of signal analysis and measurement

The inverse discrete Fourier transform is defined as:

$$y_n = y(n\Delta t) = \frac{1}{N} \sum_{k=-\frac{N-1}{2}}^{\frac{N-1}{2}} \hat{y}_k e^{2\pi i \frac{kn}{N}}, \quad (\text{B.9})$$

where $n \in [0, N - 1]$ and where n and k are both integers.

The definitions given in Eq. (B.8) and Eq. (B.9) are consistent with those used in numpy, in the numpy.fft function [109] package of the Python programming language.

Power spectral density

Following Eq. (B.6) the power spectral density of a discrete-time signal should be estimated as follows:

$$S_{yy}(f_k) = A |\hat{y}_k(f_k)|^2, \quad (\text{B.10})$$

where $f_k \in [-\frac{N-1}{2T}, \frac{N-1}{2T}]$. A is a normalisation constant which is introduced in order to obtain the correct amplitudes at each frequency and thus the correct noise power. There are several different conventions for the choice of this normalization. In this thesis, the following normalization is considered (see more details in the dedicated paragraph at the end of this section):

$$S_{yy}(f_k) = \frac{1}{N^2 \Delta f} |\hat{y}_k(f_k)|^2, \quad (\text{B.11})$$

where $\Delta f = 1/T$ the frequency resolution and N the number of samples.

Figure B.3 shows an example power spectrum of the time-domain signal shown in Fig. B.2a. It can be seen that the spectrum that results from the analysis above is two-sided, which means that it has both positive and negative frequencies. It is also symmetric around the DC component ($f = 0$ Hz), which is actually a property of a real signal.

The power spectral density is expressed in terms of the square of the amplitude of the signal per unit frequency. For example, for a signal defined in units of voltage, V, (e.g. from an oscillator) the units are V^2/Hz .

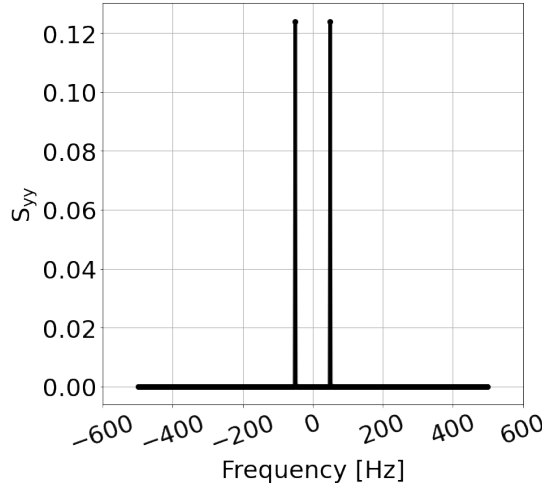


Figure B.3: Power spectrum of $y = \sin(2\pi f t)$, $f = 50$ Hz.

Conversion of a two-sided power spectrum to a single-sided power spectrum

As already mentioned, the frequency spectrum of a real signal is symmetric around the DC component and therefore the information contained in the negative frequency is redundant. For this reason, most of the instruments used in experiments to display a frequency analysis show just the positive part of the spectrum (single-sided spectrum).

In order to convert from a two-sided spectrum to a single-sided spectrum, the negative part of the spectrum is discarded, and the amplitudes of the positive frequency components (excluding the DC component, so for $f > 0$) are multiplied by a factor 2:

$$G_{yy}(f_k) = \begin{cases} 0, & f_k < 0 \\ S_{yy}(f_k), & f_k = 0 \\ 2S_{yy}(f_k), & f_k > 0 \end{cases} \quad (\text{B.12})$$

where $S_{yy}(f_k)$ is the two-sided spectrum and $G_{yy}(f_k)$ the single-sided spectrum. Figure B.4 illustrates the single-sided spectrum of the signal shown in Fig. B.2a.

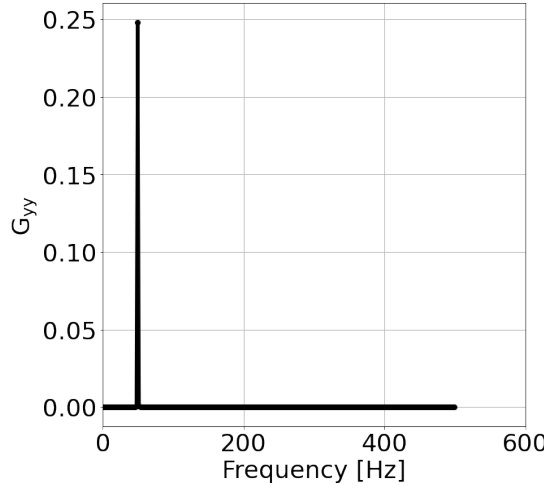


Figure B.4: Single-sided power spectrum of the signal shown in Fig. B.2(a).

Normalisation factor for the power spectral density of a discrete-time signal

This paragraph, discusses the choice of the normalisation factor $A = 1/(N^2 \Delta f)$ for the power spectral density of a discrete-time signal defined in Eq. (B.10):

$$S_{yy}(f_k) = A |\hat{y}_k(f_k)|^2. \quad (\text{B.13})$$

Consider the example of a discrete-time series $y_n = y(n\Delta t)$ where n is an integer such that $n \in [0, N-1]$. y_n represents a sequence of successive points equally spaced in time, drawn from a normal distribution with known standard deviation σ and zero mean, $\mu = 0$. The variance of this collection of N equally spaced values is given by:

$$\sigma^2 = \frac{1}{N} \sum_{n=0}^{N-1} |y_n|^2. \quad (\text{B.14})$$

According to Parseval's theorem [95], the variance can be written as:

$$\sigma^2 = \frac{1}{N^2} \sum_{k=-\frac{N-1}{2}}^{\frac{N-1}{2}} |\hat{y}_k|^2, \quad (\text{B.15})$$

where \hat{y}_k is the discrete Fourier transform of y_n .

Using Eq. (B.3), the autocorrelation function $R_{yy}(\tau)$ for a continuous-time signal can

be found from the inverse Fourier transform of $S_{yy}(f)$:

$$R_{yy}(\tau) = \int_{-\infty}^{\infty} \bar{y}(t) y(t + \tau) dt = \int_{-\infty}^{\infty} S_{yy}(f) e^{2\pi i t f} df. \quad (\text{B.16})$$

For zero lag, this becomes:

$$R_{yy}(0) = \int_{-\infty}^{\infty} S_{yy}(f) df = \sigma^2. \quad (\text{B.17})$$

This expresses the fact that the autocorrelation of a zero-mean stochastic process (such as y_n) is equal to the variance. It should be noted here that this integration over the spectral components yields the total power of the process.

For a discrete-time signal, we require that the power spectral density $S_{yy}(f_k)$ corresponds to the power spectral density for the continuous-time signal. In that case, Eq. (B.17) becomes:

$$\sigma^2 = \sum_{k=-\frac{N-1}{2}}^{\frac{N-1}{2}} S_{yy}(f_k) \Delta f. \quad (\text{B.18})$$

From Eq. (B.15) and Eq. (B.18) this leads to:

$$\frac{1}{N^2} \sum_{k=-\frac{N-1}{2}}^{\frac{N-1}{2}} |\hat{y}_k|^2 = \sum_{k=-\frac{N-1}{2}}^{\frac{N-1}{2}} S_{yy}(f_k) \Delta f, \quad (\text{B.19})$$

and hence:

$$\sum_{k=-\frac{N-1}{2}}^{\frac{N-1}{2}} \frac{|\hat{y}_k|^2}{N^2 \Delta f} = \sum_{k=-\frac{N-1}{2}}^{\frac{N-1}{2}} S_{yy}(f_k). \quad (\text{B.20})$$

Therefore, to satisfy the requirement that the power spectral density for the discrete-time signal corresponds to that for the continuous-time signal, we define the power spectral density for a discrete-time signal:

$$S_{yy}(f_k) = \frac{|\hat{y}_k|^2}{N^2 \Delta f}. \quad (\text{B.21})$$

Hence, the normalisation factor in Eq. (B.10) is chosen to be:

$$A = \frac{1}{N^2 \Delta f}. \quad (\text{B.22})$$

B.3 Measuring amplitude and phase noise

Amplitude and phase modulation are two of the main types of noise in the output signal of an oscillator. The instantaneous output voltage of an ideal oscillator can be expressed as:

$$V(t) = V_0 \sin(2\pi f_0 t), \quad (\text{B.23})$$

where V_0 is the nominal peak voltage amplitude and f_0 the nominal frequency.

However, in practice, small inaccuracies will introduce amplitude and phase modulations. These modulations are included in the above signal by adding stochastic processes, represented by $\phi(t)$ and $\epsilon(t)$, as follows:

$$\begin{aligned} V(t) &= (V_0 + \epsilon(t)) \sin(2\pi f_0 t + \phi(t)), \\ &= \left(1 + \frac{\epsilon(t)}{V_0}\right) V_0 \sin(2\pi f_0 t + \phi(t)), \\ &= (1 + \alpha(t)) V_0 \sin(2\pi f_0 t + \phi(t)), \end{aligned} \quad (\text{B.24})$$

where $\phi(t)$ is the deviation from the nominal phase $2\pi f_0 t$, $\epsilon(t)$ is the deviation from the nominal amplitude and $\alpha(t) = \epsilon(t)/V_0$ is the normalised amplitude deviation. An example of a signal with phase and amplitude noise is shown in Fig. B.5.

Following the IEEE [110] conventions, the amplitude and phase modulation are measured by one-sided spectral densities, $G_{yy}(f)$. From Eq. (B.11) and Eq. (B.12), the amount of amplitude noise can be expressed as:

$$G_\alpha(f_k) = 2S_\alpha(f_k) = \frac{2}{N^2 \Delta f} \left(\frac{|\hat{\epsilon}(f_k)|}{V_0} \right)^2 = \frac{2}{N^2 \Delta f} |\hat{\alpha}(f_k)|^2, \quad (\text{B.25})$$

and the amount of phase noise can be expressed:

$$G_\phi(f_k) = 2S_\phi(f_k) = \frac{2}{N^2 \Delta f} |\hat{\phi}(f_k)|^2, \quad (\text{B.26})$$

where f_k lies in a range of positive frequencies and $\hat{\alpha}(f_k)$ and $\hat{\phi}(f_k)$ are the discrete Fourier transforms of the modulation signals $\alpha(t)$ and $\phi(t)$ respectively. The units of the $G_\alpha(f_k)$ are $1/\text{Hz}$ and the units of $G_\phi(f_k)$ are rad^2/Hz .

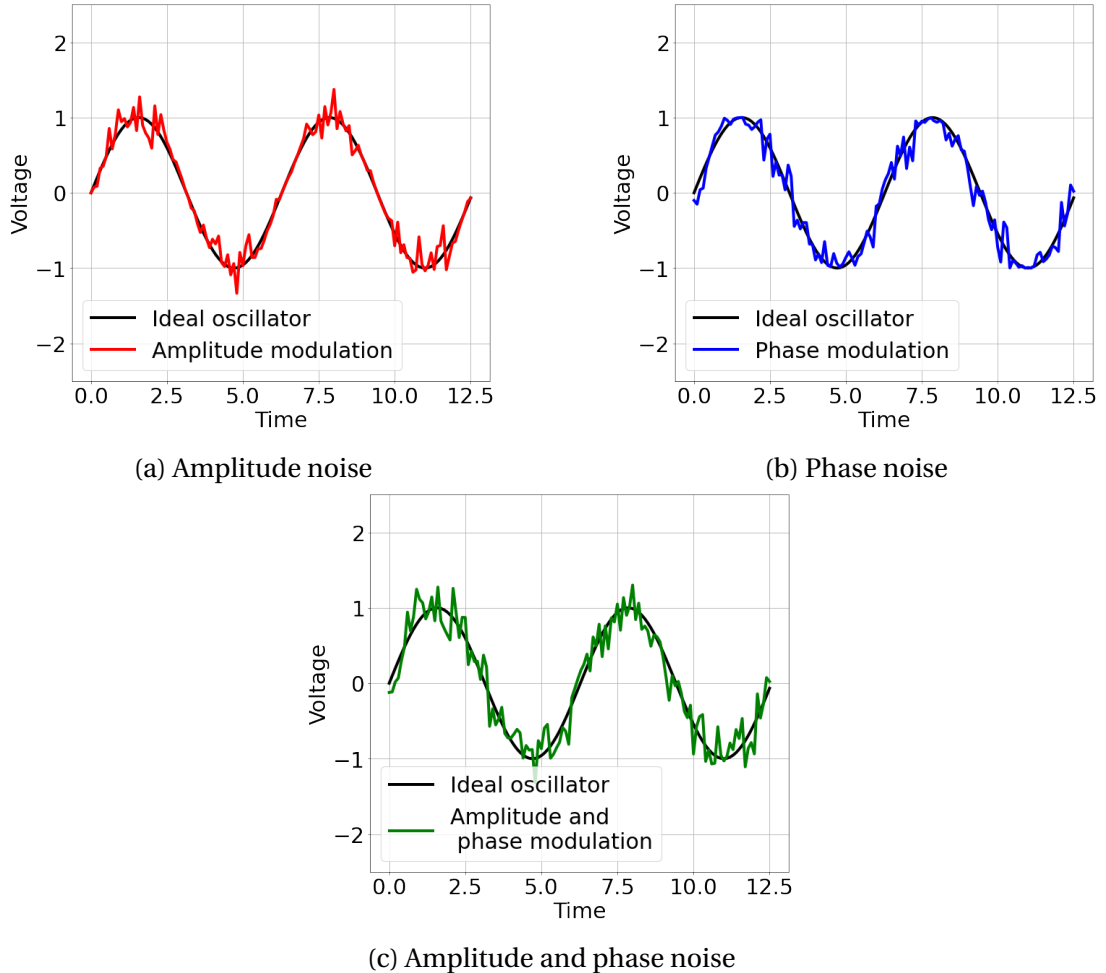


Figure B.5: Instantaneous voltage of an oscillator in the presence of (a) amplitude noise, (b) phase noise, and (c) both amplitude and phase noise.

However, instruments used in experiments do not usually display directly the single-sided spectral density G_{yy} . Instead, the quantity $10\log_{10} \mathcal{L}(f_k)$ [dBc/Hz] is shown, with [110]:

$$\mathcal{L}(f_k) = G_{yy}(f_k)/2, \quad (\text{B.27})$$

where f_k ranges from 0 over the positive part of the spectrum. It should be emphasised that here \mathcal{L} is two-sided, as defined in [110], though it is considered that the instrument displays only the positive frequencies.

B.4 Applying a measured noise spectrum in numerical simulations

The goal of this section is to describe how one can convert the measured noise spectrum from a spectrum analyzer to a discrete time series that can be used for numerical simulations.

B.4.1 Crab cavity noise in numerical simulations

As follows from the discussion in section ??, phase and amplitude noise can be represented by discrete time series $\phi_n = \phi(n\Delta t)$ and $\alpha_n = \alpha(n\Delta t)$ respectively, so that the crab cavity (CC) instantaneous voltage is given by:

$$V_{CC}(n\Delta t) = V_0(1 + \alpha(n\Delta t)) \sin(2\pi f_0 n\Delta t + \phi(n\Delta t)), \quad (\text{B.28})$$

where V_0 and f_0 are the nominal crab cavity voltage and frequency respectively, $n \in [1, N - 1]$ and N is the number of samples.

In numerical simulations, N is taken to be equal to the number of turns in the simulation. The total time simulated is $T = N\Delta t$, where Δt is the sampling interval. Since the phase and amplitude noise are sequences of noise kicks which are applied to the CC voltage every turn, Δt is equal to the time needed for one turn around the machine. For the SPS, with a revolution frequency $f_{\text{rev}} = 43.38$ kHz, $\Delta t = 1/f_s = 1/f_{\text{rev}} \approx 23$ μ s.

B.4.2 Measured noise spectrum

In the experiment performed in 2018, the amplitude and phase noise levels were measured with a spectrum analyser E5052B [81] and are expressed in terms of the quantity $10\log_{10} \mathcal{L}(f_k)$ [dBc/Hz] (see section ??). Figure B.6a shows an example of a phase noise spectrum acquired during the experiment, and which extends from 1 kHz to 10 MHz. The spectral lines observed at high frequencies correspond to harmonics of the revolution frequency.

B.4.3 Generating time series

In the following, the steps required to generate the discrete time series α_n and ϕ_n from the measured noise spectrum are discussed. The procedure involves converting the measured noise power to the two-sided power spectral density $S_\phi(f_k)$ and then using the inverse Fourier transform to produce the discrete-time series of noise kicks. In detail, the steps are as follows:

1. Convert the measured noise power $10\log_{10}\mathcal{L}(f_k)$ [dBc/Hz] to $G_\phi(f_k)$ [rad²/Hz] using Eq. (B.27) (Fig. B.6b).
2. Re-sample the noise spectrum. The measured noise power values are equally spaced in frequency on a logarithmic scale. A linear interpolation is needed such that they are equally spaced on a linear scale, every $\Delta f = f_s/N$. As already mentioned, since the beam encounters the crab cavities once each turn, $f_s = f_{rev}$ ($= 43.38$ kHz for the SPS). To this end, the linear interpolation extends up to $f_s/2$ as illustrated in Fig. B.6c. In our simulations, $N = 10^5$ turns are used.
3. Create the positive spectral components of the two-sided power spectrum, S_ϕ , using Eq. (B.12) for $f_k > 0$. The result is shown in Fig. B.6d.
4. Compute the amplitude of the spectral components of the Fourier transform, $|\hat{\phi}_n(f_k)|$ according to Eq. (B.11). It should be noted, however, that this computation is done only for the positive part of the spectrum. Fig. B.6e depicts the result of this computation.
5. Generate the phase information for each positive spectral component. By definition the power spectral density does not contain any information about the phase of the frequency components. Therefore, one should generate this information by giving a random phase $\theta(f_k)$ obtained from uniform distribution between 0 and 2π .
6. Construct a one-sided frequency domain signal, $\hat{\phi}_n^{\text{os}}(f_k) = |\hat{\phi}_n(f_k)| e^{i\theta(f_k)}$. Once again this computation is done only for the positive spectral components, with $f_k \in [\Delta f, +\frac{f_s}{2}]$.

B. Fundamentals of signal analysis and measurement

7. Construct the two-sided Fourier transform spectrum. First, create the negative components of the Fourier transform by taking the complex conjugate of the positive components. Furthermore, the information for the zero frequency component (DC) is missing from the measured spectrum, since this extends from 1 kHz to 10 MHz. In order to do the conversion correctly, the zero frequency term is set to 0, so that $\hat{y}_n(0) = 0$. The two-sided Fourier transform is then given by:

$$\hat{\phi}_n(f_k) == \begin{cases} |\hat{\phi}_n^{\text{os}}(f_k)| e^{i\theta(|f_k|)}, & f_k \in \left[-\frac{f_s}{2}, -\Delta f_s\right] \\ |\hat{\phi}_n^{\text{os}}(f_k)| = 0, & f_k = 0 \\ |\hat{\phi}_n^{\text{os}}(f_k)| e^{i\theta(|f_k|)}, & f_k \in \left[+\Delta f_s, +\frac{f_s}{2}\right] \end{cases} \quad (\text{B.29})$$

It is clear that $\hat{\phi}_n(f_k)$ has both positive and negative frequencies and the magnitude is symmetric in f_k .

8. Finally, apply the inverse Fourier transform, Eq. (B.9), to $\hat{\phi}_n(f_k)$. The output is a random discrete time series of N values sampled every $\Delta t = 1/f_s = 1/f_{rev}$. In other words, ϕ_n forms the sequence of noise kicks that will act on the particles in the beam on each turn in the simulations.

B.4.4 Validation of the time series reconstruction

This section describes the benchmarks that were carried out to ensure that the method described in section B.4.3 produces a valid time series for a set of noise kicks, for a given power spectrum.

Comparison of measured and reconstructed power spectrum

Figure B.7 shows the results of the first benchmark, comparing the measured power spectral density with the power spectral density computed from the generated time series ϕ_n . The two power spectra appear to be consistent with each other, which supports the validity of the method described above for generating the sequence of noise kicks from a given power spectrum.

B.4. Applying a measured noise spectrum in numerical simulations

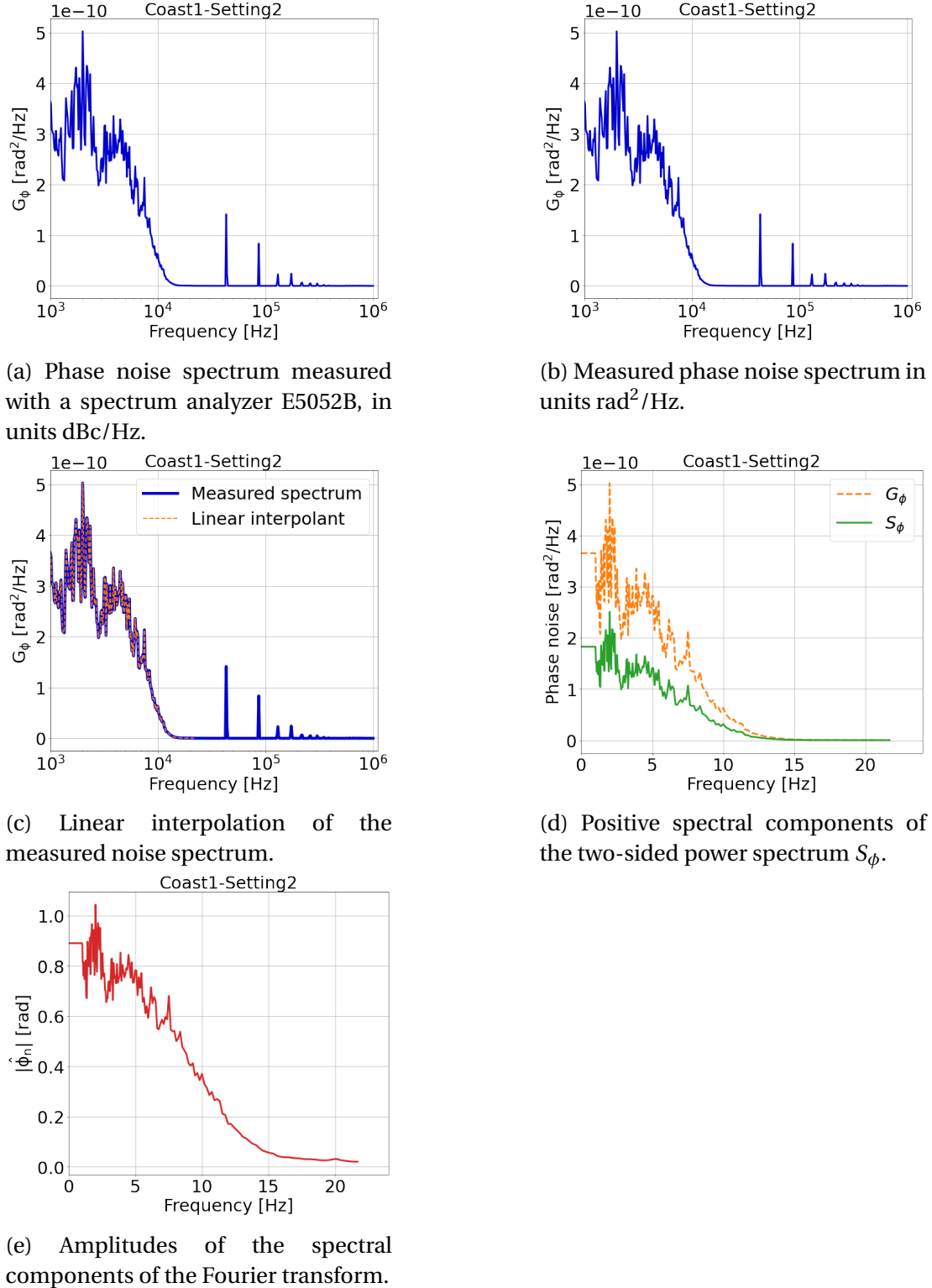


Figure B.6: Steps required to generate the sequence of noise kicks to be applied in the simulations from the measured noise spectrum.

PyHEADTAIL simulations

Another way to validate the method for producing a sequence of noise kicks from a measured power spectrum is to perform numerical simulations using the generated

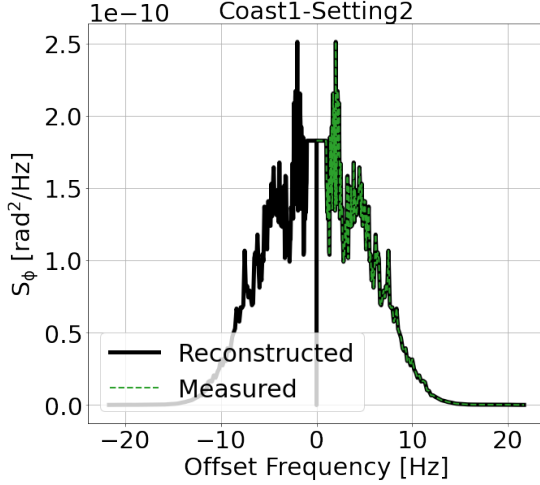


Figure B.7: Power spectral density computed from the time series ϕ_n produced from a measured power spectrum (black), compared with the original measured power spectrum (green).

noise kicks, and compare the resulting emittance growth with the predictions from an analytical model [63].

In the simulations, which were performed with PyHEADTAIL, the beam was tracked for 10^5 turns which corresponds to about 2.5 s in the SPS. A kick representing the effect of the crab cavities was applied on each turn. The noise kicks that the beam encounters every turn at the CC location were generated from the phase and amplitude noise spectra of from Coast1-Setting2 of 2018 (Fig. 5.2).

It should be noted, however, that the sequence of noise kicks includes a random factor through the set of random phases $\theta(f_k)$. To reduce the uncertainty in the results, multiple simulation runs were conducted. The set of random phases was regenerated randomly for each of 10 runs with a different seed each time. For each run, the initial bunch distribution was also regenerated randomly 3 times. The mean and the standard deviation of the emittance values obtained from the tracking were computed over all trials. The emittance growth rate was computed by performing a linear fit to the mean of the emittance values.

Figures B.8a and B.8b show the emittance growth for the case of amplitude noise and phase noise respectively. The emittance evolution in the presence of both types of noise is also illustrated in Fig. B.8c. The simulated emittance growth rates show

B.4. Applying a measured noise spectrum in numerical simulations

very good agreement with the predictions from the analytical model. The results again support the validity of the method for generating a sequence of noise kicks from a measured noise power spectrum, described in section B.4.3.

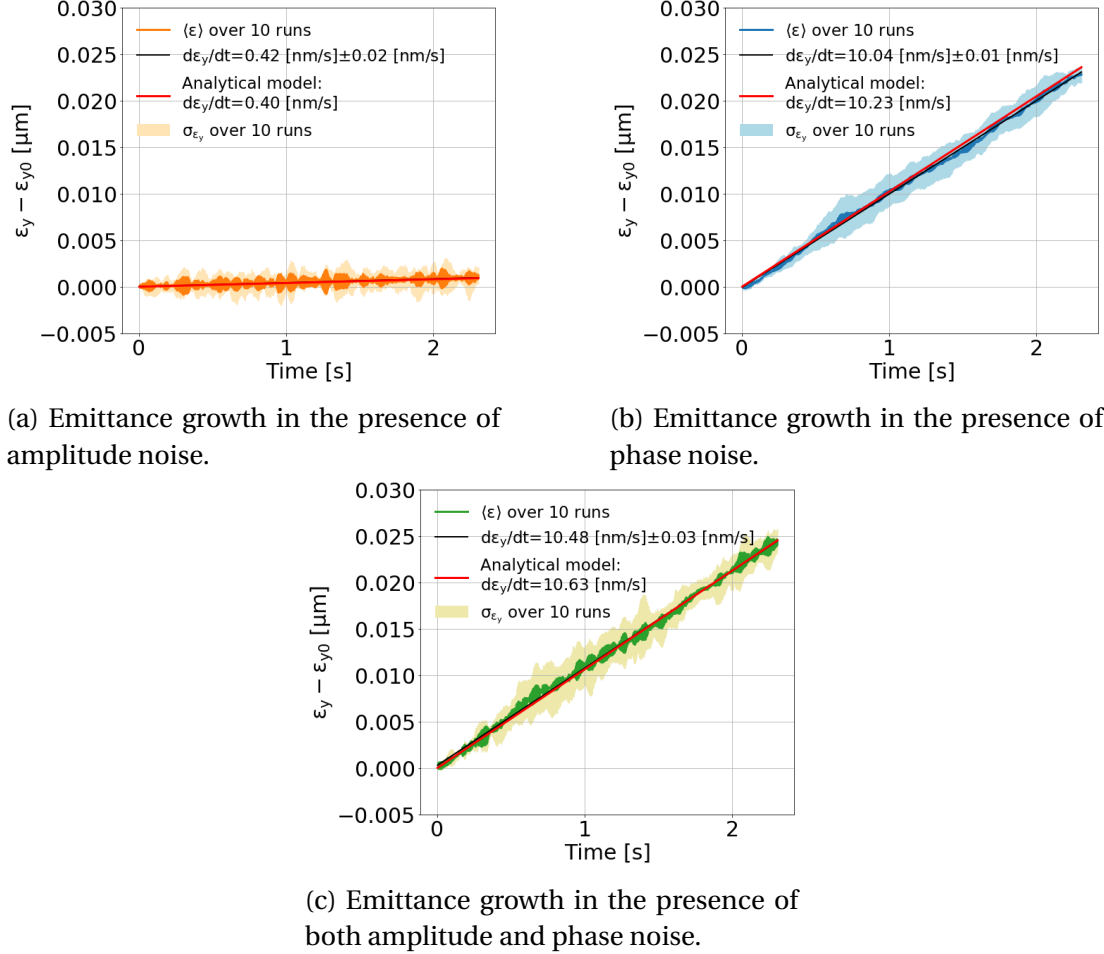


Figure B.8: Comparison between emittance growth found from simulations in PyHEADTAIL and emittance growth expected from an analytical model [63]. The emittance growth is driven by amplitude and phase noise, with kicks in the simulations generated from a measured power spectrum.

C | Appendix C

C.1 Solutions of betatron equations

The calculations here are performed according to the discussion in Ref. [86] and Ref. [111].

By inserting Eq. (2.13) in Eq. (2.11) it results to:

$$u' = Aw'(s) \cos(\psi_u(s) + \psi_{u,0}) + Aw(s)[- \sin(\psi_u(s) + \psi_{u,0})]\psi'(s) \quad (\text{C.1})$$

which becomes:

$$\begin{aligned} u''(s) = & Aw'' \cos(\psi_u(s) + \psi_{u,0}) + Aw'(s)[- \sin(\psi_u(s) + \psi_{u,0})]\psi'_u(s) + \\ & + Aw'(s)[- \sin(\psi_u(s) + \psi_{u,0})]\psi'_u(s) + \\ & + Aw(s)[- \cos(\psi_u(s) + \psi_{u,0})]\psi'^2_u(s) + \\ & + Aw(s)[- \sin(\psi_u(s) + \psi_{u,0})]\psi''_u(s) + \\ & + A\{\cos(\psi_u(s) + \psi_{u,0})[w'' - w(s)\psi''_u(s)] + \\ & - \sin(\psi_u(s) + \psi_{u,0})[2w'(s)\psi'(s) + w(s)\psi''_u(s)]\} \end{aligned} \quad (\text{C.2})$$

Now, inserting $u(s)$ and $u''(s)$ in Eq. (2.13) gives:

$$\begin{aligned} u''(s) + K_u(s)u(s) = & [w''(s)w(s)\psi'^2_u(s) + K(s)w(s)]\cos(\psi_u(s) + \psi_{u,0}) + \\ & - [2w'(s)\psi'_u + w(s)\psi''_u(s)]\sin(\psi_u(s) + \psi_{u,0}) = 0. \end{aligned} \quad (\text{C.3})$$

In the above equation, for the functions $w(s)$ and $\psi_u(s)$ to not depend in a particular motion they must not vary with $\psi_{u,0}$ [86]. To fulfill this requirement the coefficients of sine and cosine must vanish individually.

Multiplying with $w(s)$ the coefficient of sine gives:

$$2w(s)w'(s)\psi'_u(s) + w^2(s)\psi''_u(s) = [w^2(s)\psi'_u(s)]' = 0, \quad (\text{C.4})$$

which by integration is written as:

$$\psi_u(s) = \oint_C \frac{ds}{w^2(s)} \quad (\text{C.5})$$

Replacing $\psi'_u(s)$ in the coefficient of cosine gives:

$$w^3(s)(w''(s) + K_u(s)w(s)) = 1. \quad (\text{C.6})$$

C.2 Detuning with amplitude

- The linear detuning is given by the following formula, for octupole components

The detuning with amplitude is computed by:

$$\Delta Q_x = 2(\alpha_{xx}J_x + \alpha_{xy}J_y) \quad (\text{C.7})$$

$$\Delta Q_y = 2(\alpha_{yy}J_y + \alpha_{yx}J_x) \quad (\text{C.8})$$

where α_{yy} , α_{xx} and $\alpha_{xy} = \alpha_{yx}$ are the detuning coefficients with units [1/m] and J_x , J_y the action variables.

Rms detuning with amplitude

From the definition of variance, the variance of the vertical amplitude detuning is

C. Appendix C

given by:

$$\begin{aligned}
\text{Var}(\Delta Q_y) &= \langle \Delta Q_y^2 \rangle - \langle \Delta Q_y \rangle^2 \\
&= \langle 2^2 (\alpha_{yy} J_y + \alpha_{yx} J_x)^2 \rangle - \langle 2(\alpha_{yy} J_y + \alpha_{yx} J_x) \rangle^2 \\
&= 2^2 [\langle (\alpha_{yy} J_y + \alpha_{yx} J_x)^2 \rangle - \langle \alpha_{yy} J_y + \alpha_{yx} J_x \rangle^2] \\
&= 2^2 [\langle (\alpha_{yy} J_y)^2 + 2\alpha_{yy}\alpha_{yx}J_yJ_x + (\alpha_{yx} J_x)^2 \rangle - (\langle \alpha_{yy} J_y \rangle + \langle \alpha_{yx} J_x \rangle)^2] \\
&= 2^2 [\alpha_{yy}^2 \langle J_y^2 \rangle + 2\alpha_{yy}\alpha_{yx} \langle J_y J_x \rangle + \alpha_{yx}^2 \langle J_x^2 \rangle - \alpha_{yy}^2 \langle J_y \rangle^2 - 2\alpha_{yy}\alpha_{yx} \langle J_y \rangle \langle J_x \rangle - \alpha_{yx}^2 \langle J_x \rangle^2] \\
&= 2^2 [\alpha_{yy}^2 \langle J_y^2 \rangle + \cancel{2\alpha_{yy}\alpha_{yx} \langle J_y J_x \rangle} + \alpha_{yx}^2 \langle J_x^2 \rangle - \alpha_{yy}^2 \langle J_y \rangle^2 - \cancel{2\alpha_{yy}\alpha_{yx} \langle J_y J_x \rangle} - \alpha_{yx}^2 \langle J_x \rangle^2] \\
&= 2^2 [\alpha_{yy}^2 (\langle J_y^2 \rangle - \langle J_y \rangle^2) + \alpha_{yx}^2 (\langle J_x^2 \rangle - \langle J_x \rangle^2)] \\
&= 2^2 [\alpha_{yy}^2 \text{Var}(J_y) + \alpha_{yx}^2 \text{Var}(J_x)]
\end{aligned} \tag{C.9}$$

In the development of Eq. C.9 the properties of the mean discussed in Eq. (A.2) and (A.3) are used.

Now, according to the definitions introduced in Appendix A.1, the root mean square (rms) for the vertical amplitude detuning is written:

$$\begin{aligned}
\Delta Q_y^{rms} &= \sigma_{\Delta Q_y} = \sqrt{\text{Var}(\Delta Q_y)} \\
&= \sqrt{2^2 [\alpha_{yy}^2 \text{Var}(J_y) + \alpha_{yx}^2 \text{Var}(J_x)]} \\
&= 2\sqrt{\alpha_{yy}^2 (\sigma_{J_y})^2 + \alpha_{yx}^2 (\sigma_{J_x})^2} \\
&= 2\sqrt{[\alpha_{yy} (\sigma_{J_y})]^2 + [\alpha_{yx} (\sigma_{J_x})]^2}
\end{aligned} \tag{C.10}$$

where σ_{J_y} and σ_{J_x} stand for the standard deviation of the action variables J_y and J_x respectively

For a Gaussian distribution the actions, J_x and J_x follow an exponential distribution¹. It is known that for an exponential distribution the mean equals the standard deviation. Therefore, Eq. C.10 can be written as follows:

$$\Delta Q_y^{rms} = 2\sqrt{[\alpha_{yy} \langle J_y \rangle]^2 + [\alpha_{yx} \langle J_x \rangle]^2}. \tag{C.11}$$

¹The charge density function for a Gaussian beam in u, u' , where $u = (x, y)$ is expressed in terms of the Twiss parameters as: $\rho(u, u') = e^{-(\gamma_u u^2(s) + 2\alpha_u(s)u(s)u'(s) + \beta_u(s)u'^2(s))/(2c_u^{\text{geom}})} = e^{-J_u/c_u^{\text{geom}}}.$

Following Eq. (??), the rms tune spread from amplitude detuning can be also written as:

$$\Delta Q_y^{rms} = 2\sqrt{(\alpha_{yy}\epsilon_y^{geom})^2 + (\alpha_{yx}\epsilon_x^{geom})^2}. \quad (\text{C.12})$$

Equivalently, the horizontal rms tune spread from amplitude detuning is given by:

$$\Delta Q_x^{rms} = 2\sqrt{(\alpha_{xx}\epsilon_x^{geom})^2 + (\alpha_{yx}\epsilon_y^{geom})^2}. \quad (\text{C.13})$$

Disclaimer: In the analysis presented above, the actions J_x and J_y refer to the initial distribution, for which they are actually independent. The actions later in time, are coupled due to the non-linear of the lattice.

Rms betatron tune spread in the SPS at 270 GeV

In this thesis, the rms betatron tune spread includes only the contribution from the detuning with amplitude present in the SPS machine. This is a result of the SPS multiple components in the main dipole magnets (see Section ??). However, experimental studies [112] indicated stronger amplitude detuning than predicted from these multiple components. The measured amplitude detuning can be reproduced in simulations by switching on the Landau octupole families with strengths $k_{LOF} = k_{LOD} = 1 \text{ m}^{-4}$.

Using the values of the multipoles listed in Table C.1 and setting the strength of both octupole families at 1 m^{-4} the corresponding detuning coefficients are obtained with MAD-X. In particular, $\alpha_{xx} = 923.45 \text{ m}^{-1}$, $\alpha_{xy} = \alpha_{yx} = -1122.451 \text{ m}^{-1}$, $\alpha_{yy} = 705.15 \text{ m}^{-1}$. It should be noted that these values are obtained for zero linear chromaticity in both transverse planes.

The tune spread is computed for the requested initial emittances for the emittance growth measurements of 2018 and 2021, $\epsilon_x^n = \epsilon_y^n = 2 \mu\text{m}$. Using Eq. (??) it can be seen that these values corresponds to geometric emittances of $\epsilon_x^{geom} = \epsilon_y^{geom} = 6.95 \text{ nm}$. By inserting these values of detuning coefficients and geometric emittances in Eq. (C.13) and Eq. (C.12) the rms tune spread is found to be, $\Delta Q_x^{rms} = 2.02 \times 10^{-5}$ and $\Delta Q_y^{rms} = 2.17 \times 10^{-5}$, in the horizontal and vertical planes respectively.

C.3 SPS non-linear model

Move this section to chapter 6. The nominal SPS model includes only the nonlinear fields produced by the chromatic sextupoles. However, one of the most important sources of non-linearities in SPS are the odd multipole components of its main dipole magnets. For some of the studies presented in this thesis their impact on the beam dynamics must be studied and therefore they should be included in the nominal model.

The multipole error of the SPS main dipoles are unfortunately not available from magnetic measurements. On this ground a non-linear optics model of the SPS has been established with beam-based measurements of the chromatic detuning over a range of momentum deviation [79, 80]. The optics model was obtained by assigning systematic multipole components to the main lattice magnets, in the nominal model of SPS, in order to reproduce the tune variation with the momentum deviation as it was measured in the real machine. The calculations were performed with MAD-X.

The values of the multipole components up to seventh order obtained from this method are given in Table C.1 where, (b_3^A, b_3^B) , (b_5^A, b_5^B) and (b_7^A, b_7^B) stand for the sextupolar, decapolar and decatetrapolar mutipoles respectively. Note that different values have been obtained for each of the two different kinds of SPS main dipoles (MBA and MBB) which are marked with the indices A and B respectively.

Table C.1: Multipole errors from SPS non-linear model, at 270 GeV.

Multipole	Value
b_3^A, b_3^B	$8.1 \times 10^{-4} \text{ m}^{-2}, 1.1 \times 10^{-3} \text{ m}^{-2}$
b_5^A, b_5^B	$9.2 \text{ m}^{-4}, -10 \text{ m}^{-4}$
b_7^A, b_7^B	$1.3 \times 10^5 \text{ m}^{-6}, 1.4 \times 10^5 \text{ m}^{-6}$

random multiple errros? Like in APR.Ch.3.2.2.

D | Glossary and definitions

Peak to peak: Peak-to-peak (pk-pk) is the difference between the maximum positive and the maximum negative amplitudes of the wave.

<https://electronics.stackexchange.com/questions/313269/peak-to-peak-vs-amplitude>

Landau octupoles

Check the HL-LHC report to take ideas.

Bibliography

- [1] Oliver Sim Brüning et al. *LHC Design Report*. CERN Yellow Reports: Monographs. Geneva: CERN, 2004. doi: 10.5170/CERN-2004-003-V-1. URL: <https://cds.cern.ch/record/782076>.
- [2] ATLAS collaboration. “Observation of a new particle in the search for the Standard Model Higgs boson with the ATLAS detector at the LHC”. In: *Physics Letters B* 716 (1) (2012), pp. 1–29. URL: <https://www.sciencedirect.com/science/article/pii/S037026931200857X>.
- [3] CMS collaboration. “Observation of a new boson at a mass of 125 GeV with the CMS experiment at the LHC”. In: *Physics Letters B* 716 (1) (2012), pp. 30–61. URL: <https://www.sciencedirect.com/science/article/pii/S0370269312008581>.
- [4] CERN Yellow Reports: Monographs. *CERN Yellow Reports: Monographs, Vol. 10 (2020): High-Luminosity Large Hadron Collider (HL-LHC): Technical design report*. en. 2020. doi: 10 . 23731 / CYRM - 2020 - 0010. URL: <https://e-publishing.cern.ch/index.php/CYRM/issue/view/127>.
- [5] Oliver Brüning and Lucio Rossi. *The High Luminosity Large Hadron Collider*. WORLD SCIENTIFIC, Feb. 2015. doi: 10.1142/9581. URL: <https://doi.org/10.1142/9581>.
- [6] W. Herr. “*Particle Colliders and Concept of Luminosity*”. at CERN Accelerator School. 2012. URL: <https://cas.web.cern.ch/sites/default/files/lectures/constanta-2018/l1.pdf>.
- [7] O. Brüning and L. Rossi. *The High Luminosity Large Hadron Collider: the New Machine for Illuminating the Mysteries of Universe*. Vol. 24. World Scientific Publishing Company, 2015.

- [8] Rama Calaga. "Crab Cavities for the High-luminosity LHC". In: (2018), THXA03. 5 p. DOI: 10 . 18429 / JACoW - SRF2017 - THXA03. URL: <https://cds.cern.ch/record/2673544>.
- [9] Hans Peter Beck. *First Results from the Large Hadron Collider*. Accessed: 24-06-2022. URL: <https://www.sps.ch/artikel/progresses/first-results-from-the-large-hadron-collider-24>.
- [10] Silvia Verdú-Andrés. *Design and Prototyping of HL-LHC Double Quarter Wave Crab Cavities*. Talk presented at th International Particle Accelerator Conference in 2015, Richmond VA (USA). Accessed: 24-06-2022. URL: https://accelconf.web.cern.ch/IPAC2015/talks/mobd2_talk.pdf.
- [11] Silvia Verdú-Andrés et al. "Crab cavities for colliders: past, present and future". In: *Nucl. Part. Phys. Proc.* 273-275 (2016), 193–197. 5 p. DOI: 10 . 1016 / j . nuclphysbps . 2015 . 09 . 025. URL: <https://cds.cern.ch/record/2263119>.
- [12] C. et al Zanoni. "Design of Dressed Crab Cavities for the HL-LHC Upgrade". In: (2015), THPB070. 5 p. DOI: 10.18429 / JACoW- SRF2015 - THPB070. URL: <https://cds.cern.ch/record/2288282>.
- [13] Subashini De Silva et al. "Electromagnetic Design of 400 MHz RF-Dipole Crabbing Cavity for LHC High Luminosity Upgrade". In: (2015), THPB053. 5 p. DOI: 10 . 18429 / JACoW - SRF2015 - THPB053. URL: <https://cds.cern.ch/record/2288607>.
- [14] Binping Xiao et al. "Design, prototyping and testing of a compact superconducting double quarter wave crab cavity". In: *Phys. Rev. Spec. Top. Accel. Beams* 18 (Feb. 2015), 041004. 10 p. DOI: 10 . 1103 / PhysRevSTAB . 18 . 041004. arXiv: 1502 . 04088. URL: <https://cds.cern.ch/record/1992565>.
- [15] S Verdú-Andrés et al. "Design and Prototyping of HL-LHC Double Quarter Wave Crab Cavities for SPS Test". In: (May 2015), 3 p. URL: <https://cds.cern.ch/record/2113440>.
- [16] N Toge. *KEK B-factory Design Report*. Tech. rep. Tsukuba: KEK, 1995. URL: <https://cds.cern.ch/record/475260>.

D. Bibliography

- [17] T. et al. Abe. "Beam operation with crab cavities at KEKB". In: *2007 IEEE Particle Accelerator Conference (PAC), Albuquerque, New Mexico, USA*. Vol. TUPAN045. 2007, pp. 1487–1489. DOI: 10.1109/PAC.2007.4440798.
- [18] Y. Funakoshi. "Operational experience with crab cavities at KEKB". In: (Oct. 2014). Comments: 10 pages, contribution to the ICFA Mini-Workshop on Beam-Beam Effects in Hadron Colliders, CERN, Geneva, Switzerland, 18-22 Mar 2013, 27–36. 10 p. DOI: 10.5170/CERN-2014-004.27. arXiv: 1410.4036. URL: <https://cds.cern.ch/record/1955812>.
- [19] K. Oide et al. "Compensation of the Crossing Angle with Crab Cavities at KEKB". In: *Proc. PAC'07* (Albuquerque, NM, USA, Jun. 2007). JACoW Publishing, Geneva, Switzerland, pp. 27–31. URL: <https://jacow.org/p07/papers/MOZAKI01.pdf>.
- [20] R. et al. Calaga. "First demonstration of the use of crab cavities on hadron beams". In: *Phys. Rev. Accel. Beams* 24 (2021), 062001. 6 p. DOI: 10.1103 / PhysRevAccelBeams.24.062001. URL: <https://cds.cern.ch/record/2773279>.
- [21] Androula Alekou et al. "Beam dynamics simulations with Crab Cavities in the SPS machine". In: (2019), MOPGW095. 4 p. DOI: 10 . 18429 / JACoW - IPAC2019 - MOPGW095. URL: <https://cds.cern.ch/record/2696109>.
- [22] C. Zanoni et al. "The crab cavities cryomodule for SPS test". In: 874 (July 2017), p. 012092. DOI: 10 . 1088 / 1742 - 6596 / 874 / 1 / 012092. URL: <https://doi.org/10.1088/1742-6596/874/1/012092>.
- [23] Luis Eduardo Medina Medrano et al. *Effective pile-up density as a measure of the experimental data quality for High-Luminosity LHC operational scenarios*. Tech. rep. Geneva: CERN, Jan. 2018. URL: <https://cds.cern.ch/record/2301928>.
- [24] T. Mastoridis P. Baudrenghien. *Crab Cavity RF noise: Update 2*. Accessed: 27-06-2022. URL: https://indico.cern.ch/event/1044711/contributions/4389271/attachments/2264292/3861025/CC_Noise_Feedback_PB.pdf.

- [25] I. Ilias Efthymiopoulos. *Luminosity estimates including noise from crab cavities (without feedback)*. Accessed: 27-06-2022. URL: https://indico.cern.ch/event/1044711/contributions/4389268/attachments/2264203/3844208/ie_WP2CCemitBU_14.06.2021.pdf.
- [26] Andrzej Wolski. *Beam Dynamics in High Energy Particle Accelerators*. Imperial College Press, 2014.
- [27] Helmut Wiedemann. *Particle accelerator physics; 4th ed.* Berlin: Springer, 2015. DOI: 10 . 1007 / 978 - 3 - 319 - 18317 - 6. URL: <https://link.springer.com/content/pdf/10.1007/978-3-319-18317-6.pdf>.
- [28] S Y Lee. *Accelerator physics; 3rd ed.* Singapore: World Scientific, 2012. URL: <https://cds.cern.ch/record/1425444>.
- [29] R A Beth. “Complex Methods for Three-Dimensional Magnetic Fields”. In: (1971). URL: <https://cds.cern.ch/record/889480>.
- [30] Tarsi Prebibaj. *Transverse Emittance and Brightness Studies at Extraction of the CERN PS Booster*. Accessed: 12-07-2021. URL: https://indico.cern.ch/event/849052/contributions/3567761/attachments/1910604/3166225/semfe_thesis_presentation_tprebibaj_final.pdf.
- [31] Jean Buon. “Beam phase space and emittance”. In: (Dec. 1990), 23 p. DOI: 10.5170/CERN-1991-004.30. URL: <https://cds.cern.ch/record/216507>.
- [32] Bernhard Holzer. *Introduction to Accelerator Physics Beam Dynamics for Summer Students*. Accessed: 13-07-2021. URL: https://indico.cern.ch/event/91711/attachments/1096595/1564350/Summer_Stud_Holzer_2010.pdf.
- [33] David Newton and Andy Wolski. *Design of Electron Storage and Damping Rings, Part 5: Coupling and Alignment*. Accessed: 13-07-2021. URL: <https://uspas.fnal.gov/materials/13CSU/Lecture5.pdf>.
- [34] G Rumolo. “Beam Instabilities”. In: (2014). Comments: 21 pages, contribution to the CAS - CERN Accelerator School: Advanced Accelerator Physics Course, Trondheim, Norway, 18-29 Aug 2013, 21 p. DOI: 10.5170/CERN-2014-009.199. URL: <https://cds.cern.ch/record/1982422>.

D. Bibliography

- [35] Jacques Gareyte, Jean-Pierre Koutchouk, and F Ruggiero. *Landau damping dynamic aperture and octupole in LHC*. Tech. rep. revised version number 1 submitted on 2003-08-21 14:12:02. Geneva: CERN, Feb. 1997. URL: <https://cds.cern.ch/record/321824>.
- [36] W Herr. “Introduction to Landau Damping”. In: (2014). Comments: 27 pages, contribution to the CAS - CERN Accelerator School: Advanced Accelerator Physics Course, Trondheim, Norway, 18-29 Aug 2013, 27 p. DOI: 10.5170/CERN-2014-009.377. URL: <https://cds.cern.ch/record/1982428>.
- [37] Elias Metral. *Longitudinal beam dynamics*. Accessed: 19-07-2021. URL: http://emetal.web.cern.ch/JUAS/2016/LongitudinalBeamDynamics_JUAS2016_EM.pdf.
- [38] Edwin M. McMillan. “The Synchrotron-A Proposed High Energy Particle Accelerator”. In: *Phys. Rev.* 68 (1945), pp. 143–144. DOI: 10.1103/PhysRev.68.143.
- [39] Veksler V. I. “A new method of accelerating relativistic particles”. In: *Dokl. Akad. Nauk SSSR* 44 (1944). (in Russian), pp. 346–348.
- [40] Veksler V. I. “About the bew method of accelerating relativistic particles”. In: *Dokl. Akad. Nauk SSSR* 44 (1944). (in Russian), pp. 393–366.
- [41] Frank Zimmermann. “Introduction to Collective Effects in Particle Accelerators”. In: *ICFA Beam Dyn. Newslett.* 69 (2016), 8–17. 10 p. URL: <https://cds.cern.ch/record/2264408>.
- [42] Giovanni Rumolo and Kevin Li. *Instabilities Part II: Longitudinal wake fields - impact on machine elements and beam dynamics*. Accessed: 20-07-2022. URL: https://indico.cern.ch/event/509762/contributions/2450946/attachments/1515079/2373718/London2_Longitudinal_v04a.pdf.
- [43] Benoit Salvant. *Building the impedance model of a real machine*. Accessed: 20-07-2022. URL: https://accelconf.web.cern.ch/ipac2019/talks/weypls1_talk.pdf.
- [44] Alexander Wu Chao. *Physics of collective beam instabilities in high energy accelerators*. New York, NY: Wiley, 1993. URL: <http://cds.cern.ch/record/246480>.

- [45] Michael Schenk. “A novel approach to Landau damping of transverse collective instabilities in future hadron colliders”. Presented 05 Feb 2019. 2019. URL: <https://cds.cern.ch/record/2665819>.
- [46] A Vlasov. “On the kinetic theory of an assembly of particles with collective interaction”. In: *Russ. Phys. J.* 9 (1945), pp. 25–40. URL: <http://cds.cern.ch/record/426186>.
- [47] Frank James Sacherer. *Methods for computing bunched-beam instabilities*. Tech. rep. Geneva: CERN, Sept. 1972. URL: <https://cds.cern.ch/record/322545>.
- [48] F J Sacherer. “Transverse bunched beam instabilities - Theory”. In: (Apr. 1974), 5 p. URL: <https://cds.cern.ch/record/322645>.
- [49] N. Biancacci, E. Métral, and M. Migliorati. “Fast-slow mode coupling instability for coasting beams in the presence of detuning impedance”. In: *Phys. Rev. Accel. Beams* 23 (12 Dec. 2020), p. 124402. DOI: 10.1103/PhysRevAccelBeams.23.124402. URL: <https://link.aps.org/doi/10.1103/PhysRevAccelBeams.23.124402>.
- [50] Laurent Deniau (editor). *MAD-X: Methodical Accelerator Design*. Accessed: 20-07-2022. URL: <https://mad.web.cern.ch/madx/>.
- [51] *Official optics repository of the CERN accelerators*. Accessed: 20-07-2022. URL: <https://gitlab.cern.ch/acc-models>.
- [52] *Official optics repository of the CERN Super Proton Synchrotron (official name SPS)*. Accessed: 16-2-2022. URL: <https://gitlab.cern.ch/acc-models/acc-models-sps/-/tree/2021/>.
- [53] *PyHEADTAIL code repository*. Accessed: 19-6-2022. URL: <https://github.com/PyCOMPLETE/>.
- [54] Adrian Oeftiger. *An overview of PyHEADTAIL*. Accessed: 05-06-2022. URL: <https://cds.cern.ch/record/2672381/files/CERN-ACC-NOTE-2019-0013.pdf>.

D. Bibliography

- [55] Michael Schenk. *Beam dynamics simulations with the PyHEADTAIL and PyECLLOUD macroparticle codes*. Accessed: 05-06-2022. URL: https://www2.kek.jp/accl/legacy/seminar/file/PyHEADTAIL_PyECLLOUD_2.pdf.
- [56] Benoit Salvant. “Impedance model of the CERN SPS and aspects of LHC single-bunch stability”. Presented on 04 Mar 2010. 2010. DOI: 10.5075/epfl-thesis-4585. URL: <https://cds.cern.ch/record/1274254>.
- [57] Volodymyr Rodin, A. Oeftiger, and Carsten Welsch. “Simulation of intra-beam scattering in PyHEADTAIL”. In: Nov. 2021. DOI: 10.18429/JACoW-IPAC2021-WEPAB215.
- [58] *Sixtracklib code repository*. Accessed: 20-07-2022. URL: <https://github.com/SixTrack/sixtracklib>.
- [59] Martin Schwinzerl et al. *Introducing Sixtracklib*. Accessed: 20-07-2022. URL: https://indico.cern.ch/event/833895/contributions/3577803/attachments/1927226/3190636/intro_sixtracklib.pdf.
- [60] Martin Schwinzerl et al. “Optimising and Extending A Single-Particle Tracking Library For High Parallel Performance. OPTIMISING AND EXTENDING A SINGLE-PARTICLE TRACKING LIBRARY FOR HIGH PARALLEL PERFORMANCE”. In: (Sept. 2021). DOI: 10 . 18429 / JACoW - IPAC2021 - THPAB190. URL: <https://cds.cern.ch/record/2781835>.
- [61] V Lebedev et al. “Emittance growth due to noise and its suppression with the feedback system in large hadron colliders”. In: *Part. Accel.* 44 (Mar. 1993), 147–164. 28 p. URL: <https://cds.cern.ch/record/248620>.
- [62] V Lebedev. “Computer simulation of the emittance growth due to noise in large hadron colliders”. In: *Part. Accel.* 44 (Mar. 1993), 165–199. 57 p. URL: <https://cds.cern.ch/record/248622>.
- [63] P. Baudrenghien and T. Mastoridis. “Transverse emittance growth due to rf noise in the high-luminosity LHC crab cavities”. In: *Phys. Rev. ST Accel. Beams* 18 (10 Oct. 2015), p. 101001. DOI: 10.1103/PhysRevSTAB.18.101001. URL: <https://link.aps.org/doi/10.1103/PhysRevSTAB.18.101001>.

- [64] K. Ohmi et al. “Response of colliding beam-beam system to harmonic excitation due to crab-cavity rf phase modulation”. In: *Phys. Rev. ST Accel. Beams* 14 (11 Nov. 2011), p. 111003. DOI: 10.1103/PhysRevSTAB.14.111003. URL: <https://link.aps.org/doi/10.1103/PhysRevSTAB.14.111003>.
- [65] Rama Calaga, Ofelia Capatina, and Giovanna Vandoni. “The SPS Tests of the HL-LHC Crab Cavities”. In: (2018), TUPAF057. 4 p. DOI: 10.18429/JACoW-IPAC2018-TUPAF057. URL: <https://cds.cern.ch/record/2649807>.
- [66] P Baudrenghien et al. “Functional Specifications of the LHC Prototype Crab Cavity System”. In: (Feb. 2013). URL: <https://cds.cern.ch/record/1520896>.
- [67] Carver Lee. *First proton beam dynamics results with crab cavities*. Accessed: 10-11-2021. URL: https://indico.cern.ch/event/800428/attachments/1804664/2945632/CrabCavity_BE_Seminar.pdf.
- [68] Philippe Baudrenghien. *SPS Crab Cavity test RF Test Program*. Accessed: 11-11-2021. URL: <https://indico.cern.ch/event/718127/contributions/2951305/attachments/1645650/2629988/SPSCtestv3.pdf>.
- [69] R. Jones and H. Schmickler. “The measurement of Q' and Q" in the CERN-SPS by head-tail phase shift analysis”. In: *PACS2001. Proceedings of the 2001 Particle Accelerator Conference (Cat. No.01CH37268)*. Vol. 1. 2001, 531–533 vol.1. DOI: 10.1109/PAC.2001.987561.
- [70] Thomas Levens, Kacper Łasocha, and Thibaut Lefèvre. “Recent Developments for Instability Monitoring at the LHC”. In: (2017), THAL02. 4 p. DOI: 10.18429/JACoW-IBIC2016-THAL02. URL: <https://cds.cern.ch/record/2313358>.
- [71] T. E. Levens et al. “Automatic detection of transverse beam instabilities in the Large Hadron Collider”. In: *Phys. Rev. Accel. Beams* 22 (11 Nov. 2019), p. 112803. DOI: 10.1103/PhysRevAccelBeams.22.112803. URL: <https://link.aps.org/doi/10.1103/PhysRevAccelBeams.22.112803>.
- [72] Tom Levens. *Beam instrumentation with SPS Crabs*. Accessed: 11-11-2021. URL: https://indico.cern.ch/event/718127/contributions/2951309/attachments/1646050/2630808/BI_SPS_Crabs.pdf.

D. Bibliography

- [73] Alexander Wu Chao et al. *Handbook of accelerator physics and engineering*; 2nd ed. Singapore: World Scientific, 2013. DOI: 10.1142 / 8543. URL: <https://cds.cern.ch/record/1490001>.
- [74] Tom Levens. *Head-Tail Monitor for CC Diagnostics*. Accessed: 11-04-2022. URL: https://indico.cern.ch/event/826475/contributions/3457525/attachments/1872464/3081710/2019-07-02_HL_WP2_tlevens.pdf.
- [75] Natalia Triantafyllou et al. “Investigation of Damping Effects of the Crab Cavity Noise Induced Emittance Growth”. In: *12th International Particle Accelerator Conference*. Aug. 2021. DOI: 10.18429/JACoW-IPAC2021-TUPAB256.
- [76] R Calaga et al. “Proton-beam emittance growth in SPS coasts”. In: *Conf. Proc. C1205201* (May 2012), THPPP007. 3 p. URL: <https://cds.cern.ch/record/1451286>.
- [77] A Alekou et al. *Emittance growth in coast in the SPS*. Accessed: 26-11-2021. URL: https://indico.cern.ch/event/609486/contributions/2457542/attachments/1433340/2318716/EmittanceEvolutionCoastSPS_2017_April.pdf.
- [78] Fanouria Antoniou et al. “Emittance Growth in Coast in the SPS at CERN”. In: *J. Phys.: Conf. Ser.* 1067 (2018), MOPMF061. 7 p. DOI: 10.18429/JACoW-IPAC2018-MOPMF061. URL: <https://cds.cern.ch/record/2649815>.
- [79] Michele Carlà et al. “Studies of a New Optics With Intermediate Transition Energy as Alternative for High Intensity LHC Beams in the CERN SPS”. In: (2018), TUPAF022. 4 p. DOI: 10.18429/JACoW-IPAC2018-TUPAF022. URL: <https://cds.cern.ch/record/2664976>.
- [80] Androula Alekou et al. “SPS Long Term Stability Studies in the Presence of Crab Cavities and High Order Multipoles”. In: (2018), WEP2PO008. 3 p. DOI: 10.18429/JACoW-HB2018-WEP2PO008. URL: <https://cds.cern.ch/record/2640326>.
- [81] K. Gheen. *Phase Noise Measurement Methods and Techniques*. Accessed November 5, 2020. Agilent Technologies. URL: <https://studylib.net/doc/18034081/phase-noise-measurements>.

- [82] J. Bosser et al. “Transverse emittance measurement with a rapid wire scanner at the CERN SPS”. In: *Nuclear Instruments and Methods in Physics Research Section A: Accelerators, Spectrometers, Detectors and Associated Equipment* 235.3 (1985), pp. 475–480. ISSN: 0168-9002. DOI: [https://doi.org/10.1016/0168-9002\(85\)90096-8](https://doi.org/10.1016/0168-9002(85)90096-8). URL: <https://www.sciencedirect.com/science/article/pii/0168900285900968>.
- [83] OE Berrig et al. *CERN-SPS Wire Scanner Impedance and Wire Heating Studies*. Tech. rep. Geneva: CERN, Sept. 2014. URL: <https://cds.cern.ch/record/1972478>.
- [84] Rogelio Tomas et al. “Improved algorithms to determine the non-linear optics model of the SPS from non-linear chromaticity”. In: July 2007, pp. 4231–4233. ISBN: 978-1-4244-0916-7. DOI: 10.1109/PAC.2007.4439986.
- [85] Department of Physics University of Pennsylvania and Lab manual astronomy. *Managin errors and uncertainties*. Accessed: 18-03-2022. URL: <https://www.physics.upenn.edu/sites/default/files/Managing%20Errors%20and%20Uncertainty.pdf>.
- [86] Federico Roncarolo. “Accuracy of the Transverse Emittance Measurements of the CERN Large Hadron Collider”. Presented 2005. 2005. URL: <https://cds.cern.ch/record/1481835>.
- [87] Philippe Baudrenghien. *LLRF experience for SPS & HL-LHC Outlook*. Accessed: 11-11-2021. URL: <https://indico.cern.ch/event/787363/contributions/3367294/attachments/1865644/3067685/HL-LHC19v6.pdf>.
- [88] F. Follin G. Papotti. *Online bunch length measurement for SPS OP*. Accessed: 26-11-2021. URL: https://indico.cern.ch/event/774525/contributions/3218683/attachments/1756129/2847423/20181120_LIUSPSBD.pdf.
- [89] G. Papotti. “A Beam Quality Monitor for LHC Beams in the SPS”. In: (Sept. 2008), 4 p. URL: <https://cds.cern.ch/record/1124099>.
- [90] T. Argyropoulos. *Private communication, Nov 2020*.
- [91] *Repository of SPS impedance model*. Accessed: 3-6-2022. URL: https://gitlab.cern.ch/IRIS/SPS_IW_model.

D. Bibliography

- [92] Carlo Zannini. “Electromagnetic Simulation of CERN accelerator Components and Experimental Applications”. Presented 15 Apr 2013. Mar. 2013. URL: <https://cds.cern.ch/record/1561199>.
- [93] B Salvant et al. “Update of the SPS Impedance Model”. In: (June 2010), 3 p. URL: <https://cds.cern.ch/record/1271349>.
- [94] Carlo Zannini et al. “Benchmarking the CERN-SPS Transverse Impedance Model with Measured Headtail Growth Rates”. In: (2015), MOPJE049. 4 p. URL: <https://cds.cern.ch/record/2141779>.
- [95] R. Bracewell. *The Fourier Transform and its Applications*. 2nd ed. McGraw-Hill, 1986.
- [96] R Bartolini and F Schmidt. *A Computer Code for Frequency Analysis of Non-Linear Betatron Motion*. Tech. rep. Geneva: CERN, Feb. 1998. URL: <https://cds.cern.ch/record/702438>.
- [97] J. Laskar. “The chaotic motion of the solar system: A numerical estimate of the size of the chaotic zones”. In: *Icarus* 88.2 (1990), pp. 266–291. ISSN: 0019-1035. DOI: [https://doi.org/10.1016/0019-1035\(90\)90084-M](https://doi.org/10.1016/0019-1035(90)90084-M). URL: <https://www.sciencedirect.com/science/article/pii/001910359090084M>.
- [98] Sofia Kostoglou et al. “Development of Computational Tools for Noise Studies in the LHC”. In: (2017), THPAB044. 4 p. DOI: 10 . 18429 / JACoW - IPAC2017 - THPAB044. URL: <https://cds.cern.ch/record/2289645>.
- [99] *NAFFlib code repository*. Accessed: 05-08-2022. URL: <https://github.com/PyCOMPLETE/NAFFlib>.
- [100] Mario Beck. “Numerical and experimental studies to model and reduce the impedance in the CERN Super Proton Synchrotron (SPS). Numerische und experimentelle Studien zur Modellierung und Reduzierung der Strahlimpedanz im Super Proton Synchrotron (SPS) Teilchenbeschleuniger”. Presented 08 Feb 2019. Dec. 2018. URL: <http://cds.cern.ch/record/2683038>.

- [101] H Bartosik et al. “TMCI thresholds for LHC single bunches in the CERN SPS and comparison with simulations”. In: (June 2016), 4 p. URL: <https://cds.cern.ch/record/1742183>.
- [102] Carlo Zannini et al. *SPS impedance-induced observables pre and post LS2*. Accessed: 06-08-2022. URL: https://indico.cern.ch/event/919160/contributions/3863191/attachments/2040319/3417759/SPS_pre_and_postLS2_HSC.pdf.
- [103] *Updated SPS wakefields model repository*. Accessed: 12-08-2022. URL: https://github.com/natriant/exploring_SPS/tree/master/updated_wakefields_model.
- [104] R. J. Barlow. *Statistics. A Guide to the Use of Statistical Methods in the Physical Sciences*. Manchester Physics Series. Wiley, 2013. ISBN: 9781118723234. URL: <https://liverpool.idm.oclc.org/login?url=https://search.ebscohost.com/login.aspx?direct=true&db=cat00003a&AN=lvp.b3130057&site=eds-live&scope=site>.
- [105] K. K. Gan. *Chi Square Distribution (χ^2) and Least Squares fitting*. Accessed: 03-03-2022. URL: <https://www.asc.ohio-state.edu/gan.1/teaching/spring04/Chapter6.pdf>.
- [106] *SciPy API Documentation*. Accessed: 16-2-2022. URL: https://docs.scipy.org/doc/scipy/reference/generated/scipy.optimize.curve_fit.html.
- [107] William H. Press et al. *Numerical Recipes: The Art of Scientific Computing*. 3rd ed. USA: Cambridge University Press, 2007. ISBN: 0521880688. URL: http://www.e-maxx-ru.1gb.ru/bookz/files/numerical_recipes.pdf.
- [108] A. Papoulis. *Probability, Random Variables, and Stochastic Processes*. Communications and Signal Processing. McGraw-Hill, 1991. ISBN: 9780070484771. URL: <https://books.google.ch/books?id=4IwQAQAAIAAJ>.
- [109] NumPy Project and Community. *NumPy API Documentation*. Accessed November 5, 2020. URL: <https://numpy.org/doc/stable/reference/routines.fft.html>.

D. Bibliography

- [110] “IEEE Standard Definitions of Physical Quantities for Fundamental Frequency and Time Metrology—Random Instabilities”. In: *IEEE Std Std 1139-2008* (2009), pp. c1–35. DOI: 10.1109/IEEESTD.2008.4797525.
- [111] Yannis Papaphilippou. *Transverse motion*. United States Particle Accelerator School, University of California - Santa Cruz, Santa Rosa, CA. Accessed: 14-07-2022. 2008. URL: <https://yannis.web.cern.ch/teaching/transverse.pdf>.
- [112] Hannes Bartosik et al. “Improved Methods for the Measurement and Simulation of the CERN SPS Non-linear Optics”. In: (2016), THPMR036. 4 p. DOI: 10 . 18429 / JACoW - IPAC2016 - THPMR036. URL: <https://cds.cern.ch/record/2207443>.